Title
In vivo cross relaxation phenomenon in the field range of 340-1000 gauss

Author
Yee, Kingman,

Publication Date
1994

Peer reviewed|Thesis/dissertation

In Vivo Cross Relaxation Phenomenon in the Field Range of 340-1000 Gauss

by

Kingman Yee

DISSERTATION

Submitted in partial satisfaction of the requirements for the degree of

DOCTOR OF PHILOSOPHY

in

Biophysics

in the

GRADUATE DIVISION

of the

UNIVERSITY OF CALIFORNIA

San Francisco

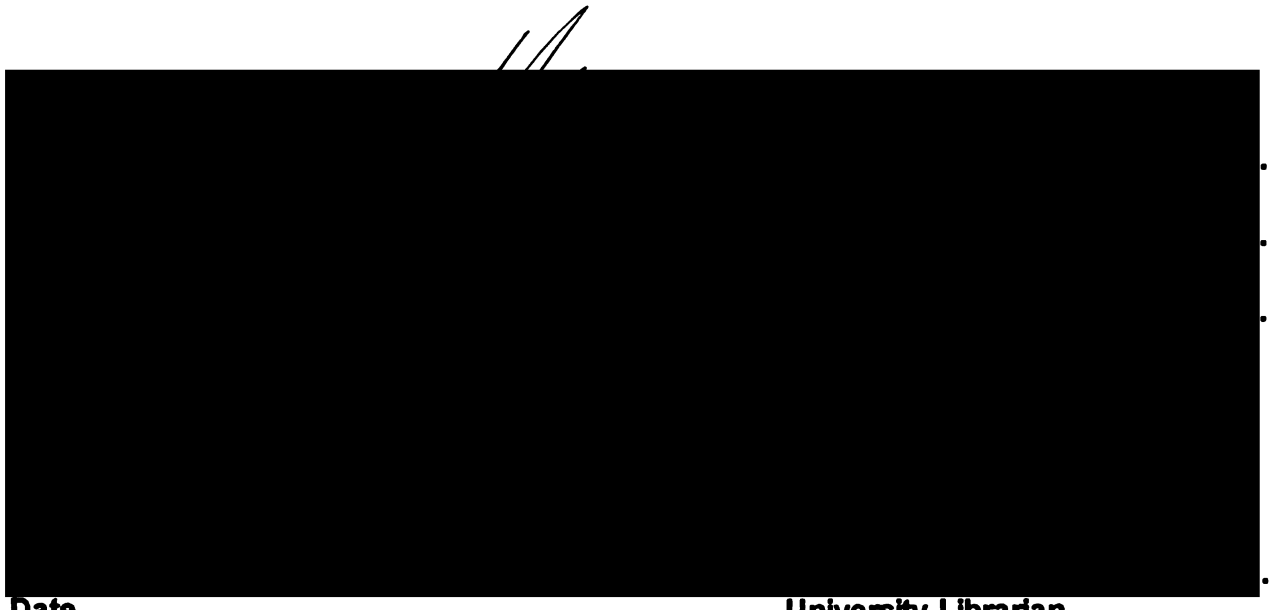

Date **University Librarian**

Degree Conferred: . . . . . .

To my Father,

who gave his all to educate us.

Acknowledgments

There are many persons I would like acknowledge for helping me fulfill by academic dream. In chronological order, they are, Dr. James Lockhart, who taught me the how to do interesting physics. Dr. Alex Grillo and Dr. Guido Galli, who taught me to how do physics productively. Dr. Bill Dewey, who taught me to how to do biophysics. Dr. Joe Carlson, who coached me through the intricacies of MRI physics. Dr. Hector Avram, who helped me apply MRI. Dr. Larry Crooks, who taught me the engineering in MRI. And Dr. Leon Kaufman, who gave me the resources and guidance to do science in MRI. I also want to thank the others at RIL for the happy and enjoyable times I had as a graduate student. I want acknowledge my appreciation to the guys in Biophysics. And lastly, I want to thank family and friends for providing the support and encouragement when I needed it.

Abstract

In Vivo Cross Relaxation Phenomenon in the Field Range of 340-1000 Gauss

Kingman Yee

Magnetic resonance imaging experiments using two female Fischer rat lesion models to study in-vivo cross relaxation phenomenon in the field range of 340-1000 Gauss. The first model compared relaxation in edema induced by a cold probe to a normal brain. The edema induced was of the vasogenic type where the extraneous fluid was in the extracellular matrix. This caused a breakdown of the blood-brain barrier, allowing large macromolecules into the brain that are normally prohibited. The second model was an adenocarcinoma of the breast grown subcutaneously in the thigh. MR images of live rats were acquired using a CPMG pulse sequence and two echoes, TE = 40 and 100 ms, were obtained in each sequence. Two TR's, 900 and 150 ms, were used and chosen to minimize the error due to a two point measurement. The relaxation parameters were calculated from these images. T_1 and T_2 NMRDs were obtained and compared to a quadrupolar crossed relaxation model for both in-vivo systems.

Nitrogen cross relaxation is clearly visible in the muscle T_1 nuclear magnetic resonance dispersion curve (NMRD), showing a pair of peaks at 489 and 653 Gauss while the adenocarcinomas did not show any peaks. The edematous and normal brain T_1 NMRDs both show a single peak with at a slightly different frequency, otherwise the two NMRDs differ only by a scale factor. The evidence of peaks shows that cross relaxation can be a contributor to T_1 relaxation values. None of the T_2 NMRDs show nitrogen cross relaxation peaks. The dispersion for T_1 for all models is a monotonic increasing function. The dispersion for T_2 is generally a monotonic decreasing function for normal brain, edematous brain, and muscle. Tumor's T_2 dispersion was not detected in this field range.

Keywords: MRI, relaxometry, cross relaxation, quadrupolar cross relaxation, edema, adenocarcinoma, cold probe.

Table of Contents

List of Tables

List of Figures

Introduction

A diagnostic image requires contrast between normal tissue and lesion, along with good signal to noise ratios. For example, a brain image with excellent resolution and signal to noise ratio (S/N) will be of little use to a radiologist if the image does not show any contrast between edematous and normal brain. Protons in water are the primary signal contributors in diagnostic MRIs. Contrast in MRI depends on three parameters, spin-lattice relaxation (T_1), spin-spin relaxation (T_2), and hydrogen density. The two relaxation parameters can have a profound effect on contrast. The classic example is the brain [*1*], in which the hydrogen density difference between white and gray matter is small (15%) compared to the larger differences in T_1 relaxation times at low fields (>300%). This difference in relaxation time is different at different fields. The dispersion in relaxation times changes the image's contrast and intensity at different imaging fields. Optimizing image qualities such as S/N and contrast requires prior knowledge of the tissue's relaxation times at the imaging frequencies. Low field images may have a lower S/N as compared to high field images, but contrast in low field images can be substantially better than in high field images.

Contrast at high field is predominately differences in T_2 and hydrogen density. This means that for tissue with similar water content, the contrast mechanism appearing in high field images is primarily differences in T_2's. T_1's of tissue at high field are not very different (within a factor 2) to the T_1 of plain water, while the difference at low field can be larger than a factor of 5. Good T_1 contrast is confined mainly to low field imagers, hence, low field imagers have the luxury of all three contrast producing parameters.

What causes relaxation dispersion is not at all clear. Theoretical studies have shown that relaxation rates are intimately tied to molecular motion. Water protons have very short correlation times (~1ps) and have no dispersion at both high and low fields. Introducing protein solutes into plain water induces relaxation changes. Calculations of relaxation rates of simple solutions can be done, but calculating relaxation rates of tissue from first principles is still not possible because of

the complexity of tissue. The mechanism producing the different relaxation rates among similar tissues is not fully understood. Measuring phenomenological parameters and speculating functional forms and applying these values and ideas to mathematical models to fit the relaxation dispersion's functional forms are common procedures.

The typical T_1 relaxation rate dispersion curve is a montonic decreasing function with a functional form $1/\omega^{\beta}$. The NMRD is smooth except in the Larmor frequency of 1.6-3 MHz where a pair of peaks represent increases in relaxation rates. The cause of the increased relaxation rate is proton coupling to nitrogen. Nitrogen has a quadrupole moment and, in the motional narrowed limit, has three transition levels that are independent of frequency. An additional relaxation path is available to the proton when the frequency dependent dipolar relaxation of proton coincides with that of the nitrogen quadrupolar frequencies. The quadrupolar rate is considerably faster than the dipolar rate thus providing the proton an additional relaxation pathway.

These experiments investigate the in-vivo T_1 and T_2 NMRD profiles and the anomalous nitrogen peaks using imaging techniques. Two lesion models are used to determine in-vivo values of relaxation dispersion curves. One is a rat brain edema and the other is an adenocarcinoma of the breast. The edema is induced by cold injury using a liquid nitrogen cooled probe. The edema induced is of the vasogenic type where the extraneous fluid is in the extracellular matrix and is caused by the breakdown of the blood-brain barrier, allowing large macromolecules into the brain that are normally prohibited. The second model is an adenocarcinoma of the breast grown subcutaneously in the thigh. T_1 relaxation of tumors is generally longer than the tissue where the tumors originate. The T_1 NMRD profile of adenocarcinoma of the breast has a different functional form than that of normal breast tissues. This result is not surprising considering that the major constituent of breast tissue is adipose cells. Adipose T_1 NMRD profile is very much different from that of typical normal tissues. The profile of breast tumor is more like that of tissue than adipose since the tumor's origin is most likely epithelial.

T_2 NMRD profiles are scarce because typical NMRD profiles are obtained by use of a field cycling relaxometer. Machines of this type can only provide T_1 values automatically, and are in-vitro type machines. In-vivo NMRD profiles are virtually non-existent. This experiment provides in-vivo NMRD profiles of both T_1 and T_2. The typical number of rats per frequency is 25, thus providing a larger population average than the ones provided by previous work that have very small samples (typically one). The frequencies spanned by this experiment are 1.5 to 4.5 MHz with points chosen to coincide with the nitrogen cross relaxation peaks. The procedure has MR images of live rats acquired using a CPMG pulse sequence with two echoes obtained with

each sequence. Two sequences with different TRs are used for a total of four images. The relaxation parameters are calculated from these images. Viewing the images allows more precise location of the lesions thus providing more accurate lesion relaxation values. In vivo experiments eliminate the excision delays and physiological changes due to excision that are inherent in in-vitro experiments. Because the total span of fields is relatively small, the hardware and pulse sequence were consistent at all fields. TR and TE value were kept the same through out the experiments.

Chapter 1

Dynamics of a Spin 1/2 Particle

The imaging done in this project is of protons, which are spin 1/2. Other nuclei, including those with spin greater than 1/2, can be used for imaging but other nuclei images generally have poor resolution and are confined to mostly spectroscopy studies because of their low densities and gyromagnetic ratios. The dynamics of a spin 1/2 particle can be described both classically and quantum mechanically. Quantum mechanics must be used to describe the dynamics of a particle with a spin greater than 1/2. The classical solutions are expressed by the Bloch equations for all but a few cases. Both methods produce the same solution for a spin 1/2 particle but with some limitations for the classical method. The Bloch equations are almost exclusively used in image calculations because of the simplicity they offer compared to the quantum derivations. Both methods will be presented here showing the equivalencies of the two methods for a spin echo experiment using spin 1/2 particles.

Classical model

An object with angular momentum experiencing a force will precess and the dynamics of this precession can be calculated in a straight forward manner using classical methods. A magnetic moment in an external magnetic field will experience a torque. The equation of motion of a magnet moment in a static magnetic field is given as,

$$\frac{dJ}{dt} = \mu \times H \qquad \text{Eqn 1.1}$$

where J is the angular momentum and H is the magnetic field. Substituting $\mu = \gamma J$, the equation of motion becomes,

$$\frac{d\mu}{dt} = \mu \times (\gamma H) \qquad \text{Eqn 1.2}$$

Use of a rotating frame transformation will facilitate the solution of this differential equation. The time derivative of a function $F(t)$ in rectangular coordinate is

$$\begin{aligned} \frac{dF}{dt} &= i\frac{dF_x}{dt} + F_x\frac{di}{dt} + j\frac{dF_y}{dt} + F_y\frac{dj}{dt} + k\frac{dF_z}{dt} + F_z\frac{dk}{dt} \\ &= i\frac{dF_x}{dt} + j\frac{dF_y}{dt} + k\frac{dF_z}{dt} + \omega \times (iF_x + jF_y + kF_z) \\ &= \frac{\delta F}{\delta t} + \omega \times F \end{aligned} \qquad \text{Eqn 1.3}$$

In the lab frame, $\frac{dF}{dt}$ can be separated into pair of terms with first term as the rate of change of F and the second is the motion of the rotating frame. Substituting for F in equation 1.3 in terms of μ, we have

$$\begin{aligned} \frac{\delta \mu}{\delta t} + \omega \times \mu &= \mu \times \gamma H \\ \frac{\delta \mu}{\delta t} &= \mu \times (\omega + \gamma H) \end{aligned} \qquad \text{Eqn 1.4}$$

Equation 1.4 has the same form as equation 1.2, that is, the one in the laboratory reference frame, but with the H being replaced by an effective field H_{eff}, where

$$H_{eff} = \omega + \gamma H \qquad \text{Eqn 1.5}$$

hence,

$$\frac{\delta \mu}{\delta t} = \mu \times H_{eff} \qquad \text{Eqn 1.6}$$

If we pick a value of ω such that H_{eff} is zero, that is ,

$$\omega = -\gamma H \qquad \text{Eqn 1.7}$$

the magnetization vector in the rotating frame is stationary. This implies that the magnetization vector is rotating in the laboratory at an angular frequency of $-\gamma H$, which is the called the *Larmor frequency*.

The magnetization can be perturbed by an application of an alternating magnetic field close to the Larmor frequency, i.e., close to resonance. The analysis begins with the decomposition of a non-selective alternating magnetic field $H_1(t) = H_1 \cos \omega t$,

$$\begin{aligned} H_+ &= H_1(\boldsymbol{i}\cos\omega t + \boldsymbol{j}\sin\omega t) \\ H_- &= H_1(\boldsymbol{i}\cos\omega t - \boldsymbol{j}\sin\omega t) \end{aligned} \qquad \text{Eqn 1.8}$$

since H_- is out of phase with the Larmor precession, only the H_+ will have effect on the magnetization. Renaming H_+ as $\boldsymbol{H}_1$,

$$\boldsymbol{H}_1 = H_1(\boldsymbol{i}\cos\omega_z t + \boldsymbol{j}\sin\omega_z t) \qquad \text{Eqn 1.9}$$

Including $\boldsymbol{H}_1$ into Eqn 1.2 gives,

$$\frac{d\mu}{dt} = \mu \times \gamma[\boldsymbol{H}_0 + \boldsymbol{H}_1(t)] \qquad \text{Eqn 1.10}$$

The time dependence of $\boldsymbol{H}_1$ is eliminated by choosing ω of the rotating frame such that is coincides with the angular frequency of $\boldsymbol{H}_1$. In the rotating frame,

$$\begin{aligned} \frac{\delta\mu}{\delta t} &= \mu \times \boldsymbol{H}_{total} \\ &= \mu \times [\boldsymbol{k}(\omega_z + \gamma H_0) + \boldsymbol{i}\gamma H_1] \end{aligned} \qquad \text{Eqn 1.11}$$

defining $\omega_z = -\omega$,where ω is positive,

$$\frac{\delta\mu}{\delta t} = \mu \times \boldsymbol{H}_{eff} \qquad \text{Eqn 1.12}$$

where

$$\boldsymbol{H}_{eff} = \boldsymbol{k}(H_0 - \frac{\omega}{\gamma}) + \boldsymbol{i}H_1 \qquad \text{Eqn 1.13}$$

The magnetization is precessing about H_{eff}. Near resonance, i.e., $H_0 \approx \omega/\gamma$, the k term is roughly zero thereby the magnetization effectively sees only the transverse alternating field. The transverse component is stationary in this frame.

Effects of a $\pi/2$ - π pulse pair

At resonance frequency, $H_0 = \omega/\gamma$ will cancel the k component giving $H_{eff} = iH_1$. The $\pi/2_x$ pulse (about the x axis) at resonance is a H_1 pulse that rotates the ("precessing") magnetization vector 90° about the x axis to lie on the y axis. The amplitude and duration of a θ pulse at resonance is,

$$\theta = \gamma H_1 t \qquad \text{Eqn 1.14}$$

for a $\pi/2$ pulse the pulse duration is,

$$t = \frac{\pi}{2\gamma H_1} \qquad \text{Eqn 1.15}$$

for typical imaging systems, the $H_1 \approx 0.5$ gauss, giving the typical $\pi/2$ pulse length to be

$$t_{\pi/2} \approx \frac{\pi}{2 \cdot 4258 \ {}^{Hz}/_{Gauss} \cdot 0.5 \text{ Gauss}} \approx 738.0 \ \mu\text{Sec} \qquad \text{Eqn 1.16}$$

with the π pulse being twice as long.

Main field inhomogeneities cause transverse magnetization to dephase. The dephasing will reduce the amplitude of the MR signal as time progress. The free induction decay (FID) describes the decay of the MR signal where the amplitude of the FID decays with the a time constant T_2^* (which is described in the following paragraph). A spin echo is created by application of another H_1 pulse of t_π duration along the x axis (it could be along the y-axis) which rotates the magnetization about the x-axis to lie on the -y axis.

A spin echo can be conceptualized with a spin vector in the rotating frame rotating with an angular frequency of $\omega = \gamma H_0$. This spin vector is stationary in the rotating frame because it is on resonance. If at $t = 0$ the spin is in the direction of the x axis, it will stay pointing along the x axis. Its neighbors that see a slightly different static field, $H_0 + \Delta H$, and will rotate with a angular frequency higher by the amount $\Delta\omega = \gamma\Delta H$. The net effect is the faster neighbor will drift in the positive direction, i.e., the phase relative to the on resonance spins will increase with time. The phase difference between the faster spins and on resonance spins at a time t is

$$\varphi = \int_0^t \Delta\omega dt \qquad \text{Eqn 1.17}$$

and for constant field inhomgeneities, that is when ΔH is a constant the phase difference becomes

$$\begin{aligned} \varphi &= \int_0^t \gamma\Delta H dt = \gamma\Delta H \int_0^t dt \\ &= \gamma\Delta H t \end{aligned} \qquad \text{Eqn 1.18}$$

The same effects will occur for neighboring spins at a field lower by $\Delta\omega = -\gamma\Delta H$ except that the dephasing will be in the opposite direction. These effects produce the rapid decay of the signal, usually much faster than T_2. This faster relaxation time is given the name of T_2^*. It includes T_2 and *all* factors contributing to the dephasing process.

Applying a π_y pulse will invert the magnetization about the y axis. The spin that was pointing along the x axis will now point in the -x axis. The faster and slower neighbors will also be inverted but the faster ones will now have a negative phase shift relative to the original spin and the slower ones will have a positive phase shift. At time $2t$, the faster spin will make up the negative phase shift cause by the π pulse and the slower spins will lose the same amount of phase shift. The net effect of the π pulse is to cause the spins to coalesce at time $2t$ producing a signal, hence the term echo. The magnitude of the echo has decreased by an amount caused by the irreversible processes and reflects the true T_2 relaxation. An important irreversible process is the molecular diffusion effect. The refocusing requires that the spins remain a constant static magnetic field but if the spins are moving, the field they encounter is constantly changing. This produces an irreversible phase shift due to diffusion which needs to be included in the relaxation term.

Bloch Equations

The previous section did not include magnetization relaxation. The calculation assumed that the relaxation was long relative to the time of the pulses so the final magnetization was not any different from prior to the application of the pulses. Taking relaxation into account, Felix Bloch [2] proposed that the longitudinal magnetization, M_Z, returns to equilibrium as a first ordered process such that

$$\frac{dM_z}{dt} = \frac{M_0 - M_z}{T_1} \qquad \text{Eqn 1.19}$$

where M_O is the equilibrium magnetization and T_1 is the longitudinal relaxation time. Applying a static magnetic field in the z direction produces a torque according to equation 1.2,

$$\frac{dM_z}{dt} = \frac{M_0 - M_z}{T_1} + \gamma(\boldsymbol{M} \times \boldsymbol{H})_z \qquad \text{Eqn 1.20}$$

and the transverse components also vanish but with a different relaxation time, the transverse relaxation T_2,

$$\begin{aligned} \frac{dM_x}{dt} &= \gamma(\boldsymbol{M} \times \boldsymbol{H})_x - \frac{M_x}{T_2} \\ \frac{dM_y}{dt} &= \gamma(\boldsymbol{M} \times \boldsymbol{H})_y - \frac{M_y}{T_2} \end{aligned} \qquad \text{Eqn 1.21}$$

Transforming the equations to a frame rotating at ω, and having H_1 along the x axis,

$$\begin{aligned} \frac{dM_z}{dt} &= \gamma M_y H_1 + \frac{M_0 - M_z}{T_1} \\ \frac{dM_x}{dt} &= \gamma M_y \left(H_0 + (\frac{\omega}{\gamma}) \right) - \frac{M_x}{T_2} \\ \frac{dM_y}{dt} &= \gamma \left\{ M_z H_1 - M_x \left(H_0 + (\frac{\omega}{\gamma}) \right) \right\} - \frac{M_y}{T_2} \end{aligned} \qquad \text{Eqn 1.22}$$

replacing $h_0 = H_0 + \left(\frac{\omega}{\gamma}\right)$,

$$\frac{dM_z}{dt} = \gamma M_y H_1 + \frac{M_0 - M_z}{T_1}$$
$$\frac{dM_x}{dt} = \gamma M_y h_0 - \frac{M_x}{T_2} \qquad \text{Eqn 1.23}$$
$$\frac{dM_y}{dt} = \gamma\{M_z H_1 - M_x h_0\} - \frac{M_y}{T_2}$$

We have Bloch equations in a rotating frame.

The dynamic behavior of the transverse magnetization is the interesting component since it is the one detected by the receiver coil. The analysis of the dynamic behavior of the transverse magnetization begins with replacing $M_+ = M_x + iM_y$ and summing the last two equations of equation 1.23 gives,

$$\begin{aligned}\frac{dM_+}{dt} &= \frac{dM_x}{dt} + i\frac{dM_y}{dt} \\ &= \gamma M_y h_0 - \frac{M_x}{T_2} + i\gamma(M_z H_1 - M_x h_0) - \frac{iM_y}{T_2} \qquad \text{Eqn 1.24} \\ &= i\gamma M_z H_1 - M_+\left(i\gamma h_0 + \frac{1}{T_2}\right)\end{aligned}$$

solving

$$\int \frac{dM_+}{i\gamma M_z H_1 - M_+\left(i\gamma h_0 + \frac{1}{T_2}\right)} = \int dt \qquad \text{Eqn 1.25}$$

we get

$$M_+ = Ce^{-(i\gamma h_0 + 1/T_2)t} + \frac{i\gamma M_z H_1}{i\gamma h_0 + 1/T_2} \qquad \text{Eqn 1.26}$$

for the steady state solution, that is when $t \to \infty$, we have

$$M_x = \mathrm{Re}(M_+) = \frac{\gamma^2 H_1 h_0 M_z T_2^2}{1 + \gamma^2 h_0^2 T_2^2} \qquad \text{Eqn 1.27}$$

and

$$M_y = \mathrm{Im}(M_+) = \frac{\gamma H_1 M_z T_2}{1+\gamma^2 h_0^2 T_2^2} \qquad \text{Eqn 1.28}$$

replacing $\omega_0 = \gamma H_0$, $M_0 = \chi_0 H_0$, and $h_0 = H_0 + \left(\frac{\omega}{\gamma}\right)$ we have the magnitude component as,

$$\begin{aligned} M_x &= \frac{\gamma^2 H_1 \left(H_0 + (\omega/\gamma)\right) M_z T_2^2}{1+\gamma^2 \left(H_0 + (\omega/\gamma)\right)^2 T_2^2} \\ &= \frac{(\omega_0 - \omega)\chi_0 \omega_0 T_2^2 H_1}{1+(\omega-\omega_0)^2 T_2^2} \end{aligned} \qquad \text{Eqn 1.29}$$

and the dispersion component is,

$$\begin{aligned} M_y &= \frac{\gamma H_1 M_z T_2}{1+\gamma^2 h_0^2 T_2^2} M_y \\ &= \frac{\chi_0 \omega_0 T_2 H_1}{1+(\omega-\omega_0)^2 T_2^2} \end{aligned} \qquad \text{Eqn 1.30}$$

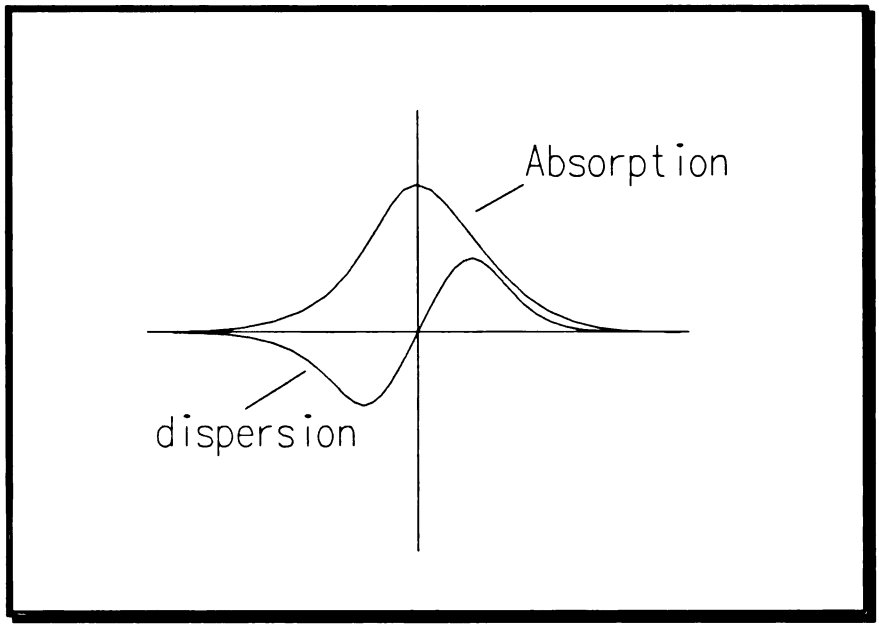

Figure 1.1
Graph of the real and imaginary components of transverse magnetization.

Figure 1.1 shows the relationship of the two signals showing that the basic characteristic of the full width at half maximum is equal to $1/(\pi T_2^*)$.

Quantum Mechanical Model

The classical solution is well adept for spin 1/2 nuclei but has limitations (it fails for T_2's of solids with spin 1/2) but for nuclei with spin larger than 1/2, a quantum solution must be sought. ^{14}N with spin=1 falls into this category. The items of interest in quantum mechanical calculations are the dynamics of expectation values rather than the values themselves. The expectation values, in a particular representation, can be found with the aid of a wave function. Calculating the dynamics of the expectation value of an ensemble of nuclei are facilitated by the use of the density matrix.

The general time dependent wave function $\Psi(t)$ can be written in the form,

$$\Psi(t) = \sum_{m=-I}^{+I} c_m u_{I,m} e^{-(i/\hbar)E_m t} \qquad \text{Eqn 1.31}$$

Where the c_m's are complex constants, $u_{I,m}$'s are the time independent eigenfunctions, and E_m's are the transitional energies,

$$E_m = -\gamma\hbar H_0 m \qquad \text{Eqn 1.32}$$

The expectation value of the magnetic moment μ_x is given by

$$\langle \mu_x(t) \rangle = \int_{-\infty}^{+\infty} \Psi^*(t) \mu_x \Psi(t) d\tau \qquad \text{Eqn 1.33}$$

Substituting $\mu_x = \gamma\hbar I_x$ and equation 1.31 for $\Psi(t)$ gives

$$\begin{aligned} \langle \mu_x(t) \rangle &= \gamma\hbar \int_{-\infty}^{+\infty} \sum_{m=-I}^{+I} c^*_m u_{I,m} e^{(i/\hbar)E_m t} I_x \sum_{m=-I}^{+I} c_m u_{I,m} e^{-(i/\hbar)E_m t} d\tau \\ &= \sum_{m,m'} \gamma\hbar c^*_{m'} c_m \langle m' | I_x | m \rangle e^{(i/\hbar)(E_{m'} - E_m)t} \end{aligned} \qquad \text{Eqn 1.34}$$

Where

$$\langle m'|I_x|m\rangle = \int_{-\infty}^{\infty} u^*_{i,m'} I_x u_{i,m} d\tau \qquad \text{Eqn 1.35}$$

is a time-independent matrix. Equation 1.34 is applicable to all values of spins. Presenting an example for a spin 1/2 nucleus will euclidate the process of a solution using this method. A spin 1/2 particle has the matrix

$$\langle m'|I_x|m\rangle = \begin{bmatrix} 0 & \frac{1}{2} \\ \frac{1}{2} & 0 \end{bmatrix} \qquad \text{Eqn 1.36}$$

giving

$$\begin{aligned} \langle \mu_x(t)\rangle &= \gamma\hbar c^*_{m'} c_m \begin{bmatrix} 0 & \frac{1}{2} \\ \frac{1}{2} & 0 \end{bmatrix} e^{(i/\hbar)(E_{m'}-E_m)t} \\ &= \gamma\hbar[c^*_{\frac{1}{2}} c_{-\frac{1}{2}} e^{i\omega t} + c^*_{-\frac{1}{2}} c_{\frac{1}{2}} e^{i\omega t}] \end{aligned} \qquad \text{Eqn 1.37}$$

The equation of motion is given as

$$\begin{aligned} \frac{dI_x}{dt} &= \frac{i}{\hbar}[\mathcal{H}, I_x] \\ &= \frac{i}{\hbar}[-\gamma\hbar H_0 I_z, I_x] \\ &= -\gamma H_0 i[I_z, I_x] \\ &= \gamma H_0 I_y \end{aligned} \qquad \text{Eqn 1.38}$$

and

$$\begin{aligned} \frac{dI_y}{dt} &= -\gamma H_0 I_x \\ \frac{dI_z}{dt} &= 0 \end{aligned} \qquad \text{Eqn 1.39}$$

where $\mathcal{H}$ is the Hamiltonian. Grouping the three components of I, we get,

$$\frac{dI}{dt} = i\frac{dI_x}{dt} + j\frac{dI_y}{dt} + k\frac{dI_z}{dt}$$
$$= \gamma H_0 \left(iI_y - jI_x \right) \qquad \text{Eqn 1.40}$$

replacing $\mu = \gamma \hbar I$, gives

$$\frac{d\langle \mu \rangle}{dt} = \langle \mu \rangle \times \gamma H \qquad \text{Eqn 1.41}$$

which is the same as the classical equation, eqn. 1.2, except for the concept of the expectation value of μ replacing "μ".

Spin temperature

The concept of spin temperature (distinct from lattice temperature) is used in cases where the spin system can be thought as a single spin system with many degrees of freedom. This occurs in solids where the spins are tightly coupled and assumes that the spin temperature is obtained rapidly relative to $T1$. The T_1 relaxation is given in a rather elegant fashion as [13]

$$\frac{1}{T_1} = \frac{1}{2} \frac{\sum_{m,n} W_{mn} (E_m - E_n)^2}{\sum_n E_n^2} \qquad \text{Eqn 1.42}$$

where W_{mn} is the transitional probability of m→n, and E_m is the energy of state m. For systems where spin temperatures apply, the longitudinal relaxation time can be calculated from the transitional probabilities. Spin temperature a powerful tool in relaxation calculations where a problem can be reduced to a simpler thermodynamics problem.

Density Matrix

The technique of density matrix is useful when the concept of spin temperature is not applicable such as motionally narrowed fluids. The density matrix is needed because we need an *incoherent*

superposition of states rather than a *coherent* superposition of states. A coherent superposition of states is an ensemble of N systems all in the same state. An incoherent superposition of states is an ensemble of N systems with n_i items in the state $|i\rangle$. The expectation of an observable M is given by

$$\langle M_x \rangle = \langle \psi | M_x | \psi \rangle \qquad \text{Eqn 1.43}$$

where $\psi(t)$ is defined in a time independent complete orthonormal basis u_n, and the time dependence is carried by the c_n's,

$$\psi(t) = \sum_n c_n(t) u_n \qquad \text{Eqn 1.44}$$

A distinction is made between an average of expectation values of an observable and the expectation of the average of an observable. What is needed is the average expectation value of M_x. Denoting the average with an overhead bar which represents a classical average over the systems in different states $|i\rangle$, the average expectation value of M_x is

$$\begin{aligned} \langle \overline{M}_x \rangle &= \langle \psi | \overline{M}_x | \psi \rangle \\ &= \sum_{n,m} \overline{c_m^* c_n} \langle m | M_x | n \rangle \\ &= \sum_{n,m} \overline{\langle n | P | m \rangle} \langle m | M_x | n \rangle \end{aligned} \qquad \text{Eqn 1.45}$$

where P is defined as

$$\langle n | P | m \rangle = \sum_{n,m} c_m^* c_n \qquad \text{Eqn 1.46}$$

and $\overline{P}$ is

$$\begin{aligned} \overline{\langle n | P | m \rangle} &= \sum_{n,m} \overline{c_m^* c_n} \\ &= \overline{\langle m | P | n \rangle} \end{aligned} \qquad \text{Eqn 1.47}$$

this gives us the definition of the density matrix, denoted by ρ, as

$$\langle n|\rho|m\rangle = \overline{\langle n|P|m\rangle} \qquad \text{Eqn 1.48}$$

$$\begin{aligned}\langle \overline{M}_x \rangle &= \sum_{n,m} \langle n|\rho|m\rangle\langle m|M_x|n\rangle \\ &= \sum_{n} \langle n|\rho M_x|n\rangle \\ &= \mathrm{Tr}\{\rho M_x\} = \mathrm{Tr}\{M_x\rho\}\end{aligned} \qquad \text{Eqn 1.49}$$

The density matrix has the properties that it is Hermitian, positive and has a trace of 1. The density matrix can be expanded in a basis dependent form,

$$\rho = \sum_i p_i \rho \qquad \text{Eqn 1.50}$$

where p_i is the probability that the system is in state i.

The dynamics of spins can be calculated with the help of the density matrix and is not restricted to spins equal to ½. To calculate the effects of a spin echo, consider an ensemble of ½ spins, biased with an external magnetic field, B_o, at a temperature T. The spins are either in the upper or lower state. The density matrix of identical ½ spins is a 2x2 matrix of the form

$$\rho = \begin{bmatrix} \rho_{11} & \rho_{12} \\ \rho_{21} & \rho_{22} \end{bmatrix} \qquad \text{Eqn 1.51}$$

The diagonal elements are the spin density of the upper and the lower states and the off diagonal elements are mixtures of both. The elements can be found with the help of eqn. 1.50 .

Denoting the energy when the spin is parallel to the magnetic field as E_0, and the energy when the spin is anti-parallel to magnetic field as E_1, the energies are

$$\begin{aligned} E_0 &= \langle \Psi_0 | \mathcal{H} | \Psi_0 \rangle = -\frac{\gamma B_0 \hbar}{2} \\ E_1 &= \langle \Psi_1 | \mathcal{H} | \Psi_1 \rangle = +\frac{\gamma B_0 \hbar}{2} \end{aligned} \qquad \text{Eqn 1.52}$$

and the equilibrium population are

$$n_i = \frac{e^{-E_i/kT}}{Z} \qquad \text{Eqn 1.53}$$

where Z is the grand conical partition function, and is equal to one. Expanding the exponential in equation 1.53 gives,

$$n_i = 1 - \frac{E_i}{kT} + \frac{1}{2!}\left(\frac{E_i}{kT}\right)^2 - \frac{1}{3!}\left(\frac{E_i}{kT}\right)^3 + \ldots\ldots \qquad \text{Eqn 1.54}$$

Because at room temperature the energies E_i are much less than kT, only the first order terms are kept. The equilibrium occupations are

$$\begin{aligned} n_1 &= \frac{1}{2} + \frac{\gamma\hbar B_0}{2kT} \\ n_2 &= \frac{1}{2} - \frac{\gamma\hbar B_0}{2kT} \end{aligned} \qquad \text{Eqn 1.55}$$

The density matrix for a spin ½ particle for upper (α) state and the lower (β) state are

$$\rho^{\alpha} = \begin{bmatrix} 1 & 0 \\ 0 & 0 \end{bmatrix}, \qquad \rho^{\beta} = \begin{bmatrix} 0 & 0 \\ 0 & 1 \end{bmatrix} \qquad \text{Eqn 1.56}$$

and the each having an equal probability of being occupied gives the density matrix as,

$$\rho = \frac{1}{2}\rho^{\alpha} + \frac{1}{2}\rho^{\beta} = \begin{bmatrix} \frac{1}{2} & 0 \\ 0 & \frac{1}{2} \end{bmatrix} \qquad \text{Eqn 1.57}$$

This gives the density matrix as,

$$\rho = \sum_i p_i \rho^i = p_1 \rho^\alpha + p_2 \rho^\beta$$

$$= p_1 \begin{bmatrix} 1 & 0 \\ 0 & 0 \end{bmatrix} + p_2 \begin{bmatrix} 0 & 0 \\ 0 & 1 \end{bmatrix} = \begin{bmatrix} \frac{1}{2} + \frac{\gamma\hbar B_0}{kT} & 0 \\ 0 & \frac{1}{2} - \frac{\gamma\hbar B_0}{kT} \end{bmatrix}$$

$$= \frac{1}{2}\begin{bmatrix} 1 & 0 \\ 0 & 0 \end{bmatrix} + \frac{1}{2}\begin{bmatrix} \frac{\gamma\hbar B_0}{kT} & 0 \\ 0 & -\frac{\gamma\hbar B_0}{kT} \end{bmatrix}$$

Eqn 1.58

rewriting in terms of the Pauli matrices ,σ_i,

$$\rho = \frac{1}{2}\left(\sigma_0 + \frac{\gamma\hbar B_0}{kT}\sigma_z\right)$$

Eqn 1.59

where the three Pauli matrices are defined as,

$$\sigma_x = \begin{bmatrix} 0 & 1 \\ 1 & 0 \end{bmatrix}, \quad \sigma_x = \begin{bmatrix} 0 & -i \\ i & 0 \end{bmatrix}, \quad \sigma_z = \begin{bmatrix} 1 & 0 \\ 0 & 1 \end{bmatrix}$$

Eqn 1.60

Only the second term contributes to the detected signal. This term is given the label magnetization density matrix and is denoted as ξ and ξ_0 is the equilibrium magnetization matrix,

$$\xi_0 = \frac{\gamma\hbar B_0}{2kT}\sigma_z$$
$$= \frac{\gamma\hbar B_0}{2kT}\begin{bmatrix} 1 & 0 \\ 0 & -1 \end{bmatrix}$$

Eqn 1.61

Effects of a π/2-π pulse pair

Applying a π/2 pulse, on resonance, and along the x-axis produces a rotation about the x-axis in the counter clockwise direction (following the right hand rule convention). The angle of rotation will depend on the duration and amplitude of the pulse. The effects of applying a -π/2 pulse about

the x axis to the magnetization density matrix, ξ can be determined with the help of the rotation matrices $U_{\varphi x}$, and is given as

$$\begin{aligned}
\xi_{-\pi/2} &= U_{-(\pi/2)x}\,\xi_0\,U^{-1}_{-(\pi/2)x} \\
&= \frac{\gamma\hbar B_0}{2kT}\begin{bmatrix} \cos(-\pi/4) & -i\sin(-\pi/4) \\ -i\sin(-\pi/4) & \cos(-\pi/4) \end{bmatrix}\begin{bmatrix} 1 & 0 \\ 0 & -1 \end{bmatrix}\begin{bmatrix} \cos(-\pi/4) & i\sin(-\pi/4) \\ i\sin(-\pi/4) & \cos(-\pi/4) \end{bmatrix} \\
&= \frac{\gamma\hbar B_0}{2kT}\frac{\sqrt{2}}{2}\begin{bmatrix} 1 & i \\ i & 1 \end{bmatrix}\begin{bmatrix} 1 & 0 \\ 0 & -1 \end{bmatrix}\begin{bmatrix} 1 & -i \\ -i & 1 \end{bmatrix} = \frac{\sqrt{2}\gamma\hbar B_0}{2kT}\begin{bmatrix} 0 & -i \\ i & 0 \end{bmatrix} \\
&= \frac{\sqrt{2}\gamma\hbar B_0}{2kT}\sigma_y
\end{aligned} \qquad \text{Eqn 1.62}$$

the evolution of spin during the interval between the $\pi/2$ and π pulse is given by

$$\begin{aligned}
\xi_\tau &= U_{\mathcal{H}}\,\xi_{\pi/2}\,U^{-1}_{\mathcal{H}} \\
&= \frac{\sqrt{2}\gamma\hbar B_0}{2kT}\begin{bmatrix} e^{-i(\Omega-\omega)\tau/2} & 0 \\ 0 & e^{i(\Omega-\omega)\tau/2} \end{bmatrix}\begin{bmatrix} 0 & -i \\ i & 0 \end{bmatrix}\begin{bmatrix} e^{i(\Omega-\omega)\tau/2} & 0 \\ 0 & e^{-i(\Omega-\omega)\tau/2} \end{bmatrix} \\
&= \frac{\sqrt{2}\gamma\hbar B_0}{2kT}\begin{bmatrix} 0 & -ie^{-i(\Omega-\omega)\tau/2} \\ ie^{i(\Omega-\omega)\tau/2} & 0 \end{bmatrix}
\end{aligned} \qquad \text{Eqn 1.63}$$

Applying a π pulse along the y axis at $t = \tau$gives,

$$\begin{aligned}
\xi_\pi &= U_{\pi y}\,\xi_\tau\,U^{-1}_{\pi y} \\
&= \frac{\sqrt{2}\gamma\hbar B_0}{2kT}\begin{bmatrix} 0 & -1 \\ 1 & 0 \end{bmatrix}\begin{bmatrix} 0 & -ie^{-i(\Omega-\omega)\tau/2} \\ ie^{i(\Omega-\omega)\tau/2} & 0 \end{bmatrix}\begin{bmatrix} 0 & -1 \\ 1 & 0 \end{bmatrix} \\
&= \frac{\sqrt{2}\gamma\hbar B_0}{2kT}\begin{bmatrix} 0 & ie^{-i(\Omega-\omega)\tau/2} \\ -ie^{i(\Omega-\omega)\tau/2} & 0 \end{bmatrix}
\end{aligned} \qquad \text{Eqn 1.64}$$

Evolving for an another time τ for total time 2τ,

$$\xi_{2\tau} = \frac{\sqrt{2}\gamma\hbar B_0}{2kT}\begin{bmatrix} e^{-i(\Omega-\omega)\tau/2} & 0 \\ 0 & e^{i(\Omega-\omega)\tau/2} \end{bmatrix}\begin{bmatrix} 0 & ie^{i(\Omega-\omega)\tau/2} \\ -ie^{-i(\Omega-\omega)\tau/2} & 0 \end{bmatrix}\begin{bmatrix} e^{i(\Omega-\omega)\tau/2} & 0 \\ 0 & e^{-i(\Omega-\omega)\tau/2} \end{bmatrix}$$

$$= \frac{\sqrt{2}\gamma\hbar B_0}{2kT}\begin{bmatrix} 0 & 1 \\ -1 & 0 \end{bmatrix} \qquad \text{Eqn 1.65}$$

$$= -\frac{\sqrt{2}\gamma\hbar B_0}{2kT}\sigma_y$$

Hence the effect of the π is to refocus the magnetization back to the state immediately after the $\pi/2$ pulse, i.e., along the y axis. This has the same result as the classical method. The density matrix method will work for spins >1/2 by simply replacing the density matrix.

Chapter 2

Magnetic Resonance Imaging

Among the various imaging methods, the dominant imaging technique is the 2-D Fourier transform method. The method was first proposed by Kumar [*3*] and later revised by Edelstein [*4*]. The quality of MR images depends on the choice of scan parameters. Changing these scan parameters can emphasize increasing an image's spatial resolution in exchange for lower S/N. Changing the parameters can enhance contrast in a particular tissue with certain relaxation times in exchange for contrast decrease in other tissues with different relaxation times. As with any nuclear magnetic resonance experiments, the signal to noise ratio is low because signal provided by the precessing nuclei is small, but with meticulous execution, images with high diagnostic qualities are readily obtained. This section will describe the implementation of the imaging method used in this experiment. A major advantage of using MRI is the in-vivo capability of this method. Tissue characteristics will change upon excision. In vitro experiments also lack the physiological correlations that living tissue have, such as blood perfusion, temperature regulation, and oxygenation.

Slice Selection

Slice selection is done with an application of a linear gradient along the axis of the magnet (z-axis). The result of this gradient is that the Larmor frequency will be a function of position along the z-axis expressed by the relationship,

$$\begin{aligned}\omega(z) &= \gamma B(z) \\ &= \gamma(B_0 + \Delta B) \\ &= \gamma(B_0 + G_z z)\end{aligned} \qquad \text{Eqn 2.1}$$

This provides a one to one correspondence of space to frequency along the z direction. To excite a slice, Δz, at a position z_l, the RF pulse must have narrow frequencies content of $\Delta\omega$, centered at ω_l. To accomplish this, the RF pulse has a sinc shape in the time domain to produce a square profile in the frequency domain. Practical implementation of the sinc pulse is a truncated pulse for the obvious reason that the pulse has a finite duration. Typically only the central five zero crossings are kept. The profile in the frequency domain is not square but has tapering edges and has ripples due to the truncation of the sinc selective pulse. Nuclei along these points will not experience a correct pulse as those points within the central area experience a partial flip. This causes a correctable error in T2 measurements.

Two dimensional Fourier Transformation Acquisition

A two dimensional Fourier transform (2DFT) is the prevalent method of image acquisition. The pulse sequence of the 2D acquisition used in this experiment is shown in figure 2.2. The RF sequence is a basic $\pi/2$-τ-π-2τ-π-delay two echo sequence. The spatial encoding is done with the x and y gradients where the x gradient is the read out gradient and y gradient is the phase encoding gradient.

At t_1 a selection gradient (z-gradient) is applied along the z axis along with a $\pi/2_x$ sinc pulse for a duration T_s. This will produce a rotation of the slice's magnetization about the x axis. The selection gradient should be turned off after T_s, but because magnetization dephases during the slice selection pulse, the selection gradient must be reversed by an application of a reversal gradient. The rephasing time and areas for each dephasing component are represented in figure 2.2 by the similar cross hatching. The area of the reversal slice gradient is equal to 1/2 the area of the slice selection gradient. The frequency encoding is achieved by an application of an x gradient at time A, but to guarantee that the signal will be in phase at t=TE, a dephasing x gradient is applied at the same time as the slice rephasing. The application of a x gradient during data acquisition will modify the precession frequency along the x axis by

$$\omega(x) = \gamma(B_0 + G_x \cdot x) \qquad \text{Eqn 2.2}$$

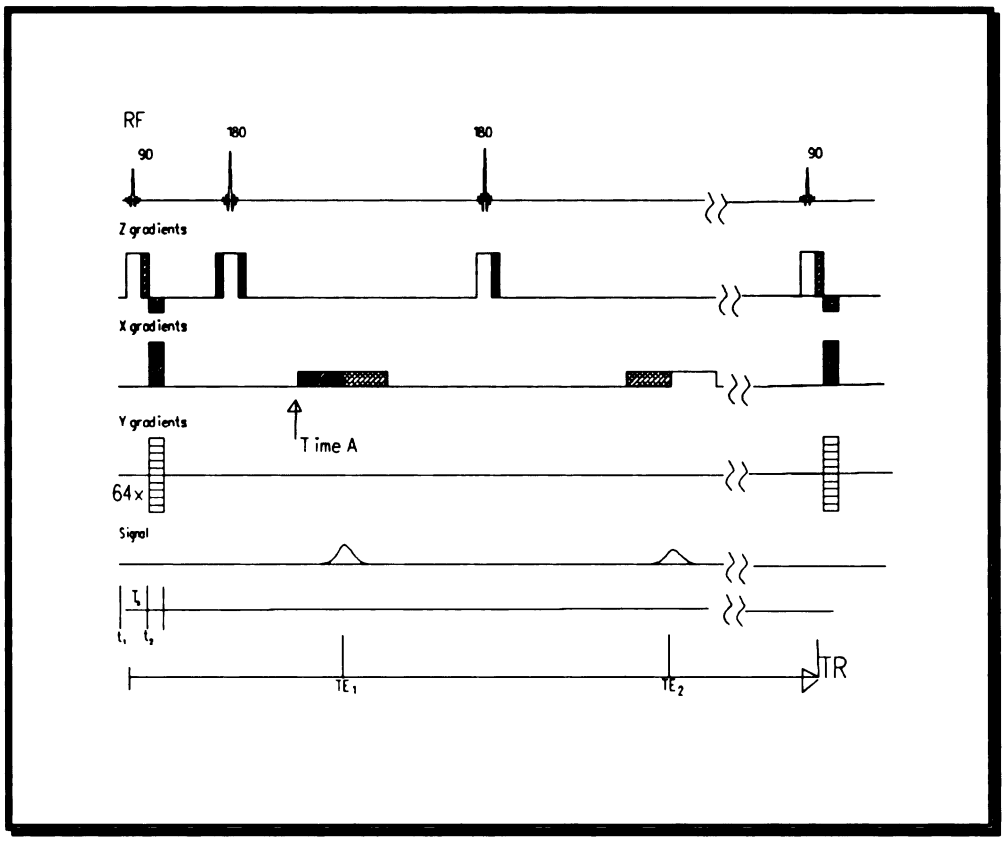

Figure 2.2
Imaging sequence use in this experiment. It is a two echo sequence. The rephasing gradients are represented by the corresponding cross hatching and typically have equal pulse area. Two identical sequences except for the repetition are required to calculate T1.

A one-dimensional FT of the signal produces a projection of all items in the y-axis along the x-axis (this is the method used in projection reconstruction). Reconstruction for a 1DFT is straight forward application of a FT,

$$m(x) = K\int_{-\infty}^{\infty} S(t)e^{(-2\pi i\gamma G_x xt)}dt \qquad \text{Eqn 2.3}$$

where $S(t)$ is the acquired signal. This will give projections of the y-axis spin densities onto the x-axis. A detail discussion of the 1DFT will help conceptually in the 2DFT case. The analog data

obtained in a MR acquisition is digitized. Sampling is done at equal intervals. Define the wave number k_i, as

$$k_{x_i} = -\gamma G_x t_i \qquad i = -N....0,1,2....N-1 \qquad \text{Eqn 2.4}$$

where t_i is the sampling interval and rewriting eqn 2.3, we get

$$m(x_i) = K \sum_{i=-N}^{N-1} S(k_i) e^{(2\pi i k_i x_i)} \qquad \text{Eqn 2.5}$$

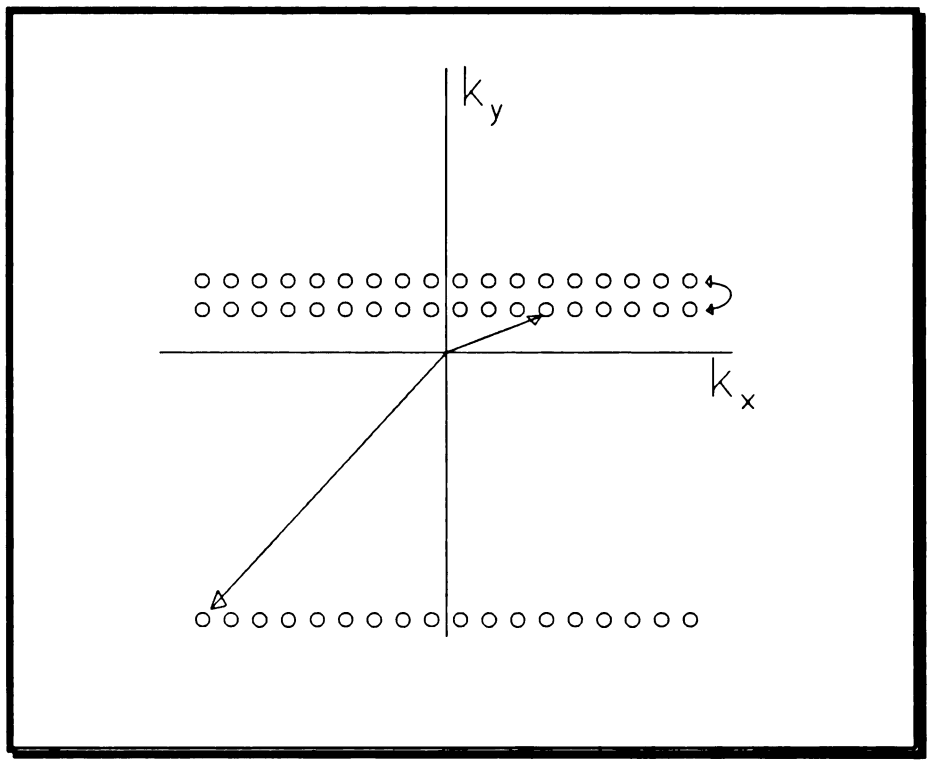

Figure 2.3

Sampling in k space. Signal is recorded at equidistant space intervals beginning at the k_y=-64 and k_x=-64. The scans with k_x increasing until k_x=63. After the next TR, ky is incremented by 1 to -63. This is repeated for until k_y=63. The description given here is not unique because any particular order will give the same sampling in k space. The order is usually done to satisfy the hardware requirements.

This gives us an equal sampling in k space along the k_x axis at $k_y = 0$, as shown in figure 2.3. The next obvious step for a 2DFT is to sample the $k_y = -N, -N+1, .., 0, .. N-1$ projections. This is accomplished by the phase encoding gradient, G_y. If the phase encoding is applied with a constant amplitude G_y and for a duration τ, we get

$$k_{y_i} = -\gamma G_{yi} \tau \qquad i = -N \ldots . 0, 1, 2, \ldots . N-1 \qquad \text{Eqn 2.6}$$

which is analogous to eqn. 2.4 If $k_{x_i} = k_{y_i}$ and $N_x = N_y$, the image has square voxels. In an analogous fashion, the 2DFT is

$$m(x,y) = K\sum_{i=-N}^{N-1}\sum_{j=-N}^{N-1} S(k_{x_i}, k_{y_j}) e^{2\pi i\left(k_{x_i}x_i + k_{y_j}y_j\right)} \qquad \text{Eqn 2.7}$$

It is possible to produce the spatial image from the k space image. Actual one dimensional implementation in the computer system is a fast Fourier transform (FFT). The algorithm for a 1 dimensional FFT reduces the number of calculations required to perform a domain transform from N^2 operations for a brute force implementation of equation 2.7 to $N\log(N)$ operations.

Resolution

MR images are spatial images mapped from frequency images. Spatial resolution is determined by the MR image's frequency resolution. The sample window is always within the length of the x readout gradient on time. The sampling window, the number of data points, gradient strength, and their relations to each other determine the resolution in the read out direction. The perpendicular direction's resolution is determined by the phase encoding steps. The phase encoding resolution has the same relationship as the read direction except it is done in discrete steps. The frequency separation between two adjacent voxel is determined by the gradient,

$$\Delta f = \gamma G \Delta x \qquad \text{Eqn 2.8}$$

The line width of the voxel must be taken into consideration because the line width is the upper limit on the resolving power of an MR image. The line width of the resolved line is given by

$$\Delta f_{lw} = \frac{1}{\pi T_2^*} \qquad \text{Eqn 2.9}$$

and the condition of $\Delta f \leq \Delta f_{lw}$ limits the minimum gradient to be

$$G \geq \frac{\Delta f_{lw}}{\gamma \Delta x} \qquad \text{Eqn 2.10}$$

T_2^* used above must exclude any effects of a linear gradient in the intended readout direction and is descriptive only of the resolved line and not of the entire plane. The resolution given by eqn. 2.8 would imply that as the gradient is increased indefinitely, the spatial resolution will increase

accordingly. The resolution has limitations imposed by the limited S/N of the image and by diffusion. Sampling and bandwidth also effects the resolution. Sampling of the FID determines the maximum resolution we can resolve even with a very narrow natural line width. If we want a resolution of $\Delta\nu$, we have to sample for at least $T_{sample} = 1/\Delta\nu$ seconds.

The echo is acquired during a sampling window. The sampling window also determines the image resolution and is given by

$$\text{resolution} = \frac{1}{\text{sampling window}} \quad [\text{Hertz / pixel}] \qquad \text{Eqn 2.11}$$

The sampling rate determines the field of view (FOV). The FOV is simply the product of the number of points and the resolution,

$$\text{FOV} = (\text{Number of Points})(\Delta x) \quad [\text{cm}] \qquad \text{Eqn 2.12}$$

The maximum frequency that can be sampled without aliasing is given by the Nyquist frequency, which is 1/2 the sampling rate

$$\text{Nyquist Frequency} = \frac{1}{2}\text{sampling rate} \quad [\text{Hz}] \qquad \text{Eqn 2.13}$$

Application of a 48 db/oct (Butterworth filter, Rockland model 452) removes the out of band noise, thus preventing a loss in S/N due to aliasing. Aliasing is more troublesome if the imaged object is larger than the FOV because if the signal of the object is high, the aliased signal from the portion of the object outside the FOV will fold back into the image. This is limited in the read out direction with the application of an external filter but the phase encoding direction does not have the luxury of an external filter. Alias reduction in the phase encode direction is accomplished by ensuring that the FOV is larger than the signal producing object along the phase encoding direction.

The sampling window has limits on its duration. The boundaries are the π pulse and the end of the sequence at $t = TR$ or the next π pulse in a multi-echo sequence. For symmetric sampling the maximum sampling window is TE, beginning after the π pulse at TE/2 and sampling until $t = 3TE/2$ gives equal times on either side of the echo peak. The sampling window is increased substantially if sampling is done asymmetrically. The sampling begins after the π pulse (usually

approximately $TE/2$ before the peak of the echo) to well past $t = TE/2$ after the peak of the echo. In theory, the sampling can be done right up the $t = TR$, but in practice, the sampling is done until the echo does not have substantial signal. The truncated portion of the echo is supplied by the property of the data being Hermitian and is call *conjugation* [5]. Increasing the length of sampling for a fixed number of points will increase the S/N by $\sqrt{\text{Time per point}}$. The advantage of asymmetric sampling is the typical reduction of noise by ~40% than with symmetric sampling.

Signal averaging improves the S/N by $\sqrt{n}$, where n is the number of averages. The image size is 64x64 pixels with TR=0.9 secs, giving a total imaging time of 57.6 secs. A second image with a TR=0.15 secs. is require to compute T1 with an imaging time of 9.6 secs. giving a total time of 67.2 seconds. This experimental setup does not have a real time intravenous injection of anesthetics so the imaging time is restricted to the effect time of the anesthetics which is about 1.5 hours. The 1.5 hours provide about 80 images and keeping the number of averages a power of 2 will allow 64 images for averaging. Averaging 64 images increases the S/N by 8.

Contrast

Image contrast between lesion and background is a required characteristic for a useful diagnostic image. MRI has more contrast variables than a radiograph. Radiographs are images of electron densities and the contrast in these images reflect this dependency. MRIs have the two intrinsic relaxation times and hydrogen density that produce contrast. The sequences used to acquired these images also have variables that will change the images contrast. For example, spin echo sequences will behave differently than inversion recovery sequences when the repetition times are change. Taking a single spin echo as an example, the signal is given as,

$$S = M_0\left(1 + e^{-TR/T1} - 2e^{-(TR-TE/2)/T1}\right)e^{-TE/T2} \qquad \text{Eqn 2.14}$$

where TR is the repetition time, and TE is the echo time. The contrast is the difference between lesion and background intensities divided by the background intensities (i.e. $\text{Contrast} = (S_2 - S_1)/S_1$). Equation 2.14 shows that contrast will depend proportionally on the hydrogen densities, but the dependencies on the relaxation times are exponential. Two additional sequence parameters affect the contrast, TR and TE. These also affect the contrast in an exponential fashion [6]. Figure 2.4 is an example of how changes to a sequence parameter affect

the contrast. The plot is the change in contrast due to change to TE. Plots similar to this one showing how the contrast depends on other sequence parameters can be implemented easily.

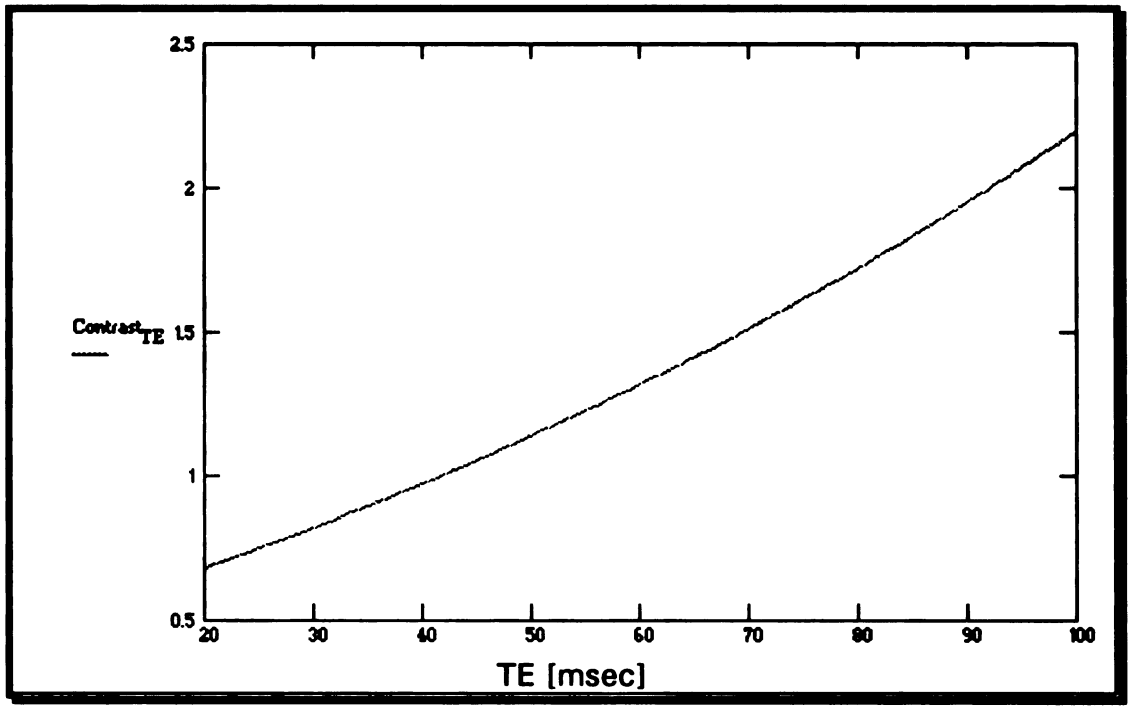

Figure 2.4
Plot of contrast of adjacent tissues as the echo time (TE) is changed. The values used for background were T_1=150ms and T_2=50ms and M_o=1. The values used for lesion were T_1=350ms and T_2=85ms and M_o=1.5. Contrast here is defined as $(S_2-S_1)/S_1$.

Dispersion affects the contrast as shown in equation 2.14. A sequence can be optimized to the display T_1 differences, or T_2 differences, or a combination of both. Dispersion data provide information for pulse programmer or a radiologist to choose a sequence that will optimize the contrast of the lesion in question. Dispersion data [*22*] have shown that large changes in relaxation times occur in the low field regime, changing by over a factor of 5. High field dispersion is very small, where relaxation differences between different tissue are rarely greater than a factor 2.

Signal Intensity for a Spin Echo Sequence

The signal received from the precessing nuclei depends on, among many other parameters, the relaxation times and pulse sequences. The pulse sequence used in the experiment is a "$\pi/2 - \tau - \pi -$

τ - acquire " sequence. An imaging sequence repetition rate (T_R) is rarely the 4-5 T_1 required for the magnetization to relax to its equilibrium, rather a steady state value is reached. The steady state value is achieved by the second application of the pulse sequence as will be shown. The intensity can be calculated with the application of Bloch equations, eqn. 2.22 and 2.23. The basic form of the magnetization recovery equation is

$$M_Z(t) = M_z(0)e^{-t/T_1} + M_z(\infty)\left(1 - e^{-t/T_1}\right) \qquad \text{Eqn 2.15}$$

where

$M_z(0)$ = Magnetization at $t = 0$

$M_z(\infty)$ = Magnetization as $t \to \infty$

Immediately after the application of a π/2 pulse, the transverse and longitudinal magnetization are

$$M_l(t) = M_0\left(1 - e^{-t/T_1}\right)$$
$$M_t(t) = M_0 e^{-t/T_2} \qquad \text{Eqn 2.16}$$

waiting a delay TE/2, and before an application of the π pulse,

$$M_l(TE/2) = M_0\left(1 - e^{-TE/2T_1}\right)$$
$$M_t(TE/2) = M_0 e^{-TE/2T_2} \qquad \text{Eqn 2.17}$$

and after the application of the π pulse,

$$M_l(t) = -M_0\left(1 - 2e^{-(t-TE/2)/T_1} + e^{-t/T_1}\right)$$
$$M_t(t) = -M_0 e^{-t/T_2} \qquad \text{Eqn 2.18}$$

The echo will occur at t = TE, which is another delay of TE/2, is the time when the data is acquired,

$$M_l(TE) = M_0\left(1 - 2e^{-TE/2T_1} + e^{-TE/T_1}\right)$$
$$M_t(TE) = -M_0 e^{-TE/T_2} \qquad \text{Eqn 2.19}$$

delaying until the next pulse, which is at t=TR,

$$M_l(TR) = M_0\left(1 - 2e^{-(TR-TE/2)/T_1} + e^{-TR/T_1}\right)$$
$$M_t(TR) = -M_0 e^{-TR/T_2} \qquad \text{Eqn 2.20}$$

The sequence used in this experiment is a dual spin echo sequence. The second π pulse is applied after a delay time of TE_2 after the peak of the first echo (the first occurred at $t = TE$). Our sequence has $TE_1 \neq TE_2$. The magnetization is then given as,

$$M_l(t) = M_0\left[1 + \left(2e^{-(TE_1 - TE_2/2)T_1} + e^{-TE_2/2T_1} - 1\right)e^{-t/T_1}\right] \qquad \text{Eqn 2.21}$$

Hardware

A schematic of a magnetic resonance imager is shown in figure 2.1

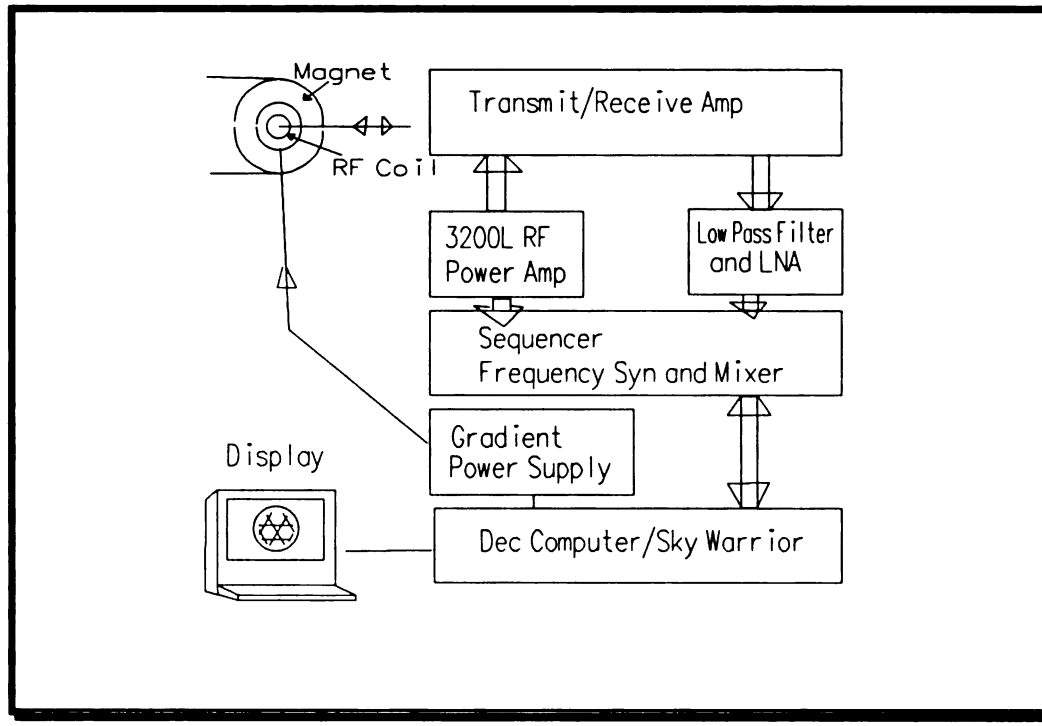

Figure 2.1
Schematic of the rat imaging system. This system consist of a Diasonics imaging system attached to an Oxford magnet.

The magnet

The magnet used in this experiment is a supeconducting magnet custom built by American Magnetics. The field is adjustable with a maximum of 5 Tesla. The clear bore size is 150mm, and adding shims, gradient coils, and RF coil will reduce the usable bore to 90mm. The magnet has, typical of superconducting magnets, excellent field stability (0.05 ppm/hr). The magnet has a nitrogen jacket surrounding the helium jacket. The helium tank holds about 60 liters of liquid helium and requires a refill about every 30 days. The nitrogen jacket needs to be refilled every 5 days.

Gradient Coil

The same gradient coil was used at all fields except at 340 gauss. The gradient coil used at 340 gauss has four turns of stranded wire (Lietz wire). The Lietz wires contributes to the interaction between the gradient coil and the RF coil which gave a substantial increase in coupled noise. The noise was largest at 650 Gauss. To minimize this, another gradient coil was constructed containing only a single turn of solid wire. This helped alleviate most of the coupling at 650 gauss. The axial (z) gradient is a pair of opposing Maxwell coils. The transverse (x and y) gradient are a pair of Golay coils. The restriction of the minimum number of turns we can safely use is determined by the compliance of our Crown 7570 gradient amplifiers.

RF Coil

A radio frequency (RF) resonator (or coil) is needed for excitation of the nuclei and reception of the signal from the precessing nuclei. A single RF coil can be used for transmission and reception or separate RF coils can be used. We used the single RF coil approach. Using the single coil has its advantages and disadvantages. The equation for the signal to noise ratio for a coil is given by [7]

$$\psi = K\eta M_0 \left(\frac{\mu_0 Q \omega_0 V_c}{4FkT_c \Delta f} \right)^{1/2} \qquad \text{Eqn 2.1}$$

where

K = numerical factor
η = filling factor
M_0 = static magnetization
μ_0 = permeability of free space
Q = quality factor
ω_0 = Larmor frequency
V_c = coil volume
F = noise figure of the receiver
k = Boltzmann's constant
T_c = coil temperature
Δf = receiver bandwidth

The factors that are in our control during the coil construction are the filling factor, η, the coil volume, V, and to some degree the quality factor, Q. The schematic of the series-parallel RF coil tuning and coupling chosen for this experiment is shown in figure 2.2

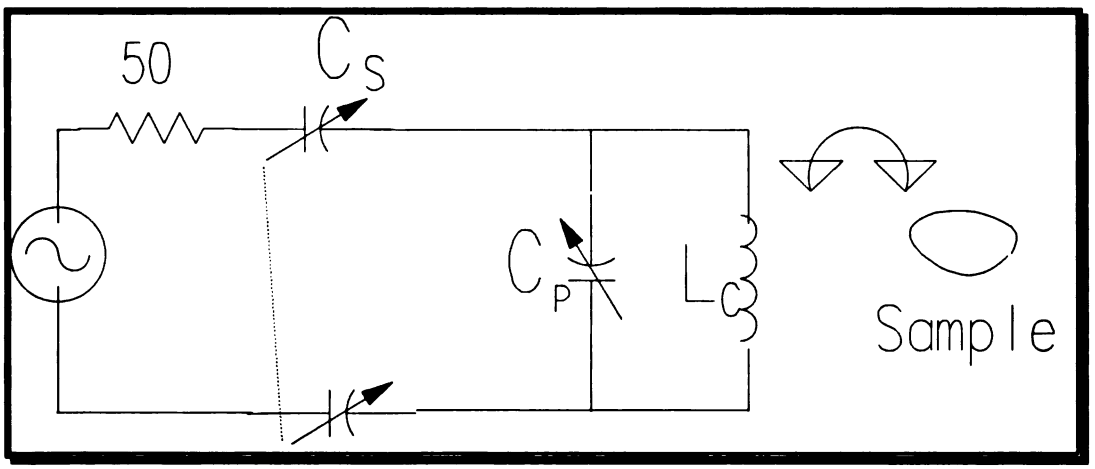

Figure 2.2
Schematic of RF coil. The inductor is the coil itself coupling to the sample. C_p is the parallel capacitance to tune the circuit to resonance. C_S is the series capacitance to match the circuit to the input impedance of 50Ω.

The coil is both a transmit and receive coil. The coil is connected to the RF transmitter and receiver through a T/R switch. The T/R switch functions during transmission with the pin diode,

D1, connected between the transmitter and coil becoming a short. This provides a direct path for the transmit pulse to the coil. The receiver is isolated from the high power transmit pulse by the tank circuit L1 and C1. Diodes D2 and D3 are shorts during the transmit pulse. Diode D3 being a short effectively grounds the receiver connection. The tank circuit is in a parallel configuration connection so it will be a high impedance at resonance. During receive, diode D1 is an open circuit effectively eliminating the power amp from the circuit. Diodes D2 and D3 are also effectively open circuits, so the coil is connected to the receiver in series with the tank circuit consisting of L1 and C2. This tank circuit is in an serial connection so it will have a very low impedance at resonance thus providing a connection between the coil and the receiver.

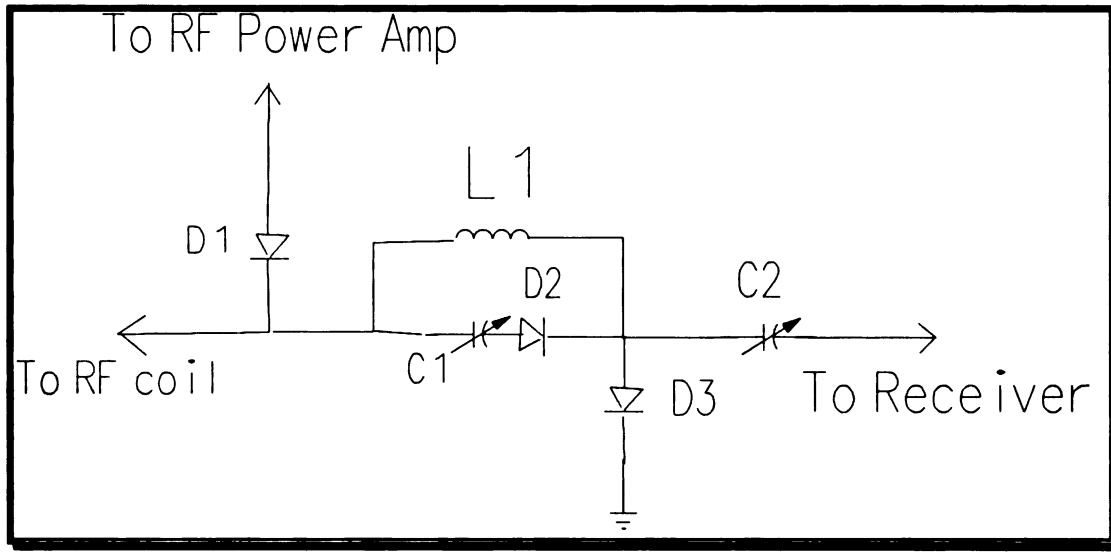

Figure 2.3
Schematic of T/R switch

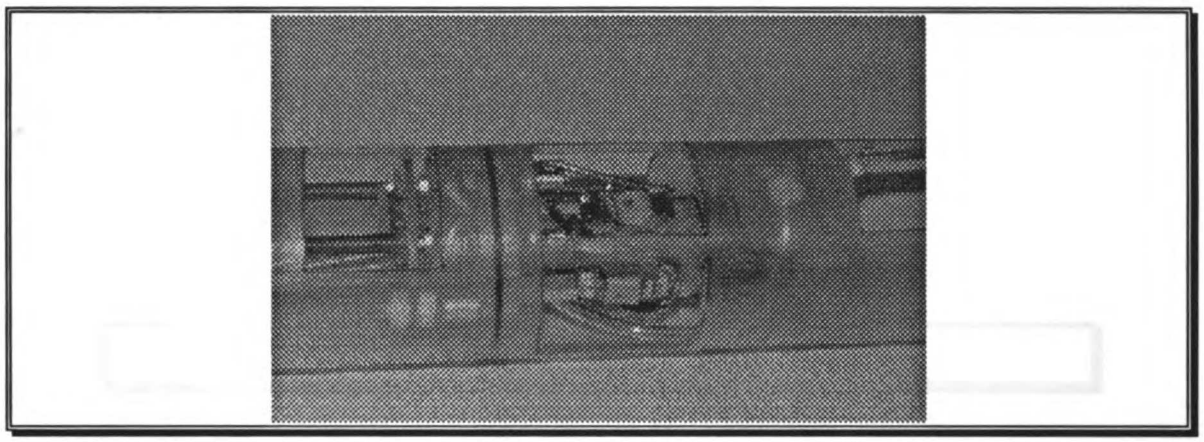

Figure 2.4
Rat head RF coil. The coil is a saddle type with 4 turns and has 1.5 inch diameter bore.

Because the S/N is proportional to the filling factor, two radio frequency (RF) coils were built to maximize the filling factor of the coil. The volume of a rat's head and hip differ about 3:1. Using a body coil for head scanning will lower the signal to noise by a factor of three thereby justifying the construction of two coils of different volumes. The smaller coil has a diameter of 1.5 inches to accommodate the head of a rat and the larger coil has diameter of 3 inches to accommodate the body of the rat. Figure 2.4 is a picture of the head RF coil. Both coils have all tuning capacitors attached to the coils. The tuning capacitors were 0-120 pF type from Voltronics, and are constructed from brass and quartz. The same tuning capacitors were used for all fields with only the fixed capacitors changed with the field.

The length to diameter ratios were 1.5:1, not 2:1 (as suggested by Hoult [7]) to maximize homogeneity) because the small diameter allows only the head of the rat but not the shoulder thereby limiting the length of the coil to the length of the rat's head. The wire used was a solid core 10 AWG copper wrapped on a Plexiglas form. The space between wires was the thickness of the wire for minimization of "proximity effects" [7]. The 10 awg wires were chosen to fulfill the requirement of low resistance and still be able to form nicely on the Plexiglas tube.

Table 2.1 Head Coil

Coil diameter	1.5 in
Usable diameter	1.25 in
Inductance	2.15 μH
Q @ 3.4 MHz	364

Table 2.2 Body Coil

Coil diameter	3.0 in
Usable diameter	2.75 in
Inductance	4.76 μH
Q @ 3.4 MHz	265

The coupling of the RF coil to the sample determines the power needed to produce the necessary tipping pulse. A coil of inductance L_0 is filled with a material with susceptibility χ_0 will have its inductance changed by

$$L = L_0[1 + 4\pi\chi(\omega)] \qquad \text{Eqn 2.2}$$

which give the average power as,

$$\langle P \rangle = \tfrac{1}{2}\omega H_1^2 \chi'' V \qquad \text{Eqn 2.3}$$

where H_1 is the amplitude to the RF pulse, χ'' is the imaginary part of the susceptibility, and V is the volume of the uniform field. Another form of equation 2.3 is typically used because of its convenience. A more useful form of equation 2.3 is the mixed units form,

$$H_1 = \sqrt{\frac{10PQ}{\nu V}} \qquad \text{Eqn 2.4}$$

where H_1 has units of [Gauss], P has units of [Watts], ν has units of [MHz], and V has units of [cm^3].

Measuring Relaxation Times

Measuring relaxation times from images are more restrictive than measuring them from spectroscopic data because of acquisition time and S/N constraints. In spectroscopy, many points are acquired during a single relaxation and T_1 and T_2 are calculated using various error minimizing algorithms. The time to obtain the data is dependent on T_1 and the signal to noise ratio required. Typically, spectroscopy measures only homogeneous in-vitro samples so data acquisition time is limited by the experimenter's patience (acquisition times can be many hours) and by the relaxation time. The relaxation time measured is an ensemble average of the sample. In-vivo measurements do not have the luxury of unlimited scan times. Anesthesia has a limit in duration of effectiveness. In our case, this is 1½ hours. This time constraint will determine the number of acquisitions, resolution, and signal to noise ratio. A spin echo technique is generally used for T_2 measurement because the π pulse in the spin echo sequence reverses any reversible process that occurs during the relaxation.

Measuring T_1

The data acquired are from a pair of images, each with two echoes. Calculations of T_1, T_2 are two point calculations and assume a single exponential for both T_1 and T_2. Sensitivity uncertainties are present in this type of measurements and the general approach is to choose the sequences to minimize the errors. The signal intensity of a spin echo sequence is given by 1.21 and keeping TE fixed and varying TR will allow the calculation T_1 by taking the ratio of the two images,

$$\frac{S_2}{S_1} = \frac{1+\left(2e^{-(TE_1-TE_2/2)T_1} + e^{-TE_2/2T_1} - 1\right)e^{-TR_2/T_1}}{1+\left(2e^{-(TE_1-TE_2/2)T_1} + e^{-TE_2/2T_1} - 1\right)e^{-TR_1/T_1}} \qquad \text{Eqn 2.5}$$

and solving T_1 numerically. The method of using a lookup table for T_1 for a given ratio is one of the most efficient methods and is used in this experiment. An extrapolation is done on the entries of the lookup table for ratios not listed in the table.

Analysis of the error produced by a two point measurement is simplified by keeping the ratios, R, of the longer vs the shorter TR's an integer. Typical of imaging sequences, the echo time is considerably shorter than the repetition time, i.e., $TE << TR$. The ratio simplifies when TR_2 is chosen to be an integer multiple of TR_1 and making the assumption that $TE<<TR$. The first is within our experimental control and TR_2/T_{11} was chosen as 6. The ratio was not arbitrary but was chosen with regards to minimizing the error in T_1 measurement. The second assumption is not be applicable for tissue with short T_1 but, for this experiment, where the typical T_1 is 300ms and the TE is 30ms gives,

$$\begin{aligned} 1-e^{-TE/2T_1}e^{-T_R/T_1} &= 1-e^{-30/2\cdot 300}e^{-T_R/T_1} \\ &= 1-.951e^{-T_R/T_1} \end{aligned} \qquad \text{Eqn 2.6}$$

Thus introducing the approximating will give a 5% error.

Defining the uncorrelated noise as δS_1 and δS_2, the uncertainty for a two point T_1 measurement is

$$(\delta T_1)^2 = \left(\frac{\delta T_1}{\delta S_1}\right)^2 (\delta S_1)^2 + (\delta S_2)^2 \left(\frac{\delta T_1}{\delta S_2}\right)^2 \qquad \text{Eqn 2.7}$$

Evaluation of the terms are straight forward. T_1 is calculated from the ratio $R= S_2/S_1$ so,

$$\frac{dR}{dS_1} = -\frac{S_2}{S_1} \quad \text{and} \quad \frac{dR}{dS_2} = \frac{1}{S_1} \qquad \text{Eqn 2.8}$$

and by the chain rule,

$$\frac{dT_1}{dS_{1,2}} = \frac{dT_1}{dR}\frac{dR}{dS_{1,2}} \qquad \text{Eqn 2.9}$$

and

$$\frac{dR}{dT_1} = \frac{dR}{dS_1}\frac{dS_1}{dT_1} + \frac{dR}{dS_2}\frac{dS_2}{dT_1}$$
$$= -\frac{S_2}{S_1^2}S_1' + \frac{1}{S_1}S_2' \qquad \text{Eqn 2.10}$$
$$= \frac{S_1S_2' - S_2S_1'}{S_1'^2}$$

Replacing the terms in equation 2.7 gives the T_1 error with the assumption that $S_2 > S_1$ and $TR_2 > TR_1$ as,

$$\frac{\delta T_1}{T_1} = \delta S \frac{S_1\sqrt{1+\left(\frac{S_2}{S_1}\right)^2}}{\left(S_1S_2' - S_2S_1\right)T_1} \qquad \text{Eqn 2.11}$$

where

δS the noise of S_1 and S_2

$$S_{1,2}' = \frac{\delta S_1}{\delta T_1}$$

Chen has calculated numerically the error propagation for a two point measurement [8]. His analysis for the values of the repetition time and the ratio of the repetition times are given in the table below. This table is calculated with imaging time as a constraint and with a TE value of 30ms.

Table 2.3
Table of optimum TR for a given T1

T_1	TR_1	TR_2/TR_1
2000	$.7T_1$	5.4
400	$.8T_1$	5.2
200	$.9T_1$	5.0
100	$1.0T_1$	4.5
60	$1.16T_1$	4.0

For the tissue measured in this experiment, which are ~200ms range, the proper choice has $TR_1 \sim .9T_1$ and the ratio of about 5. At the optimum TR, the effective $\Delta T_1 / T_1 \sim 2\%$ [8].

Measurements of relaxation times from images can introduce errors inherent in the imaging process. T_1 calibration as done to determine the errors produced by the imaging process. Figure 2.5 shows a typical T_1 calibration graph where the slope gives the slice selection effects.

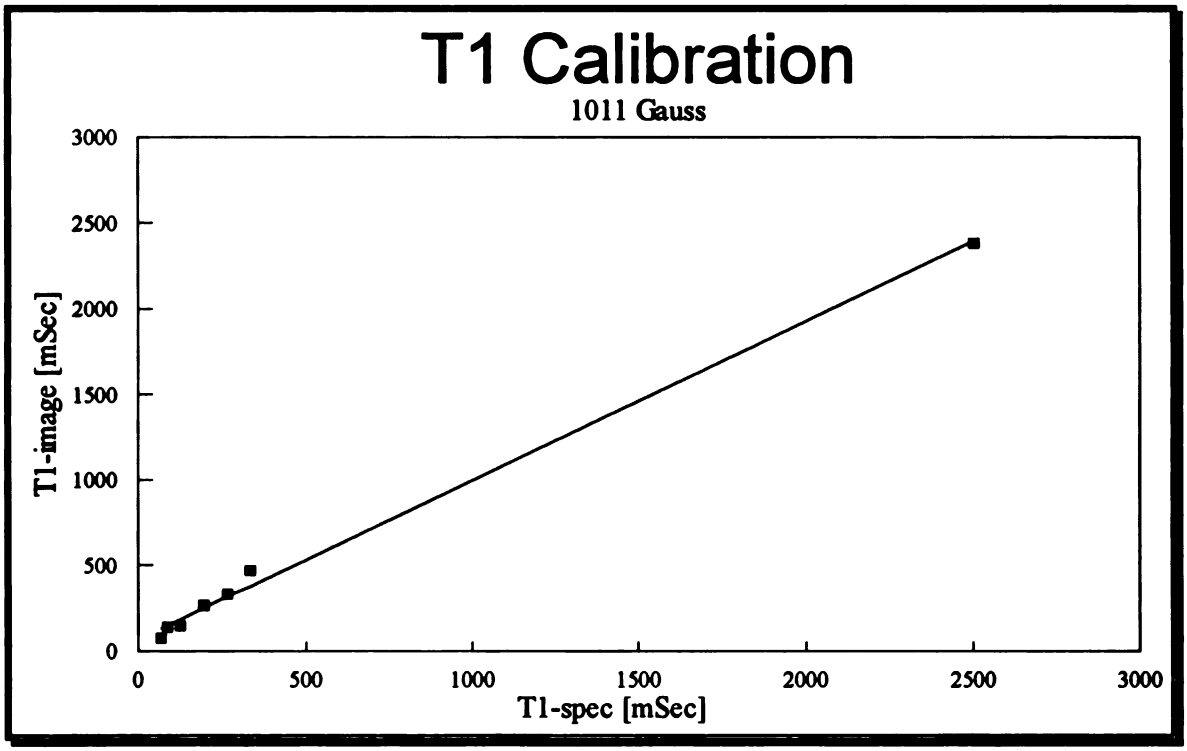

Figure 2.5

Correlation for T_1 between imaging and spectroscopy. Samples of different concentrations of manganese doped water are imaged and T1 calculated from these images. The sample's T1 were also measured spectroscopically. The slope of the line gives the relative error due to the slice selection process.

Measuring T_2

T_2 is calculated with a single TR but acquiring two echoes. The images used to calculate T_2 are the one with the larger S/N. These are the images with the longer TR. Taking the ratios of the image intensities gives,

$$\frac{I_1}{I_2} = \frac{e^{-TE_1/T_2}}{e^{-TE_2/T_2}} \qquad \text{Eqn 2.12}$$

which immediately gives T_2 as

$$T_2 = \frac{TE_2 - TE_1}{\ln\left(\frac{I_1}{I_2}\right)} \qquad \text{Eqn 2.13}$$

Though the solution of T_2 looks rather straight forward, there is an unsuspecting error due to the slice selection process in this calculation [9]. To see this, consider the n^{th} echo of a multi echo sequence with selective excitation producing an intensity

$$I_n = e^{2n\tau/T_2}\left|\int_{lz} M_0 P_n(z)dz\right| \qquad \text{Eqn 2.14}$$

where

$$\int_{lz} P_n(z) = \int_{lz} P_1^{\pi/2}(z) P_n^{\pi}(z)dz \qquad \text{Eqn 2.15}$$

is the normalized complex slice profile function, l_z, is the extent of the slice, and 2τ is the echo to echo time. $P_1^{\pi/2}(z)$ is the profile of the initial $\pi/2$ selective pulse and can be measured by applying a $\pi/2$ selective pulse followed by a hard unselective π pulse and read out with the slice selection gradient. $P_n^{\pi}(z)$ is the n^{th} π selective pulse profile and can be measured . Assuming that M_0 is constant over the thickness of the slice, which allows M_0 to be taken out of the integral, and replacing eqn. 2.14 into eqn. 2.13

$$T_2 = \frac{-2\tau}{\ln\left(e^{4\tau/T_2}/e^{2\tau/T_2}\right) + \ln\left(\left|\frac{\int P_2(z)dz}{\int P_1(z)dz}\right|\right)}$$ Eqn 2.16

rearranging gives

$$\frac{1}{T_2} = \frac{1}{T_2'} - \frac{1}{2\tau}\ln\left(\left|\frac{\int P_2(z)dz}{\int P_1(z)dz}\right|\right)$$ Eqn 2.17

The transverse relaxation rate is modified by the slice profile error term. The error shortens T_2, and with T_2 large, the error can be the dominate term shortening the T_2 considerably. Correction to the measured relaxation times is done by calibrating with phantoms with known relaxation times. Scans with the slice selection and without slice selection using the same phantoms allow the determination of the error term.

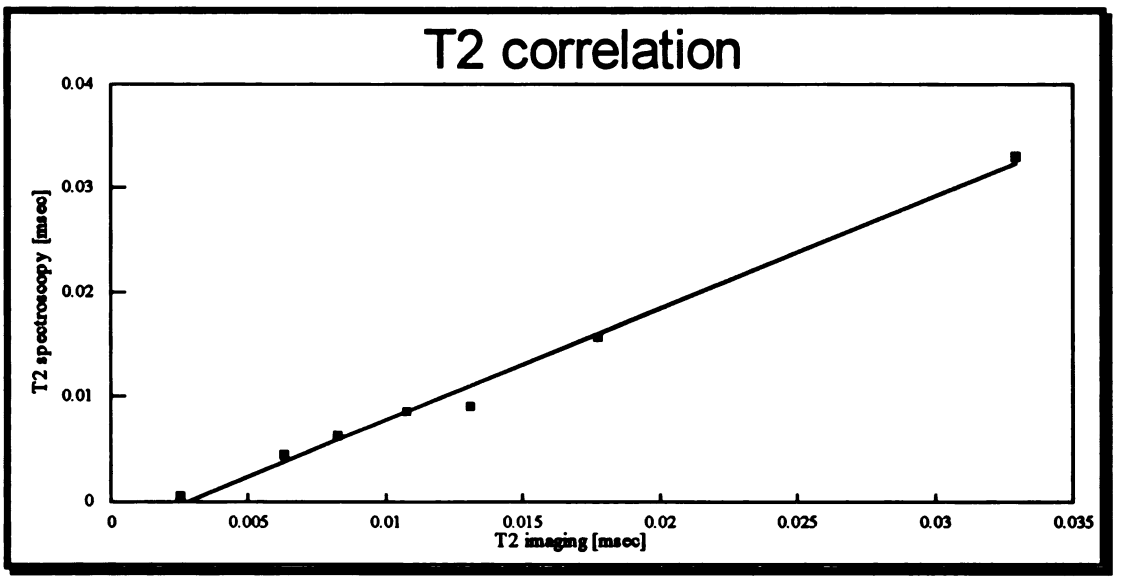

Figure 2.6
Correlation for T_2 images. Samples of different concentration of manganese doped water are imaged and T2 calculated from these images. The sample's T_2 were also measured spectroscopically. The slope of the line gives the relative error due to the slice selection process as discussed in the text.

The error propagation of T_2 is considerably easier to obtain than of T_1. Defining δR as eqn. 2.14 and following the same procedure as for T_1, we get

$$\frac{\Delta T_2}{T_2} = \frac{1}{S_1/N} \frac{\sqrt{1-e^{2TE/T_2}}}{TE/T_2} \qquad \text{Eqn 2.18}$$

Again taking the results from Chen [8], the T_2 error has a minimum at $TE = 1.1T_2$. The minimum is fairly broad, ranging from roughly $.5T_2$ to $2.2T_2$ so the an exact TE is not critical for minimizing the T_2 error.

Chapter 3

Relaxation

A theory of relaxation was presented in the seminal paper by Bloembergen, Purcell, and Pound [*10*] and expanded by Solomon [*11*]. A large amount of work has been done since and summarized in two textbooks [*12,13*] and the amount is still increasing in current literature but the basic BPP theory is still invoked in tissue relaxation. The BPP theory shows that relaxation is related to nuclear motion. This presentation will deal mostly with proton relaxation, since the images are proton images except where a quadrupolar nucleus interacts with the protons. The results we are after are those applicable to tissue. Models of tissue relaxation use the concept of the multiple phases of water with the proton sharing time in each phase. Each phase has different relaxation times depending on the physical characteristics. Most models can be generalized to contain variations of three distinct phases, solid-like, hydration, and free water. The solid and free phases will be discussed in the following sections and the hydration layer phase will be discussed in the tissue relaxation section.

Magnetic relaxation has many ideas common with electric relaxation. Electric relaxation theory was worked out extensively during the early 1900's. Results from this prior work, such as those from Debye, are frequently reformulated and applied to magnetic relaxation. The concern here is with the dynamic properties of the magnetic susceptibility rather than the static case because the dynamics of the magnetic moment dictate the frequency dependencies of the relaxation time, paralleling to that of the dielectric constant frequency dependencies.

Relaxation is the process of returning to equilibrium from a perturbed state. Spontaneous emissions of an excited state at MRI frequencies are extremely small, on the order of 10^{-25} sec^{-1},

which cannot be the primary mechanism for the relaxation times observed. The primary mechanism of relaxation in liquids is stimulated emission caused by molecular Brownian motion, occurring when the frequency of the instigating field is the same as the transition frequency. A correlation time, τ_c, is a parameter used to describe this type of Brownian motion.

Spin lattice relaxation requires transfer of energy between the spins and a reservoir. Spin 1/2 nuclei have two levels specified by $m = \pm 1/2$ with the respective occupancies, $N_{\pm}$. The total number of spins, N, is constant and is simply the sum of the number in the upper and lower states, $N_+ + N_-$. Assuming the probably of transition from the upper state to the lower state is equal the probability transition from the lower state to the upper state, the rate of change of the number of upper state spins is then proportional to the difference in number of spins between the upper and lower state,

$$\frac{dN_+}{dt} = W(N_- - N_+) \qquad \text{Eqn 3.1}$$

where the proportionality constant, W, is the probability of transition of a upper state spin going into the lower state. Defining $N=N_+ + N_-$ as the total population and $n=N_+ - N_-$ as difference and substituting into eqn 3.1 gives,

$$\frac{dn}{dt} = -2Wn \qquad \text{Eqn 3.2}$$

whose solution is,

$$n = n(0)e^{-2Wt} \qquad \text{Eqn 3.3}$$

Thus equilibrium is obtained via a first order process with a characteristic time

$$\frac{1}{T_1} = \frac{1}{2W} \qquad \text{Eqn 3.4}$$

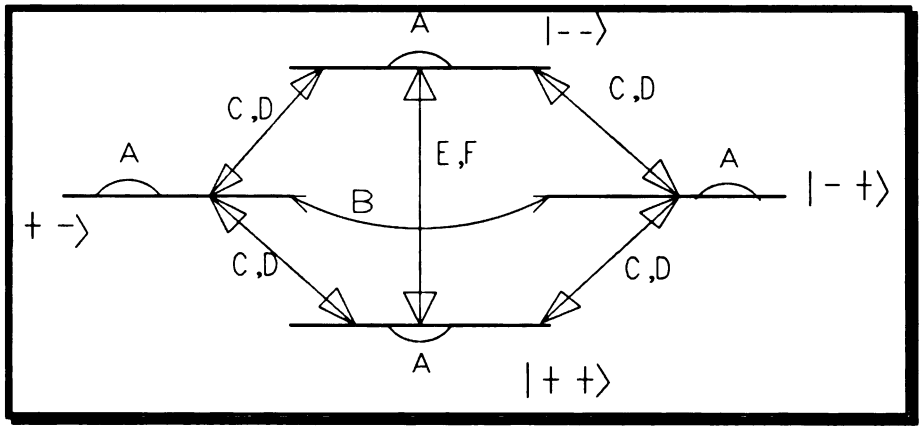

Figure 3.1

Diagram of relaxation pathways. The terms A,B,.. F, are described in Abragam [*12*] and in Solomon [*11*]. The notations used in the two articles are different. Abragam uses A, B,.. and Solomon uses w_i's. Throughout the text, w_0=B, w_1=C, w_2=E are used interchangeably.

A more elaborate presentation is Solomon's [*11*] relaxation theory for two spins. Represented in figure 3.1 as A, B, C, D, E, F (to keep the standard notation used in the dipolar discussion) the different transitions (w_i) used in Solomon's theory is simple w_0=B, w_1=C, w_2=E and the primes are the opposite rate constants B, D, F, respectively. The rate equations for T_1 are,

$$\begin{bmatrix} dN_{++} \\ dN_{+-} \\ dN_{-+} \\ dN_{--} \end{bmatrix} = \begin{bmatrix} -(w_1 + w_1' + w_2) & w_1' & w_1 & w_2 \\ w_1' & -(w_1 + w_1' + w_0) & w_0 & w_1 \\ w_1 & w_0 & -(w_1 + w_1' + w_0) & w_1' \\ w_2 & w_1 & w_1' & -(w_1 + w_1' + w_2) \end{bmatrix} \begin{bmatrix} N_{++} \\ N_{+-} \\ N_{-+} \\ N_{--} \end{bmatrix} + C$$

Eqn 3.5

The system of equation for T_2 is identical, with the replacement of N with $|\alpha\rangle$, $|\beta\rangle$ for $|+\rangle$, $|-\rangle$ and u_i for w_i respectively.

$$\begin{bmatrix} dN_{\alpha\alpha} \\ dN_{\alpha\beta} \\ dN_{\beta\alpha} \\ dN_{\beta\beta} \end{bmatrix} = \begin{bmatrix} -(u_1 + u_1' + u_2) & u_1' & u_1 & u_2 \\ u_1' & -(u_1 + u_1' + w_0) & u_0 & u_1 \\ u_1 & u_0 & -(u_1 + u_1' + w_0) & u_1' \\ u_2 & u_1 & u_1' & -(u_1 + u_1' + u_2) \end{bmatrix} \begin{bmatrix} N_{\alpha\alpha} \\ N_{\alpha\beta} \\ N_{\beta\alpha} \\ N_{\beta\beta} \end{bmatrix} + C$$

Eqn 3.6

The constant C characterizes the thermal equilibrium state and is not important for relaxation calculations. Calculations for T_2 are identical as done with T_1 calculations. The expectation for two different spins, $\langle I \rangle$ and $\langle S \rangle$, is proportional to the difference in populations,

$$\begin{aligned}(N_{++}+N_{+-})+(N_{+-}+N_{--}) &= K\langle I_z\rangle \\ (N_{++}+N_{-+})+(N_{-+}+N_{--}) &= K\langle S_z\rangle\end{aligned} \qquad \text{Eqn 3.7}$$

where K is the proportionality constant. Replacing equation 3.7 into 3.5 and subtracting the equilibrium value of I and S gives the expectation values rate of change for the *longitudinal* component as,

$$\frac{d}{dt}\begin{bmatrix}\langle I_z\rangle \\ \langle S_z\rangle\end{bmatrix} = \begin{bmatrix}-(w_0+2w_1+w_2) & -(w_2-w_0) \\ -(w_2-w_0) & -(w_0+2w_1+w_2)\end{bmatrix}\begin{bmatrix}\langle I_z\rangle - I \\ \langle S_z\rangle - S_0\end{bmatrix} \qquad \text{Eqn 3.8}$$

and following the identical steps for the *transverse* relaxation gives,

$$\frac{d}{dt}\begin{bmatrix}\langle I_x\rangle \\ \langle S_x\rangle\end{bmatrix} = \begin{bmatrix}-(u_0+2u_1+u_2) & -(u_2-u_0) \\ -(u_2-u_0) & -(u_0+2u_1+u_2)\end{bmatrix}\begin{bmatrix}\langle I_x\rangle \\ \langle S_x\rangle\end{bmatrix} \qquad \text{Eqn 3.9}$$

The first order transition probabilities is given as,

$$w_{ij} = \frac{1}{t\hbar}\left|\int_0^t \langle m_j|\mathcal{H}(t)|m_i\rangle e^{-i\omega_{ij}t}dt\right|^2 \qquad \text{Eqn 3.10}$$

where

$$\omega_{ij} = \frac{(E_i - E_j)}{\hbar}$$

The real work is in the calculation of the transition probabilities which depend on the mechanism of relaxation and knowing the transition probabilities will allow us to calculate T_1 and T_2 by replacing the transition probabilities into equation 3.8 and 3.10, respectively.

The molecular dynamics induces relaxation in five ways which categorize into five mechanisms and are listed as follows,

1. Nuclear dipole-dipole
2. Nuclear quadrupolar
3. Scalar
4. Anisotropic
5. Spin-rotation

The last three categories (scalar, anisotropic, spin-rotation) are minor contributors to the relaxation in tissue so only brief descriptions are given of these items (for completeness), whereas most of the discussion will be of the dipole-dipole relaxation and somewhat less for quadrupolar relaxation.

Correlation Times

Intrinsic to the theory of relaxation in liquids and in tissue is the concept of correlation time τ_c, which for our model, describes the classical random tumbling of a spin. Discussion on correlation time will be restricted to tumbling, being that the dominant term for tissue is rotational. An important definition frequently used in relaxation calculations is the autocorrelation function [*14*], defined as,

$$G(\tau) = \lim_{T\to\infty} \frac{1}{2T} \int_{-T}^{T} x(t)x(t+\tau)dt \qquad \text{Eqn 3.11}$$

This definition describes the time relationship and influence between a pair of random variables arising from the same random process. The spectral density of the autocorrelation function is the Fourier transform of G,

$$J(\omega) = \int_{-\infty}^{\infty} G(\tau)e^{-i\omega\tau}d\tau \qquad \text{Eqn 3.12}$$

Many relaxation calculations assume a $e^{-|t|/\tau_c}$ dependence (including the original BPP paper) for the correlation function, with τ_c being the correlation time. Dielectric calculations [*15*] use a decaying function

$$\alpha(t) = \frac{\varepsilon_s - \varepsilon_\infty}{\tau} e^{-t/\tau} \qquad \text{Eqn 3.13}$$

with

ε_s = static dielectric

ε_∞ = dielectric constant as $\omega \rightarrow \infty$

τ = dielectric relaxation time

to derive the basic differential equation relating the electric displacement vector D and the electric field vector E. To show the plausibility of this $e^{-|t|/\tau_c}$ density function, we can calculate it for a situation where there are events with equal probabilities of occurring. Brownian motion is assumed to be, at a random time, equally probable at any given position. This assumption allows a derivable density function [14]. Given the average time between events as τ_c, then the probability of an event occurring in the interval Δt is $\Delta t/\tau_c$, with the assumption that Δt is short compared to τ_c. With an event occurring at t_0, the probability of the next event occurring at a random time between $t_0+\tau$ and $t_0+\tau+\Delta t$ is

$$P(t_0, t_0 + \tau + \Delta t) = P(\tau + \Delta t) + P(\tau) \qquad \text{Eqn 3.14}$$

where

$P(\tau)$ = distribution function for τ

This is also equal to the probability that the event did not occur in the interval t_0 and $t_0+\tau$ and the event occurring between $t_0+\tau$ and $t_0+\tau+\Delta t$. Equating this with the previous equation gives

$$P(\tau + \Delta t) + P(\tau) = [1 - P(\tau)]\left(\frac{\Delta t}{\tau_c}\right) \qquad \text{Eqn 3.15}$$

dividing both sides by Δt and letting Δt approach zero gives

$$\lim_{\Delta t \to 0} \frac{P(\tau+\Delta t)+P(\tau)}{\Delta t} = \frac{dP(\tau)}{d\tau} = [1-P(\tau)]\left(\frac{1}{\tau_c}\right) \qquad \text{Eqn 3.16}$$

solving for P(τ) gives

$$P(\tau) = 1 - e^{-\tau/\tau_c} \qquad \text{Eqn 3.17}$$

differentiation gives the density function p(τ),

$$p(\tau) = \frac{1}{\tau_c} e^{-\tau/\tau_c} \qquad \text{Eqn 3.18}$$

for $\tau \geq 0$ and zero elsewhere.

In magnetic resonance, average time between events is synonymous to the correlation time, τ_c. The physical relationship of correlation time can be shown with help from Debye [*15*]. Debye's model assumes that the molecule has $\Omega t/\alpha$ collisions in time *t*, Ω is the angular velocity and α rotational mean free path. A modification of the Debye's model is required because the function whose correlation time in Debye's theory is $\cos\theta$, while what is needed in MRI is a $\cos^2\theta$ dependency. Debye's equation for the probability, $p(\theta,\phi,t)$, of the nuclei being a certain angle on a surface of a sphere is described by the diffusion equation, given in spherical coordinate with D as the coefficient of diffusion. Debye proposed that the angle θ between the dipole moment and the applied field is proportional to $\langle\cos\theta(t)\rangle$ and has the value

$$\langle\cos\theta(t)\rangle = e^{-2Dt} = e^{-t/\tau_D} \qquad \text{Eqn 3.19}$$

where τ_D is the Debye correlation time. Magnetic resonance has very similar angular dependence as will be discussed in the dipolar section, which is F_0,

$$\tfrac{1}{2}\langle 3\cos^2\theta(t)\rangle = e^{-6Dt} = e^{-t/\tau_c} \qquad \text{Eqn 3.20}$$

Following Debye's method, this can give a rough estimate of the correlation time for a sphere in a viscous fluid via the Einstein's relation

$$D = \frac{kT}{8\pi\eta a^3} \qquad \text{Eqn 3.21}$$

or equating to the correlation time,

$$\tau_c = \frac{4\pi\eta a^3}{3kT} \qquad \text{Eqn 3.22}$$

where

η = viscosity of the fluid
a = radius of sphere
k = Boltzmann Constant
T = Abosolute temperature

This relationship between the size of the molecule, temperature, and correlation time is a fairly important concept used just about anytime a connection between these variables are needed. Though the calculations many seem artificially simplified, the results from more complicated calculations have results that differ very little.

Scalar Coupling

The two variations of scalar coupling (or *J*-coupling) have the relaxation mediated by the chemical bond (electron mediated) and cause bond dependent line splitting. Scalar coupling of the first kind is when the chemical exchange rate and the longitudinal relaxation rate are much larger than the scalar coupling constant. The relaxation rate of the I spins as induced by the S spins is given by the expressions,

$$\frac{1}{T_{1I}} = \frac{2A^2}{3} S(S+1)\left\{\frac{\tau_e}{1+(\omega_I - \omega_S)^2 \tau_e^2}\right\}$$
$$\frac{1}{T_{2I}} = \frac{A^2}{3} S(S+1)\left\{\tau_e + \frac{\tau_e}{1+(\omega_I - \omega_S)^2 \tau_e^2}\right\} \qquad \text{Eqn 3.23}$$

where τ_e is the exchange time. The ratio of T_1/T_2 is,

$$\frac{T_1}{T_2} = 1 + (\omega_I - \omega_S)^2 \frac{\tau_e^2}{2} \qquad \text{Eqn 3.24}$$

If $(\omega_I - \omega_S)\tau_e$ is not vanishing small, T_1 and T_2 will be field dependent and the ratio will be greater than one.

Scalar coupling of the second kind is the opposite situation where the chemical exchange and longitudinal relaxation rate are shorter than the scalar coupling constant. The expressions for scalar relaxation of the second kind,

$$\frac{1}{T_{1I}} = \frac{2A^2}{3} S(S+1) \left\{ \frac{\tau_2}{1 + (\omega_I - \omega_S)^2 \tau_2^2} \right\}$$
$$\frac{1}{T_{2I}} = \frac{A^2}{3} S(S+1) \left\{ \tau_1 + \frac{\tau_e}{1 + (\omega_I - \omega_S)^2 \tau_2^2} \right\} \qquad \text{Eqn 3.25}$$

is very similar to scalar relaxation of the first kind, where the difference is the replacement the exchange time with the relaxation times of the S nuclei, (i.e. $\tau_e \rightarrow \tau_1, \tau_2$).

Chemical Shift Anisotropy

Chemical shift anisotropic relaxation depends on the applied field's asymmetric effects due to the chemical shielding tensor σ. For short correlation times, τ_c,

$$\frac{1}{T_1} = \frac{g_N^2 \beta_N^2 H_0^2}{10\hbar^2} \left(\sigma_1'^2 + \sigma_2'^2 + \sigma_3'^2 \right) 2\tau_c \qquad \text{Eqn 3.26}$$

Where σ_i' is the anisotropic portion of the chemical shift tensor along the i^{th} principal axis. And for a nucleus with axial symmetry,

$$\frac{1}{T_1} = \tfrac{2}{15} \gamma^2 B_0 \Delta\sigma^2 \frac{\tau_c}{1 + \omega^2 \tau_c^2}$$
$$\frac{1}{T_2} = \tfrac{1}{90} \gamma^2 B_0 \Delta\sigma^2 \left[\frac{6\tau_c}{1 + \omega^2 \tau_c^2} + 8\tau_c \right] \qquad \text{Eqn 3.27}$$

where $\Delta\sigma$ is the chemical shift anisotropy. For short correlation times, the two relaxation times are not equal, rather their ratio is T_1/T_2=7/6. The field dependence of T_1 relaxation rate is the square of the field strength.

Spin Rotation

Spin-rotation relaxation arises from the magnetic field produced by the motion of the nuclei and electrons. The induced field is proportional to the rotational angular momentum. For short correlation times, τ_j, the relaxation rate is,

$$\frac{1}{T_1} = \frac{2\tau_j}{9\hbar^2}\left(C_1^2 + C_2^2 + C_3^2\right)\langle J(J+1)\rangle \qquad \text{Eqn 3.28}$$

where C_i are the principal values of the spin-rotation tensor, and J is the rotation angular momentum. The two relaxation times are equal for short correlation times. Spin rotation does not have field dependencies.

Nuclear Dipole-Dipole Relaxation

Dipole-dipole relaxation is the primary pathway for proton relaxation for both T_1 and T_2 (nuclei without a dipole moment will obviously not have this interaction as a relaxation pathway). Dipole-dipole relaxation is caused by the interaction between a pair of spins via the magnetic dipole. The classical interaction energy is given by

$$V = \frac{\mu_1 \cdot \mu_2}{r^3} - \frac{3(\mu_1 \cdot r)(\mu_2 \cdot r)}{r^5} \qquad \text{Eqn 3.29}$$

where $\mu_{1,2}$ is the magnetic moment for the two spins. The quantum mechanical interaction energy has μ replaced with $\hbar\gamma I$. A rigid model of water is shown in Figure 3.1. The spatial relationships between the atoms are fixed but the molecule is allowed to rotate. The distance between the two hydrogen's is a constant, but the angular relationship between the spin varies. The angular variation is the main contributor to the intra molecular relaxation. The dipolar relaxation can be separated into two terms, intra-molecular (same molecule), and inter-molecular (different

molecules). The larger contribution to the dipolar relaxation is the intra-molecular rather than the inter-molecular interactions because of cubic dependency to distance.

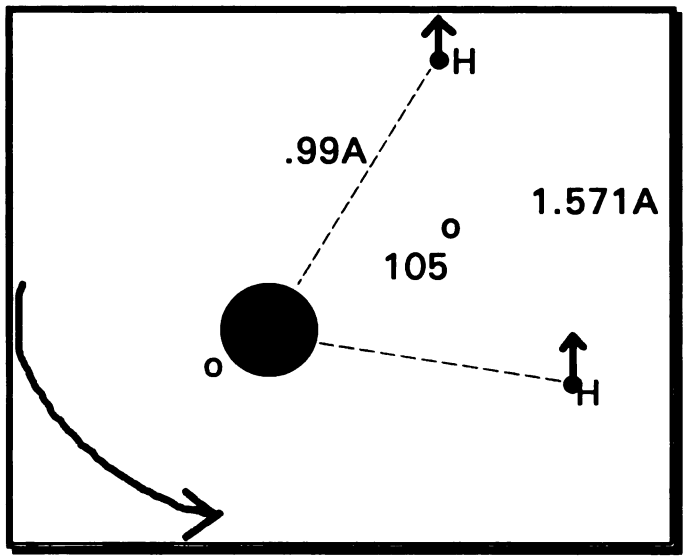

Figure 3.2
Pictorial representation of a water molecule. The hydrogen and oxygen nuclei rotate about the center of mass in a rotational Brownian motion.

For a more rigorous calculation, consider a pair of magnetic dipole, I and S, (in a water molecule) as shown in figure 3.2 . The field that spin I experiences has two contributions, the static field and local field produced by spin S. The static contribution of the Hamiltonian is the Zeeman Hamiltonian and the local contribution is the dipolar Hamiltonian,

$$\begin{aligned}\mathcal{H} &= \mathcal{H}_z + \mathcal{H}_{loc} \\ &= -\gamma_1 \hbar H_0 I_{1z} - \gamma_2 \hbar H_0 I_{2z} + \mathcal{H}_{dipolar}\end{aligned} \qquad \text{Eqn 3.30}$$

The dipolar term for N spins is given as

$$\mathcal{H}_{dipolar} = \frac{1}{2}\sum_{j=1}^{N}\sum_{k=1}^{N}\left[\frac{\mu_j \cdot \mu_k}{r_{jk}^3} - \frac{3(\mu_j \cdot r_{jk})(\mu_k \cdot r_{jk})}{r_{jk}^5}\right] \qquad \text{Eqn 3.31}$$

expanding $\mathcal{H}_{dipolar}$ for a pair spins

$$\mathcal{H}_{dipolar} = \frac{\gamma_1 \gamma_2 \hbar^3}{r^3}(A + B + C + D + E + F) \qquad \text{Eqn 3.32}$$

where

$$A = I_z S_z F_0$$
$$B = -\tfrac{1}{4}\left(I^+ S^- + I^- S^+\right) F_0$$
$$C = -\tfrac{3}{2}\left(I^- S_z + I_z S^-\right) F_1^*$$
$$D = -\tfrac{3}{2}\left(I^+ S_z + I_z S^+\right) F_1$$
$$E = -\tfrac{3}{4} I^+ S^+ F_2^*$$
$$F = -\tfrac{3}{4} I^- S^- F_2$$

and

$$F_0 = \left(1 - 3\cos^2\theta\right)$$
$$F_1 = \sin\theta\cos\theta e^{-i\varphi}$$
$$F_2 = \sin^2\theta e^{-2i\theta}$$

I^+ and I^- are raising and lower angular momentum operators and the F_i are the spatial Fourier spectra. Abragam [12] describes the physical significance of each term and its implications. A water molecule is a tri-state system with three levels as shown in figure 3.1 with the transition pathway drawn in to represent the 6 dipolar terms of eqn. 3.32. The water tri-state is really a quad-state but the calculation assumes that the states $|+-\rangle$ and $|-+\rangle$ are equal thus reducing the number of states by one. Following the outline of the BPP theory, the standard form for the correlation function is,

$$\begin{aligned} K_i(\tau) &= \left\langle F_i(t) F_i^*(t+\tau) \right\rangle \\ &= \left\langle F_i(t) F_i^*(t) \right\rangle e^{-|\tau|/\tau_c} \end{aligned} \qquad \text{Eqn 3.33}$$

and is the place where the correlation time, τ_c, appears. The Fourier spectra are simply the Fourier transform of $K(\tau)$,

$$J_i(\omega) = \int_{-\infty}^{\infty} K_i(\tau) e^{i\omega\tau} d\tau$$

$$\int_{-\infty}^{\infty} \left\langle F_i(t) F_i^*(t) \right\rangle e^{-|\tau|/\tau_c} e^{i\omega\tau} d\tau \qquad \text{Eqn 3.34}$$

Resulting in the following form for the Fourier spectra,

$$J_0(\omega) = \int_{-\infty}^{\infty} \left(1 - 3\cos^2\theta\right)^2 e^{i\omega\tau} d\tau = \frac{24}{15r^6}\left(\frac{\tau_c}{1+\omega^2\tau_c^2}\right)$$

$$J_1(\omega) = \int_{-\infty}^{\infty} \left(\sin\theta\cos\theta\right)^2 e^{i\omega\tau} d\tau = \frac{4}{15r^6}\left(\frac{\tau_c}{1+\omega^2\tau_c^2}\right) \qquad \text{Eqn 3.35}$$

$$J_2(\omega) = \int_{-\infty}^{\infty} \left(\sin^2\theta\right)^2 e^{i\omega\tau} d\tau = \frac{48}{45r^6}\left(\frac{\tau_c}{1+\omega^2\tau_c^2}\right)$$

Replacing the spatial Fourier functions in the transition probability equation, Eqn 3.10 and integrating will give the transition probabilities. The transition probabilities will depend on whether the interacting spins are the same (i.e. same γ's) or different (unlike spins). For *like spins*, where $\omega_S = \omega_I = \omega$, the transition probabilities for the *longitudinal* component are,

$$w_0 = \frac{\tau_c}{8\hbar^2}\left\langle F_0^2 \right\rangle$$

$$w_1 = w_1' = \frac{\tau_c}{2\hbar^2}\left\langle \left|F_1^2\right| \right\rangle \frac{1}{1+\omega^2\tau_c^2} \qquad \text{Eqn 3.36}$$

$$w_2 = \frac{2\tau_c}{\hbar^2}\left\langle \left|F_2^2\right| \right\rangle \frac{1}{1+4\omega^2\tau_c^2}$$

and the transition probabilities for the *transverse* components are,

$$u_0 = \frac{\tau_c}{8\hbar^2}\left[\frac{\left\langle F_0^2 \right\rangle}{4} + \left\langle \left|F_2\right|^2 \right\rangle \frac{2}{1+4\omega^2\tau_c^2}\right]$$

$$u_1 = u_1' = \frac{\tau_c}{8\hbar^2}\left[\left\langle \left|F_1\right|^2 \right\rangle \frac{2}{1+\omega^2\tau_c^2} + \left\langle \left|F_2\right|^2 \right\rangle \frac{2}{1+4\omega^2\tau_c^2}\right] \qquad \text{Eqn 3.37}$$

$$u_2 = \frac{\tau_c}{8\hbar^2}\left[\frac{9}{2}\left\langle \left|F_0\right|^2 \right\rangle + \left\langle \left|F_1\right|^2 \right\rangle \frac{8}{1+\omega^2\tau_c^2} + \left\langle \left|F_2\right|^2 \right\rangle \frac{2}{1+4\omega^2\tau_c^2}\right]$$

The regime that we are interested in is the motional narrowing regime. The averages of the angular functions in the regime, where the angular dependencies are averaged out, are

$$\left\langle F_0^2 \right\rangle = \left\langle 1 - 3\cos^2\theta \right\rangle = \frac{4}{5}$$
$$\left\langle |F_1|^2 \right\rangle = \left\langle \sin^2\theta\cos^2\theta \right\rangle = \frac{2}{15} \qquad \text{Eqn 3.38}$$
$$\left\langle |F_2|^2 \right\rangle = \left\langle \sin^4 \right\rangle = \frac{8}{15}$$

replacing these values for the angular functions values in eqn 3.9 gives the relaxation rates for *like spins,*

$$\frac{1}{T_1} = \frac{6}{20}\frac{\hbar^2\gamma^4}{b^6}\left[\frac{\tau_c}{1+\omega^2\tau_c^2} + \frac{4\tau_c}{1+4\omega^2\tau_c^2}\right]$$
$$\frac{1}{T_2} = \frac{3}{20}\frac{\hbar^2\gamma^4}{b^6}\left[3\tau_c + \frac{5\tau_c}{1+\omega^2\tau_c^2} + \frac{2\tau_c}{1+4\omega^2\tau_c^2}\right] \qquad \text{Eqn 3.39}$$

The case of unlike spins is important to the cross relaxation because of the calculations between a quadrupolar and spin 1/2 nuclei are very similar to the like spin calculations for the w_I terms. However, the calculations are more involved. The net results of the transition probabilities with the motional narrowed conditions for *unlike spins* are

$$\frac{1}{T_1} = \frac{1}{10}\frac{\hbar^2\gamma_I{}^2\gamma_S{}^2}{b^6}\left[\frac{\tau_c}{1+(\omega_I-\omega_S)^2\tau_c^2} + \frac{\tau_c}{1+4\omega^2\tau_c^2} + \frac{\tau_c}{1+(\omega_I+\omega_S)^2\tau_c^2}\right]$$
$$\frac{1}{T_2} = \frac{\hbar^2\gamma_I{}^2\gamma_S{}^2}{20b^6}\left[4\tau_c + \frac{\tau_c}{1+(\omega_I-\omega_S)^2\tau_c^2} + \frac{3\tau_c}{1+\omega_I^2\tau_c^2} + \frac{6\tau_c}{1+\omega_S^2\tau_c^2} + \frac{6\tau_c}{1+(\omega_I+\omega_S)^2\tau_c^2}\right]$$

Eqn 3.40

For both cases, in the motional narrowing limit, $1/T_1 = 1/T_2$ and is frequency independent, or in other words, there is no dispersion for either case in the motional narrowing case.

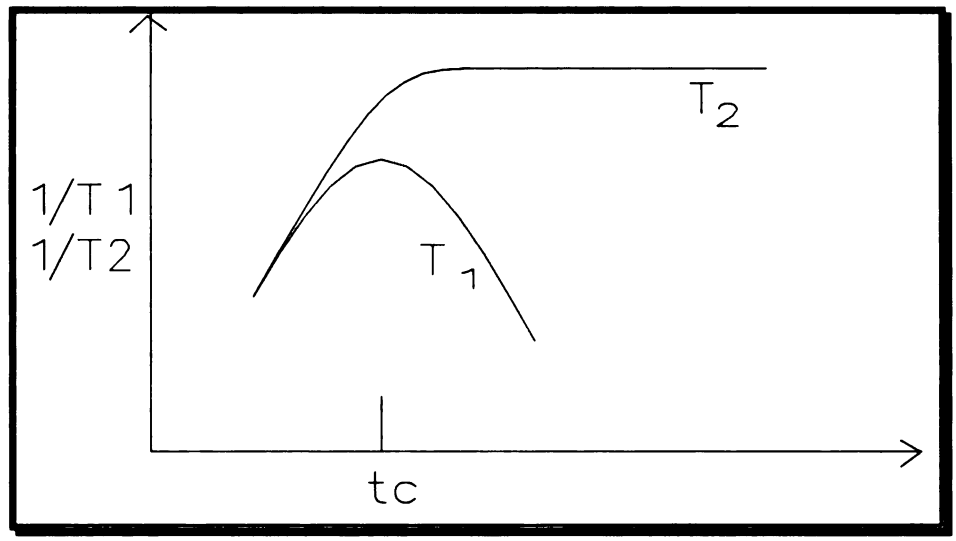

Figure 3.3
Relaxation times as a function of correlation time. The motional narrowing limit has $T_1 \sim T_2$. Very long correlation times have very short T_2's and long T_1's. Very short correlation times have $T_1 = T_2$.

The behavior of dipolar relaxation given by equation 3.8 is shown in figure 3.3. The longitudinal relaxation rate reaches a maximum when $\omega_0 \tau_c \sim 1/\sqrt{2}$ while the transverse relaxation rate is monotonic increasing until $\omega\tau_c \sim 1/\sqrt{2}$, where the rate levels to a constant value. This graph gives a qualitative description of relaxation behavior for different states of matter. A solid-like material has a very long correlation time, which is represented by the right hand region of the graph, giving very short T_2's and long T_1's. The behavior can be seen from equation 3.8. The very short correlation times, represented by the left region of the graph, have $T_1 = T_2$. The region most representative of tissue is the central portion. Water at room temperature is definitely in the motional narrowing limit so if water protons were the primary nuclei imaged, tissue relaxation dispersion should behave somewhat like diamagnetic doped water.

Quadrupole relaxation

Nuclei with spin greater than 1/2 have a quadrupolar moment because the nuclei are no longer spherically symmetric. The magnitude of the quadrupolar constant depends on the nucleus site symmetry that dictates the magnitude of the electric field gradient. For example, sites of cubic symmetry will have the three axis quadrupolar terms equal thus making the quadrupolar terms in

the Hamiltonian cancel. The Hamiltonian H_S of S spins is composed of the Zeeman (H_Z) and the quadrupole (H_Q) contributions. For Nitrogen ($S = 1$), the Hamiltonian is [*12*],

$$\begin{aligned} H_S &= H_Z + H_Q \\ &= -\gamma_S \hbar \boldsymbol{B}_o \cdot \boldsymbol{S} + K \frac{6S_z^2 - 4 + \eta(S_+^2 + S_-^2)}{2} \end{aligned} \qquad \text{Eqn 3.41}$$

where γ_S is the magnetogyric ratio of the S nuclei, $\boldsymbol{S}=(S_x,S_y,S_z)$ is the spin operator of the S-nuclei, $S_\pm = S_x \pm S_y$, are the raising and lowering spin operators, $K=(e^2qQ/4)$, Q is the nuclear electric quadrupole moment, and η the asymmetry factor. The quadrupolar relaxation rates are

$$\begin{aligned} \frac{1}{T_1} &= \frac{3}{80}\left(1+\frac{\eta^2}{3}\right)\left(\frac{eQ}{\hbar}\frac{\partial^2 V}{\partial z'^2}\right)^2 \{J(\omega)+4J(2\omega)\} \\ \frac{1}{T_2} &= \frac{1}{160}\left(1+\frac{\eta^2}{3}\right)\left(\frac{eQ}{\hbar}\frac{\partial^2 V}{\partial z'^2}\right)^2 \{9J(0)+15J(\omega)+6J(2\omega)\} \end{aligned} \qquad \text{Eqn 3.42}$$

where the $J(\omega)$ and $J(2\omega)$ are the same spectra's densities given in the dipolar section. The solution to the quadrupolar Hamiltonian is solvable for the high and low field cases. The result that is important to this experiment is the low field case where the quadrupole term dominates the Zeeman term, that is,

$$\begin{aligned} K &>> \hbar\gamma_s B_0 \\ B_0 &<< \frac{e^2qQ}{4\hbar\gamma_s} \end{aligned} \qquad \text{Eqn 3.43}$$

Estimating the quadrupolar relaxation for a typical protein will get a ballpark figure on the magnitude of the quadrupolar relaxation in relationship to the total relaxation. The ^{14}N quadrupole coupling constant for a typical nitrogen in a protein is,

$$\frac{4K}{\hbar} = \frac{e^2qQ}{\hbar} \approx 10^7 \text{ Hz} \qquad \text{Eqn 3.44}$$

Given that the magnetogyric ratio for nitrogen is, $\gamma_S = 3.075\text{MHz}\cdot\text{T}^{-1}$ and the symmetry parameter η=0.1, the low field limit has the value, $B_0 \le 0.8\text{T}$. The field range used in this experiment was 0.0340-0.1011 T, so the low field requirement is easily met. The three transition frequencies for a spin 1 nucleus with a given asymmetry factor η are,

$$\omega_1 = \frac{K}{\hbar}\left[3 - \eta\sqrt{1+a^2}\right]$$
$$\omega_2 = \frac{K}{\hbar}\left[3 + \eta\sqrt{1+a^2}\right] \qquad \text{Eqn 3.45}$$
$$\omega_3 = \frac{2K}{\hbar}\eta\sqrt{1+a^2}$$

where

$$a = \frac{\gamma_S \hbar B_0 \cos\theta}{K\eta}$$
$$K = \frac{e^2 qQ}{4}$$

Equation 3.45 simplifies for the motional narrowed case which essentially "averages" any angular dependencies (i.e. the a term averages to zero) giving,

$$\omega_1 = \frac{K}{\hbar}[3 - \eta]$$
$$\omega_2 = \frac{K}{\hbar}[3 + \eta] \qquad \text{Eqn 3.46}$$
$$\omega_3 = \frac{2K}{\hbar}\eta$$

Assuming that the primary interaction between quadrupolar nuclei and spin 1/2 nuclei is dipolar, the dipolar interaction Hamiltonian is given by equation 3.31 and following the procedure previously given for the dipolar calculations will give the quadrupolar cross relaxation.

Quadrupolar Cross Relaxation

The hydrogen nuclear relaxation dispersion curve has fine structure at 350-800 Gauss. The curve shows two dips thought to be caused by cross relaxation of the hydrogen by nitrogen. The motional narrowing T_1 for coupled spin 1/2 and spin 1 nuclei where I is the spin 1/2 nuclei and S is the spin 1 nuclei, is given by [*16*],

$$\frac{1}{T_{1I}} = \frac{\mu_0 \gamma_I \gamma_S \hbar^2}{12\pi r_{IS}^3}\left\{\begin{array}{c} \frac{1}{2}\left(\frac{2}{3} + \sin^2\theta_S\right)[j(\omega_1 - \omega_I) + j(\omega_1 + \omega_I) \\ + j(\omega_2 - \omega_I) + j(\omega_2 + \omega_I)] \\ + \left(\frac{4}{3} - \sin^2\theta_S\right)[j(\omega_3 - \omega_I) + j(\omega_3 + \omega_I)] \end{array}\right\} \qquad \text{Eqn 3.47}$$

Where

θ_S = Polar angle of r_{IS} in the molecular frame

$\omega_{1,2,3}$ = the three quadrupolar transistion frequencies

ω_I = Larmor frequency of the spin 1/2 nuclei

$\gamma_{I,S}$ = Gyromagnetic ratio of the I and S nuclei respectively

$r_{I,S}$ = Distance between the I and S nuclei

and the other variables are the same as given in the previous section. The occurrence of the cross relaxation peak requires that the following three conditions to be met,

1. ω_I needs to cross the quadrupolar transition frequency ω_S ($\omega_I = \omega_S$)..
2. The spin lattice relaxation of the quadrupolar nuclei, S, must be fast compared to the I nuclei $(T_{1S} << T_{1I})$.
3. The quadrupolar correlation time needs to be relatively long $(\omega_q \tau_c > 1)$.

The first condition describes the requirement that the transitional frequencies of I and S spins must be the same for the cross relaxation to occur. This is diagrammed in figure 3.4 where the three horizontal lines are the pure quadrupolar transition frequencies solution for the motional narrowed case. The powdered solid solution will have the three frequencies dispersing with increasing frequencies, represented by the curves that deviate from the horizontal lines. The slope line is simply $\omega = \gamma B_0$. The three intersection points of this line are where the dips should occur.

The second condition describes the transfer of energy from the I spins to the S spins where the relaxation of the S spins is much faster than the I spins so the S spins act as sinks. Hence the examination of relaxation of the I spin at the crossing frequencies is really investigating a pair of relaxation pathways, one the normal pathway to the lattice, and the second through the S spins to the lattice.

The third is saying that the quadrupolar splitting is observable if the molecular reorientation occurs adiabatically. No dips occur when $\omega_q \tau_c << 1$ and the dips become more pronounce with longer correlation times. The number of dips is affected by the asymmetry parameter η . For axial

symmetry, $\eta = 0$, a single dip occurs. For $\eta > 0$, three dips occur and two coincide when η approaches 1. Another condition that dictates the occurrence of multiple dips is when $\omega_3 \tau_c > 1$.

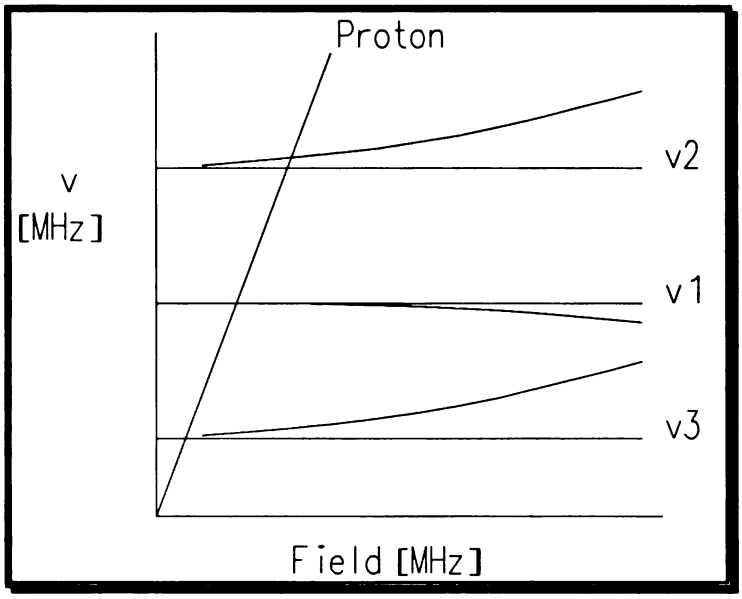

Figure 3.4
The three quadrupolar transition frequencies are v1, v2, and v3. The solid horizontal lines are the pure quadrupolar transition and the curves represent the ranges that the three transition frequencies have for different molecular orientations. The pure transition occurs in the motional narrowing case. The single sloped line is the proton transition frequency

The asymmetry factor, η, also determines the number of peaks in the dispersion curves, which can easily be seen from equation 3.46. For axial symmetry, the asymmetry factor is zero, i.e. $\eta = 0$, which gives a single peak at

$$\omega_1 = \omega_2 = \frac{3K}{\hbar} \qquad \text{Eqn 3.48}$$
$$\omega_3 = 0$$

For $\eta > 0$, three peaks are present and for $\eta = 1$, two are present with $\omega_1 = \omega_2$ being equal making these two peaks coalesce. The coalesced peak will display twice the intensity of a single peak.

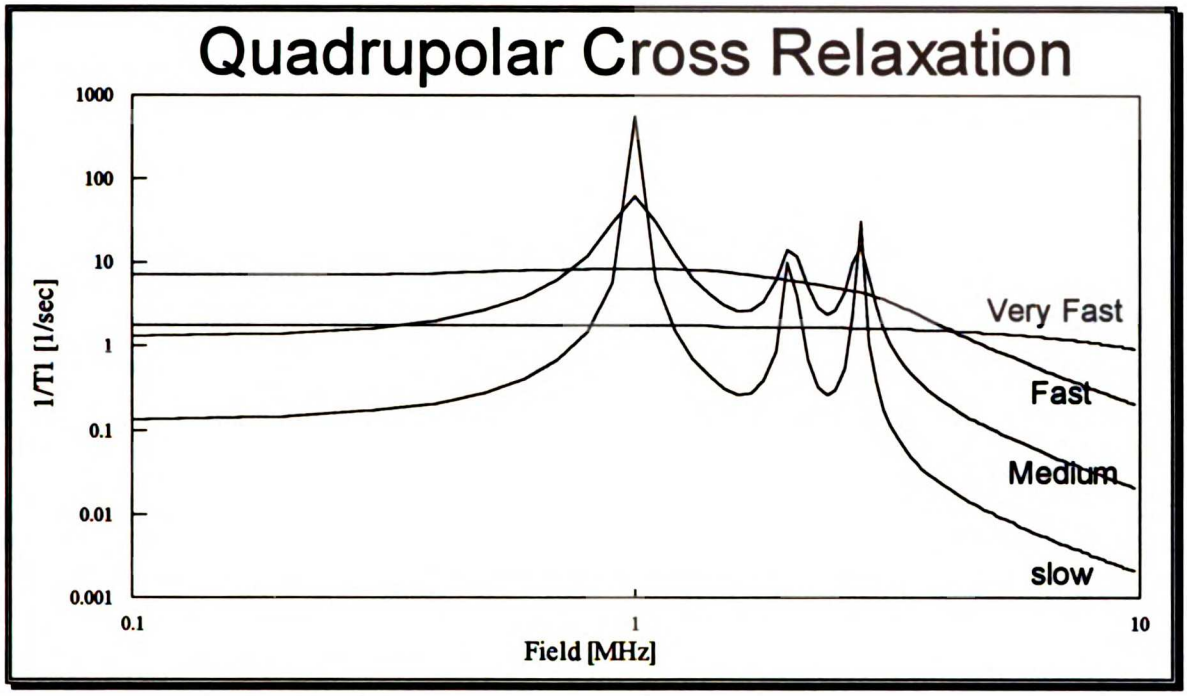

Figure 3.5
Quadrupolar cross relaxation dispersion for different correlation times. The correlation times have $\omega\tau_c$~.1 for very fast, $\omega\tau_c$~1 for fast, $\omega\tau_c$~10 for medium, and $\omega\tau_c$~100 for slow.

Implementation of equation 3.47 requires a intensity function for $j(\omega)$. Winter and Kimmich [*16*] show calculations with two different intensity functions to fit bovine serum albumin (BSA) data,

$$j(\omega) = \frac{2\tau_c}{1+\left(\omega_I - \omega_q\right)^2 \tau_c^2} \quad \text{and} \quad j(\omega) = \frac{2\tau_c}{1+\left|\omega_I - \omega_q\right|\tau_c} \qquad \text{Eqn 3.49}$$

The first expression is the classic form used in the BPP theory and is the one used in the following analysis. Show in figure 3.5 are plots of four different correlation times for equation 3.47 to show the effects of different correlation times. The parameters used in calculating the graph is $\theta_s = 0$, $\eta = 0.5$ The very fast case has $\omega\tau_c$~.1 where the peaks are not visible and dispersion does not occur until roughly $\omega\tau_c$~1. This is the case for fast with $\omega\tau_c$~1 where the peaks are still not visible

but dispersion is clearly visible. The transition between $\omega\tau_c$~1 and $\omega\tau_c$~10 is when the peaks start to appear, beginning with single bulging peak and with longer correlation time will separate into three peaks. The medium plot is when $\omega\tau_c$~10. As the correlation time gets longer, the peaks narrow and the overall baseline becomes lower. The peaks become larger on the slow plot where $\omega\tau_c$~100.

The relative size of peaks is determined by the angle θ_s. This can be seen by examining equation 3.47. The two higher field peaks have the same amplitude and their size relative to the low field peak is determined by $\sin\theta_s$. They are equal when,

$$\frac{2}{3}+\sin^2\theta_s=\frac{4}{3}-\sin^2\theta_s \qquad \text{Eqn 3.50}$$

or when

$$\theta_s=\sin^{-1}\sqrt{1/3}=35^\circ$$

and the two peaks are relatively larger for smaller angles and the opposite for larger angles. The frequency where the proton and the ν_3 transition cross (~600 KHz) is difficult to observe but Kimmich and Keonig have seen it in muscle tissues.

Magnetization Transfer

Ttissues exhibit a mono exponential behavior despite being heterogeneous. Solving the magnetization transfer equation can elucidate the cause for the mono exponential behavior. Magnetization transfer can occur in two ways, by physical exchange of nuclei containing the spins or by spin exchange. Both pathways affect the relaxation rate by changes in the micro environment of the spins due to the spatial changes of the spins. The classical solution for a spin jumping between sites *A* and *B*, with the assumption that the only place where the spins relax is at these sites is given as [*17*],

$$\begin{aligned} M &= M_A + M_B \\ &= -\gamma_N H_1 M_0 \frac{f_A(\omega-\omega'_B)+f_B(\omega-\omega'_A)+i(P_{AB}-P_{BA})}{\left[(\omega-\omega'_A)+iP_{AB}\right]\left[(\omega-\omega'_B)+iP_{BA}\right]+P_{AB}P_{BA}} \end{aligned} \qquad \text{Eqn 3.51}$$

with

$P_{AB,BA}$ = probability of spin jumping from A to B , B to A

$$f_{A,B} = \frac{P_{AB,BA}}{P_{AB} + P_{BA}}$$

$$\omega'_{A,B} = \omega_0 - 1/T_{2_{A,B}}$$

The results of spin exchange depend on the rate of exchange P_{AB} and P_{BA}. For slow exchanges, where the rate of exchange is much less than the line splitting, $P << |\omega_A - \omega_B| = \delta\omega$, two lines with their natural line width are present. As the exchange rate approaches the line splitting, $P \approx \delta\omega$, the two lines coalesce into a single broad line and for very fast exchange rates the line narrows. The position of a coalesced line depends of the equilibrium fractions, $f_{A,B}$, with the line closer in frequency to the site with the larger fraction and dominating the lineshape for ratios greater than a factor of 3.

Tissue relaxation, which generally shows a single relaxation rate, can be modeled with the fast exchange two state model (FETS). The FETS model is essentially the case when the magnetization transfer is very fast. The meaning of the term *fast* for the FETS models is when the exchange rate is much less than the difference in correlation times. Other models for tissue can incorporate multiple relaxation sites and spin exchanges among them. This *compartmentalization* of relaxation centers has varying degrees of success with correlation within a tissue type but losing correlation when comparing among different tissues.

Chapter 4

Relaxation of tissue

The mechanism of proton relaxation in tissue is not well defined because of the complexity of tissue. The tissue's microenvironment has a profound effect on relaxation times. White and grey brain tissues have a 15% difference in hydrogen density but a factor of two difference in longitudinal relaxation times. Water content is a major parameter that dictates the relaxation time but water content alone cannot explain the dispersion effects. The hydration layer on the surface of the protein is believed to have the dispersive component, though the exact mechanism producing this dispersive effect is not known. Tissue relaxation is more complicated than a simple weighted average of a collection of proteins with their respective relaxation times.

Various authors have conjectured on the mechanism of tissue relaxation. A popular model is where the water molecule is influenced by neighboring proteins in a region commonly described as the *hydration layer*. The dynamics of the protein are conjectured to be transmitted through this region by some type of bonding of the water molecule to the protein, or maybe by the *slosh* effect where the protein's hydrodynamic effects are felt over a longer range of many water molecule diameters. Another popular model is exchange of magnetization, or *cross relaxation*, between the water and protein. Water exchanging rapidly between the heterogeneous phases with different relaxation times is another viable model that produces the require characteristics. Keonig accrued a substantial amount of relaxometry data for various tissues and proteins. The tissue tends to have the dispersion profile of cross linked proteins.

Protein Molecular Dynamics

Tissue is a "structured" collection of proteins as sort of an "enzyme catalyzed" machine. Different tissues have different collections of proteins. Protein molecular dynamics may give insights on how this interaction affects the hydrogen nuclei. Proteins are unique linear arrays (primary structures) of a combination of 20 different amino acids connected by peptide bonds. At one end is the amino terminus and the other end is the carboxl terminus, with an assorted combination of different residue side chains between the two ends. The linear array will fold (with external assistance or spontaneously) into a three dimensional conformation (secondary structure). The final functional form (conformation) of the protein may be in this secondary structure but some may continue to assemble into tertiary structures. Only in the final three dimensional structure (secondary or tertiary) will the protein function as designed. The amino sequence specifies the three dimensional structure. Protein enzymes have an active site that is determined by its conformation and sequence.

Amino acids contain a fair amount of hydrogen and typically have different chemical shifts depending on their bonding though imaging studies tend to design the experiment to minimize chemical shift artifacts. The intrinsic hydrogens are not the one's that are typically imaged in normal physiological tissue (because of the "solid" like relaxation characteristics of these hydrogens) rather it is mostly the tissue water. At low water concentration the intrinsic hydrogen can be significant. The model used by many molecular dynamicists is a sphere of a water molecule with a radius of 1.4 Å rolling on the surface of a protein. The surface of a protein is described by the van der Waals envelopes of the surface atoms. This accessible surface of the protein is what MRI'ist calls the hydration layer although the idea of a hydration layer does not imply only the surface. The hydration layer is the phase of water that has correlation with the dynamics of the proteins. The "binding" of water molecules may be hydrogen binding or due to hydrophilic forces. Hydrogen binding is a low energy electrostatic bond between a hydrogen and oxygen atom with a binding energy of -3kcal/mole. Hydrophilic bonds are not really bonds but rather a entropic interaction between the water molecules and the protein's exposed side chains. In the protein folding process where the hydrophobic residues clump together to avoid exposure to the solvent, the Gibbs free energy is an important term. The Gibbs free energy for a pair state of a random peptide chain and a native peptide chain is,

$$\begin{aligned} -RT\ln K &= \Delta G_{chain} \\ &= \Delta H_{Chain} - T\cdot\Delta S_{Chain} \end{aligned} \qquad \text{Eqn 4.1}$$

Where

K = equilbrium constant

$\Delta H = H_{Native} - H_{random}$

$\Delta S = S_{Native} - S_{random}$

The ability for the protein to fold or to stay in a native state is determined by the sum of the electrostatics energy and the difference in entropy. The random state entropy being higher than that of the native states gives ΔS as negative which means that the entropy term, $T \cdot \Delta S_{Chain}$, is positive. The electrostatic term, $\Delta H = H_{Native} - H_{random}$, is negative because the hydrogen bond and van der Waal energy is lower in the native state than in the random state. The competition between the electrostatic forces and entropy determines the stability of the protein. The solvent's Gibbs free energy must be included to complete the story. Including water into equation 4.12 gives

$$\Delta G_{total} = \Delta H_{water} + \Delta H_{Chain} - T \cdot \Delta S_{Chain} - T \cdot \Delta S_{water} \qquad \text{Eqn 4.2}$$

The sign and relative magnitude of each term for both the polar and nonpolar residues can be estimated. ΔS_{Chain} for both polar and nonpolar residues is negative. For nonpolar residues, the electrostatic terms are small with ΔH_{water} negative and ΔH_{Chain} positive. The entropic terms for nonpolar residues have ΔS_{water} positive and large .

The terms due to the polar groups are of more interest to the understanding of the hydration layer. The native structure of a globular protein in water has the hydrophobic portion buried within the protein and the charged residues on the surface. The backbone of the protein is charged with its polar amide and carbonyl groups, and typically has charge residues attached to it. The hydrophobic core, which wants nothing to do with the polar groups, has the polar groups and backbone "neutralized" by hydrogen bonding with other polar groups. ΔS_{water} is positive and small because of some "ordering" of water molecules around the protein. This is what relaxometrist describe as crystilline water. ΔH_{water} is negative and ΔH_{Chain} is positive with ΔH_{water} the larger of the two electrostatic terms for polar residues. The polar groups within the hydrophobic core bond with each other and the surface polar groups bond with water exposed to them.

Water is a polar molecule and it can hydrogen bond to the exposed polar groups. Depending on the length of time that the water molecule stays bound to the protein, the water molecule will "sense" the proteins motions. The hydration layer has these hydrophilic polar groups and large hydrophobic entropic term competing for the concentration of the water molecules along the

surface of the molecules. There are proteins that have water molecules bonded to them in a more stable manner but these water molecules can be categorized as "semi-permanently bound" relative to the relaxation times.

Proton relaxation is mediated by dipolar interactions. Experiments using isotopic substitution of D_2O for H_2O show a dramatic decrease in relaxation and are one of the ways to determine proton protein interactions. Assuming that the dynamics of the deuterium and water molecule have essentially the same hydrodynamics, the dipolar interaction between a protein proton and a water proton is more effective than the protein proton and a deuterium proton by a factor of 16.

$$\left(\frac{\gamma_H}{\gamma_D}\right)^2\left(\frac{I_H(I_H+1)}{I_D(I_D+1)}\right)=16 \qquad \text{Eqn 4.3}$$

Varying the dilution can reveal information about the number of protons and their interactions.

Koenig has kept to the idea of the special interfacial sites, using three in his model[*23*]. He proposed a hydration model where the water molecule can only be attached to the protein interface by hydrogen bonds. The three different sites have different correlation times, a short, a medium, and a long correlation time, labeled $\tau_{hyS}, \tau_{hyM}, \tau_{hyL}$ receptively. His deduction, from BSA relaxometry data, is that the long correlation time has the bound of $2.0\text{x}10^{-5}\,\text{s} \geq \tau_{hyL} \geq 5.5\text{x}10^{-8}\,\text{s}$ and the medium correlation time $\tau_{hyM} \approx 10^{-6}\,\text{s}$. Koenig justifies his answer with some rough calculations that a water molecule with a pair of hydrogen bonds to the protein will have a lifetime of $\approx 2\text{x}10^{-10}$s and with four bonds $\approx .8\text{x}10^{-6}$s. He calculated the lifetime of a water molecule localized by two hydrogen bonds to be $2.1\text{x}10^{-10}$ s and for four bonds to be $0.83\text{x}10^{-6}$ s which corresponds to the medium correlation time (τ_{hyM}) and the long correlation time (τ_{hyL}) respectively of his proposed "special" binding sites. Keonig postulates that water with the medium correlation time is a product of a pair of bonds to acidic side groups with each proton bound to the carboxylates while waters with the long correlation time have protons bridging two carboxylates with each proton bonded to two oxygens of a single carboxylate [*23*]. The protons with the long correlation, which comprise ~1% of the hydration layer, is the interesting item in the field range used in this experiment.

Tissue Relaxation Dispersion Models

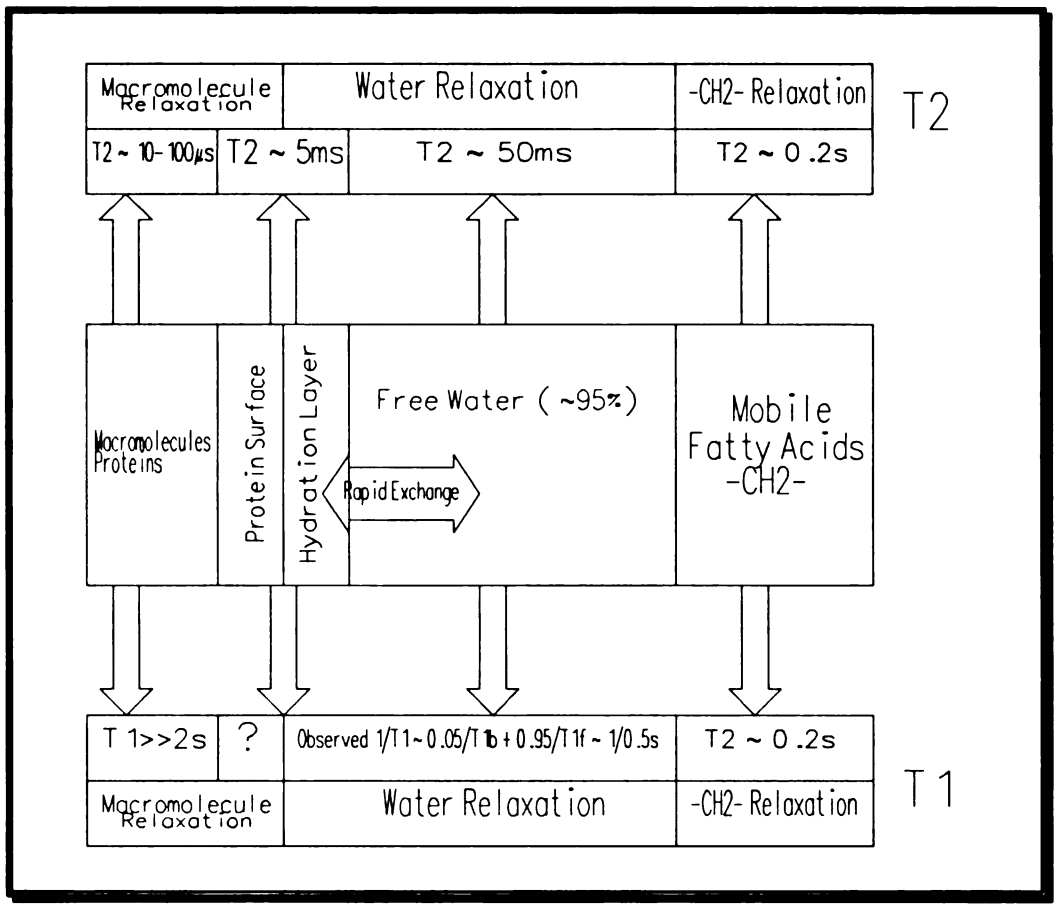

Figure 4.1
A best guess fast exchange (FE) model of tissue relaxation. Chemical differences are draw horizontally and the 5 different phases of water are represented in the center block diagram. Modes of relaxation are represented by arrows. Refer to text for more explanation.

Most models for tissue relaxation can be fitted into the diagram shown in figure 4.1 [*18*]. The protons' chemical envirnoment is represent horizontally, macromolecule, pure water, and adipose relaxation. The corresponding time scale is given in adjacent boxes. As complicated as the model seems, we can narrow the region of interest for this experiment to the left portion of the FE diagram, this is, the macromolecules protein, protein surface, hydration water, and free water

interaction. The arrows represent the mechanism affecting the corresponding relaxation. The macromolecule component is like that of a solid with very long T_1 and very short T_2. The pure water component is well understood with correlation time τ_c~1ps producing T_1 and T_2 ~3s. Neither the solid like or the free water state have a large effect on normal imaging frequencies (1-100MHz). All the action is in the surface-hydration-water interface. The water molecule is assumed to be in fast exchange (at least for FET model) between free water and the hydration layer. The term "fast" generally means much shorter than the relaxation time but longer than the correlation time.

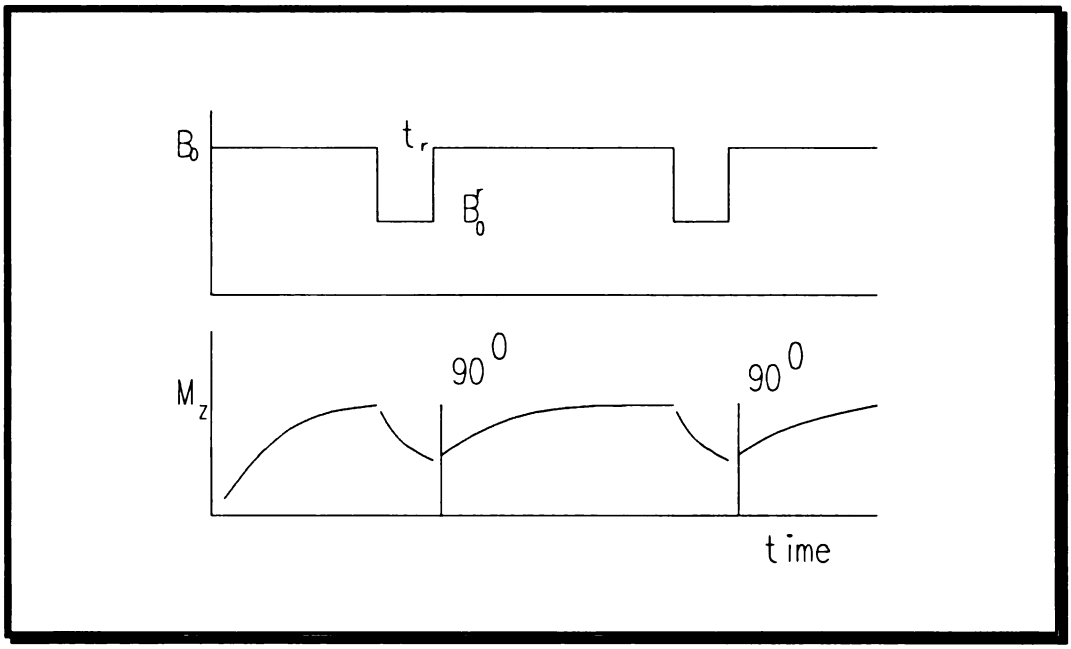

Figure 4.6
Pulse diagram of a typical relaxometer. The signal acquisition and application of the tipping pulse is done at a constant field where the instrument has a good signal to noise ratio. The sample is allowed to relax at a different field, both higher and lower fields. Sampling is done with a short delay after the application of the $\pi/2$ pulse. This delay imposes a minimum measurable T2 as discussed in the text

The mechanism of the solid-like macromolecule relaxation, as represented by the left most arrows, is the rigid lattice type dipole-dipole interaction for T_1 and T_2. The mechanism for the surface-hydration layer is local field inhomgeneities for T_2 while it is intermolecular motions and cross relaxation for T_1. The correlation time for the T_1 interaction is about 10-100ns. The third mechanism is the simple free water relaxation, with exchange diffusion the dominate term for T_2

and rapid reorientation and translation diffusion the dominant term for T_1. The correlation times for these interaction are ~10^{-5}s for T_2 and ~10^{-12}s for T_1. The forth and last mechanism is due to the mobile fatty acids, which is the primary reason for the chemical shift for adipose. This experiment addresses only the possible interactions between the free water-hydration layer-protein interactions and is represented by the items on the left side of in the model diagram.

A machine specifically design to study the NMR dispersion is called a relaxometer. Koenig and Brown [*19*], and Kimmich are the pioneers of this method. Relaxometer acquires data a fixed field where S/N is high and varies the bias during the relaxation durations. In theory, both T_1 and T_2 can be measured in this manner but only T_1 can be measured because of the extreme instrument requirements to measure T2. Figure 4.6 shows the timing diagram of a typical relaxometer which shows that it cannot measure the very fast decaying components because of instrument limitation delaying the acquiring of data until the bias field settles. This implies, from the discussion of cross relaxation, that the data Keonig acquires does not include the protons within the protein because of their short solid-like T_2 times.

Discussed in their reference is the question of whether tissue is, in terms of MRI parameters, more like a liquid or a solid. Koenig has shown the Nuclear Magnetic Resonance Dispersion profile (NMRD) of tissue has the characteristics of a solution of crossed linked (polymerized) globular proteins. The NMRD of a polymerized protein has a distinct difference that at very low fields (<10 G), the NMRD does not level off to a constant value as with a solution of globular proteins, rather the relaxation rate grows rapidly as the field decreases. In other words, tissue has a lower field dispersion in contrast to a solution of proteins, which does not have lower field dispersion. The NMRD of tissue having the distinct characteristics of a polymerized protein may not be too surprising since tissue have a solid-like structure.

A protein NMRD profile can be fitted by expression calculated from theory of dispersion and absorption of dielectrics and is given the label of its authors -- Cole-Cole [*20*]. The Cole-Cole equation is an extension of Debye's theory of dielectrics with the idea of a distribution of relaxation times and given as,

$$\varepsilon_0 - \varepsilon_\infty = \frac{(\varepsilon - \varepsilon_\infty)}{\left[1-(i\omega\tau_0)^{1-\alpha}\right]} \qquad \text{Eqn 4.4}$$

where

$\varepsilon_0 \equiv$ static dielectric constant

$\varepsilon_\infty \equiv$ "infinite frequency " dielectric constant

$\tau_0 \equiv$ generalized relaxation time

$\alpha =$ value between 0 and 1

The beauty of the Cole-Cole formulation is that when equation 4.4 is plotted on the ε" and ε' axis (imaginary and real axis) it produces a semi circle centered at $(\varepsilon_0 - \varepsilon_\infty)/2$ and below the ε' axis. For $\alpha = 0$, equation 4.4 reduces to the Debye equation which, on a Cole-Cole plot is a semi circle centered on the ε' axis. Koenig [*21*] revised equation 4.4 to fit his data and found the expression that gave the best fit was,

$$\frac{1}{T_1} = \frac{1}{T_{1,W}} + D + A\left\{\mathrm{Re}\left[\frac{1}{1+(i\nu/\nu_c)^{\beta/2}}\right]\right\} \qquad \text{Eqn 4.5}$$

where the fitting parameters are,

$T_{1,W} = T_1$ of pure Water

$D =$ asymtotic additive constant at high frequency

$A =$ Static additive constant

$\nu_c =$ frequency at the point of inflection

$\beta =$ exponential value between 0 and 1

For $\beta = 2$, equation 4.5 becomes a Lorentzian,

$$\frac{1}{T_1} = \frac{1}{T_{1,W}} + D + A\left(\frac{1}{1+(\nu/\nu_c)}\right) \qquad \text{Eqn 4.6}$$

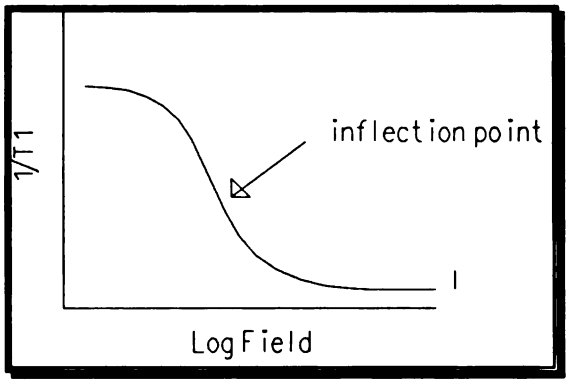

Figure 4.7

The general dispersion profile of a protein solution. It generally has an asymptotic value at very high field approaching that of free water and another asymptote at low field that is protein dependent. The interesting feature is the inflection point where Koenig has determined that it is related to the correlation time of the protein as discussed in the text.

The result of presenting equation 4.5 in this particular form is its ability to allow physical interpretation of the four fitting parameters [*22*] as depicted in figure 4.7. The asymptotic value at high frequencies is disassociated into two components, $1/T_{1,W}$ and D. The $1/T_{1,W}$ contribution is due to pure water and the D contribution is the asymptotic value due to the tissue proteins and conjectured to be caused by the interaction between the surface of the proteins and the solvent protons with some cross relaxation thrown in. The A term correlated with the molecular weight and calculations made from the two-site models using the measured A terms produce the result that the hydration layer is <1.3%. ν_c has the more interesting biophysical interpretation. From Koenig's graph [22], the inflection point of apotransferrin can be correlated to the reciprocal of rotational correlation time τ_c, using the same reasoning from Debye's use of Stoke's law. Koenig proposed that the inflection point is,

$$\nu_c \propto \frac{1}{\tau_c} = \frac{3kT}{4\pi\eta R^3} \qquad \text{Eqn 4.7}$$

where η is the microscopic viscosity, k is Boltzmann constant, and R is the macromolecule's radius. Comparing this "heuristic" fit to the motional narrowing, ($\omega_{DI}\tau_c << 1$), expression for relaxation rates,

$$\frac{1}{T_1} \approx 6(\omega_{DI})^2 \tau_c \left[\frac{0.2}{1+\omega^2\tau_c^2} + \frac{0.8}{1+4\omega^2\tau_c^2} \right] \qquad \text{Eqn 4.8}$$

may provide insights on the validity of such a fit. The bracketed terms of eqn 4.8 can be approximated by the expression

$$\left[\frac{0.2}{1+\omega^2\tau_c^2}+\frac{0.8}{1+4\omega^2\tau_c^2}\right]\approx\frac{1}{1+\left(\sqrt{3}\omega\tau_c\right)^2} \qquad \text{Eqn 4.9}$$

which gives,

$$\tau_c\approx\frac{1}{2\pi\sqrt{3}\nu_c} \qquad \text{Eqn 4.10}$$

The expression has good correlation for symmetric macromolecules and loses correlation for highly anisotropic macromolecules, producing a lower value of ν_c for anisotropic macromolecules. Fits from other macromolecules of varying size fall in the general vicinity of this value for the inflection point.

Koenig's relaxometer does not produce T_2 measurements, rather he conjectures on the functional form for T_2. Again he assumes that the dominant interaction is dipolar producing a standard form for T_2,

$$\frac{1}{T_2}\approx 6(\omega_{DI})^2\tau_c\left[3+\frac{0.5}{1+\omega^2\tau_c^2}+\frac{0.2}{1+4\omega^2\tau_c^2}\right] \qquad \text{Eqn 4.11}$$

From eqn. 4.11, the behavior of T_2 is predictable from T_1. As will be shown, the dispersion of T_2 does not follow T_1, rather it has from no dispersion to that of the opposite trend of T_1. Koenig goes on to produce a unified view of relaxation in protein and tissue [*23*] as will be discussed in the molecular dynamics section.

Bottomley has a different opinion on the relaxation dispersion functional form. He surveyed the literature for relaxation values [*24, 25*] for a large variation of tissue. An obvious problem from examining Bottomley's method is the he did not take into account anything else other than tissue type. Different equipments, different sequences, different methods or age variations were not taken into account. With this in mind , the tissues' T_1 frequency dependencies can be summarize into a basic fitting function,

$$T_1 = A\,\nu^B \qquad \text{Eqn 4.12}$$

Bottomley's fits were at higher frequencies and at a lower resolution than Keonig's data and does not take into account the inflection point of the NMRD. Bottomley's survey of the data does show the intrinsic variations between a given tissue (such as muscle) but from different animals (i.e. same species). For a single sample, such as muscle, either function can be fitted to the data very well, but with all tissue types included in the sample, the fit is not very good. The T_2 data have very large scatter and show no frequency dependencies. Bottomley does not give a physical model to justify equation 4.12 other than saying that his fit was better than what Escanye or Keonig can produce but the result is not justifiable because of Bottomley does not account for the differences in experimental procedures as described above.

Escanýe [27] experimented on cross relaxation effects of protein bound water by supercooling tissue. Supercooling allows the free water to freeze but not the protein bound water. He did this at two field strengths, 6 MHz and 90 Mhz. From the data he determined that the expression,

$$\frac{1}{T_1} = A'\,\nu^{-\frac{1}{2}} + B' \qquad \text{Eqn 4.13}$$

fit the data's frequency dependencies. Keonig agrees that tissue have a behavior very similar that given by equation 4.13. Keonig's proposed functional form is

$$\frac{1}{T_1} = A'\,\nu^{-B} \qquad \text{Eqn 4.14}$$

The real question is why the $\nu^{-\frac{1}{2}}$ or ν^{-B} dependence. Escanye rationalized that the intercept of his fitting function is the free water relaxation. He shows from his fit that the free water relaxation time is 1.7s, which agrees with the value given by Fung [*26*]. Escanýe also rationalized the dispersion functional dependence is due to multiple correlation times [27]. Plotting his multiple correlation time function vs. $\nu^{-\frac{1}{2}}$, he searched for a value of an typical correlation time that will linearize this graph. Though his approach may give some insight on the dispersion behavior of tissue, it does not have a solid fundamental foundation on which a theory can build. Therefore such a approach can only be regarded as phenomenological [27].

Fast Exchange Models

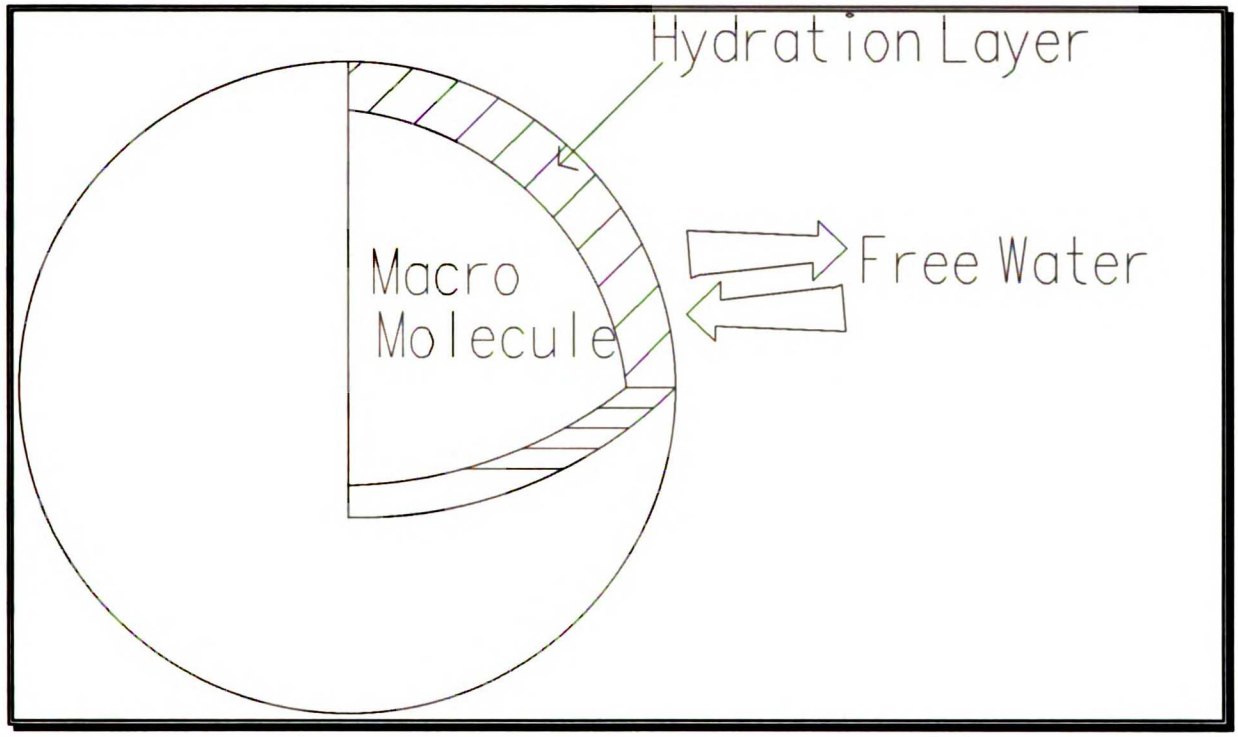

Figure 4.8
A diagram of the typical FET model. Most of the action is in the hydration layer.

Understanding the dispersion behavior of relaxation times of tissue requires the understanding of the effects that macromolecules have on water molecules. The well known result that changes in water content play a important role in changes in relaxation rates brings the notion that these changes may also play a role in dispersion effects. The two phase FE models have the hydration layer contributing the dispersion because free water does not have dispersion. Three phase FE models have the solid phase produce additional dispersion behavior.

Displayed in figure 4.1 was a generalized block diagram of a model of tissue relaxation. Displayed in figure 4.8 is a physical picture of the fast exchanged model. The picture shows three phases of water, a solid like phase bound to the macromolecule, a quasi-solid hydration layer and free water. Typically only the two outer phases are considered, the hydration layer and free water, giving the ubiquitous fast exchange two state model (FETS). Fullerton [*28*] includes the macromolecular phase, which he gives the term crystilline phase. Common to these models is the idea that

exchanges occur only between common interfaces. This is only important to models with more than two phases because the two phase models only have one interface.

Probably because of its simplicity, the fast exchange two state model (FETS) is one of the more popular relaxation models. The two states or phases of water are the free and bound state. The bound state is typically the hydration region. The T_1 relaxation for the FETS is the weighted T_1 average of the two states,

$$\frac{1}{T_1} = \frac{a}{T_{1_b}} + \frac{1-a}{T_{1_f} + \tau_b} \qquad \text{Eqn 4.15}$$

where a is percentage of water being observed, b and f represent bound and free respectively, and τ_b is the time spent in the bound compartment. The idea here is the term fast, so from the discussion of magnetization transfer presented earlier the result would be an weighted average relaxation time.

Tissue typically have ~70-80% water content. The apportionment of the water to the different phases is uncertain but is very important to quantitative models. The portion of free water constitutes ~ 75-99% depending on tissue. Applying this free water into the basic FET model, equation 4.15, and assuming that the measured value of T1 is 100ms, gives a range of relaxation values. The lower limit is (assuming that the residence time, τ_b, is short) is

$$\frac{1}{T_{1h}} \approx 100\left(\frac{1}{T_{1meas}} - \frac{.99}{T_{1f}}\right) = 100\left(\frac{1}{.3} - \frac{.99}{2.5}\right) = 960\ [1/\text{sec}] \qquad \text{Eqn 4.16}$$

and the upper limit is

$$\frac{1}{T_{1h}} \approx 4\left(\frac{1}{T_{1meas}} - \frac{.75}{T_{1f}}\right) = 4\left(\frac{1}{.3} - \frac{.75}{2.5}\right) = 12.1\ [1/\text{sec}] \qquad \text{Eqn 4.17}$$

For a measured relaxation value of 100ms, the hydration relaxation rate differs by 1.5 orders of magnitude depending on the hydration apportionment so the FET model can encompass large differences in relaxation time due to small changes in the number of hydration sites. To get a handle on the actual value of the relaxation rate of the hydration layer, various experiment have been tried to measure the hydration layer [*26,27*] with osmolarity and freezing techniques used to

determine the apportionment of water. At a temperature of ~ -6°, roughly ~90% of the water freezes. This "freezable" water is identified as the free fraction, where the remaining water produces a narrow line even below the phase transition. Other methods to determine the hydration layer are gradual dehydration by successively vacuum pumping on tissue and determining water content by direct weighing or by using modified Krebs solution with different glucose content to vary the osmotic pressure and keep the ionic strength constant. Measurements of T_h from Fung and Escnaye show a value on the order of ~.1s. This translate to a hydration of ~90%.

The FETS models do not explain the difference in relaxivity (relaxation rate per protein). The differences in relaxivity can be absorbed by the size of the hydration layer. Basically, just about anything can be attributed to the hydration layer. FET models have a difficult time in modeling dispersion. The only phase of a two state model that can have dispersion is the hydration layer. Free water does not have dispersion at low fields.

Two site models have fairly simple properties. The limiting condition is

$$R_s \le T_s \le T_{(ave)} \le R_l \le T_l \qquad \text{Eqn 4.18}$$

where

R_s = measured short relaxation time
R_l = measured long relaxation time
T_s = Short phase relaxation time
T_l = Long phase relaxation time
$T_{(ave)}$ = Average relaxation time

T_s and T_l are the relaxation times when the exchange rate is very slow relative to the relaxation times. That is, the residence time τ_s and τ_l, the short and long phases respectively, are considerably longer than the relaxation times,

$$\tau_s >> T_s \quad \text{and} \quad \tau_l >> T_l \qquad \text{Eqn 4.19}$$

will imply that the measured relaxation times will approach that of the actual relaxation time of the two phase,

$$R_s \sim T_s \quad \text{and} \quad R_l \sim T_l \qquad \text{Eqn 4.20}$$

The opposite case is when the exchange is very fast,

$$\tau_s << T_s \quad \text{and} \quad \tau_l << T_l \qquad \text{Eqn 4.21}$$

will have the measured relaxation times approaching,

$$\frac{1}{\mu_s} \sim T_{(ave)} \quad \text{and} \quad \frac{1}{\mu_l} \sim \frac{t_s t_l}{t_s + t_l} \qquad \text{Eqn 4.22}$$

Fullerton proposed a FET model and showed data to support his model [*28*]. He shows that for solutions of protein suspension the relaxation rate is proportional to the inverse of water concentration. His model has water in three phases -- free water, hydration water, and crystalline water where each of the phases has a different relaxation time. The first and last phases have the typical behavior as their name implies (assuming that the dominate mechanism is dipolar). Free water has the long relaxation times with T_1=T_2. Crystalline water has very short T_2s and long T_1s. The hydration layer is the phase where the frequency dependencies are. The expression he gets is

$$\frac{1}{T_1} = k(R_h - R_w)\left(\frac{1}{P_w} - 1\right) + R_w$$
$$\frac{1}{T_2} = \frac{1}{T_1} + f_h(R'_{2c} - nd) \qquad \text{Eqn 4.23}$$

where

R_h = relaxation rate of hydration layer
R_w = relaxation rate of free water
R'_{2c} = effective relaxation rate for crystilline water
f_h = fraction of water in the hydration phase
n = number of hydration layers
d = exchange rate decrease per hydration layer
k = proportion of hydration layer to solid solute

His data fits his model very well, but empirical parameters such as the slope of the linear dependencies need to be determined for different tissue types. His model works well for a particular tissue type and only over a limited hydration range.

Fung [*26*] also address the hydration problem. He measured dehydrated rat muscles suspended in modified Krebs solutions. He determined, by extrapolating to zero dry weight, the value of $1/T_1$

for the free fraction to be 0.6s, about twice as fast as free water. Fung attributed the shortening of T_1 to the oxygenation of water. This value for the free fraction is independent of field strength. Applying the basic FETS model, eqn. 4.15, determined the T_1 rates for the hydration layer, at 25C, were 25[1/s], 9.9[1/s], and 4.8[1/s] for 5, 30, and 100 MHz respectively. He does point out that relaxation rates may not be monotonic functions of water content because he has shown that T_1 of mouse brain decreased by 8% after homogenization, though the water and protein contents were the same. Even with constant water content and identical protein content the relaxation time decrease implies that the tissue structure has an effect on the relaxation time. Fung also notice an interesting event when the dry weight ratio of muscle reaches 3, T_1 reaches a minimum and increases for lower water content. This may be the point where the NMR signal has no contribution from free water and further dehydration decreases the thickness of the hydration layer.

The FETS models have shown not to be correct. Hallenga [*29*] experimented with proteins with a large range of molecular weights and using three nuclei, ^1H, ^2H, and ^{17}O. Any two site model can be written in the form

$$\frac{1}{T_{1measured}} = \frac{[C]}{55.6}\sum_{i=0}^{i=I}\frac{q_i}{T_{1protein}^i + \tau_d^i} + \frac{1}{T_{1w}} \qquad \text{Eqn 4.24}$$

where

$[C]$ = molar concentration of protein

q_i = number of the ith binding site

τ_d^i = lifetime of binding site

$T_{1protein}^i$ = relaxation time of the ith protein

T_{1w} = Relaxation time of water

A further simplification is typically applied, where all the binding sites are assumed equivalent. With Q as the total number of binding sites, the assumption gives,

$$\frac{1}{T_{1measured}} = \frac{[C]}{55.6}\frac{Q}{T_{1protein} + \tau_d} + \frac{1}{T_{1w}} \qquad \text{Eqn 4.25}$$

Keonig [*23*] states that the condition that the residence time of the macromolecule, τ_d, is constrained by the condition,

$$T_{1\,protein} \geq \tau_d \geq \tau_c \approx 1/10.9\,\nu_c \qquad \text{Eqn 4.26}$$

This relationship results from the arguments that the proton will not be able to sense the dynamics of the protein if τ_d is too short and the relaxation effects will be exchanged limited if τ_d is too long. With the contraints imposed by equation 4.26, experiments with lysozyme (14kD) and hemocyanin (9000kD) solutions [*30*] shows their respective τ_d values differ by more than an order of magnitude and are not compatible with typical τ_d values. Another objection to the two site model is the value of τ_d is five orders of magnitude larger than what is expected from hydrogen binding. Hydrogen binding is assumed to be the major factor for the formation of the hydration layer.

The unusually long residence time may be explained by the protons binding to polar groups on the surface of the protein, though pH dependent experiments fail to show such binding sites. The two site model should be strongly dependent on isotropic dilution because increasing the dilution will increase the relaxation. Such experiments on serum albumin solutions have shown almost no dilution effects. Hydrodynamic ordering has also been suggested but experiments again show that the protein-water interface is the important parameter since this ordering is presumably caused by hydrogen bonding to exposed polar groups and pH dependencies are not apparent. Koenig assumes that the hydration layer is ~20% of the protein volume or ~2% of the total volume. From his fit of appotrasferin he gets a value of the number of binding sites as n~13 per molecule or about ~2% of the water molecules in the hydration layer.

Cross Relaxation

The demise of the two state model leaves a question of how does the solute protein affect the solvent water relaxation rate. Cross relaxation may be the answer. The protons in protein have a relatively higher relaxation rate than that of solvent protons providing an additional relaxation pathway for the solvent protons. The picture of the cross relaxation mechanism is not very different than that of FETS models, only the names of the players are changed.

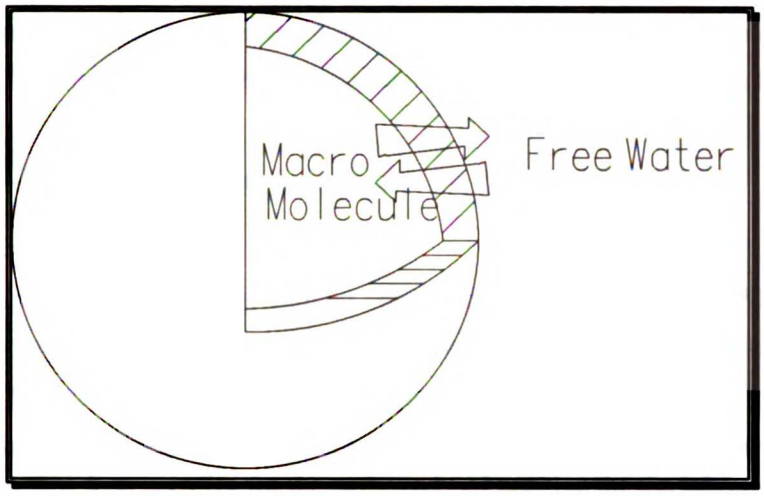

Figure 4.9
The cross relaxation model is very similar to the FET model except magnetization is transfered via spin exchanges. Spin exchange is between the proton in the interior of the protein to the solvent protons.

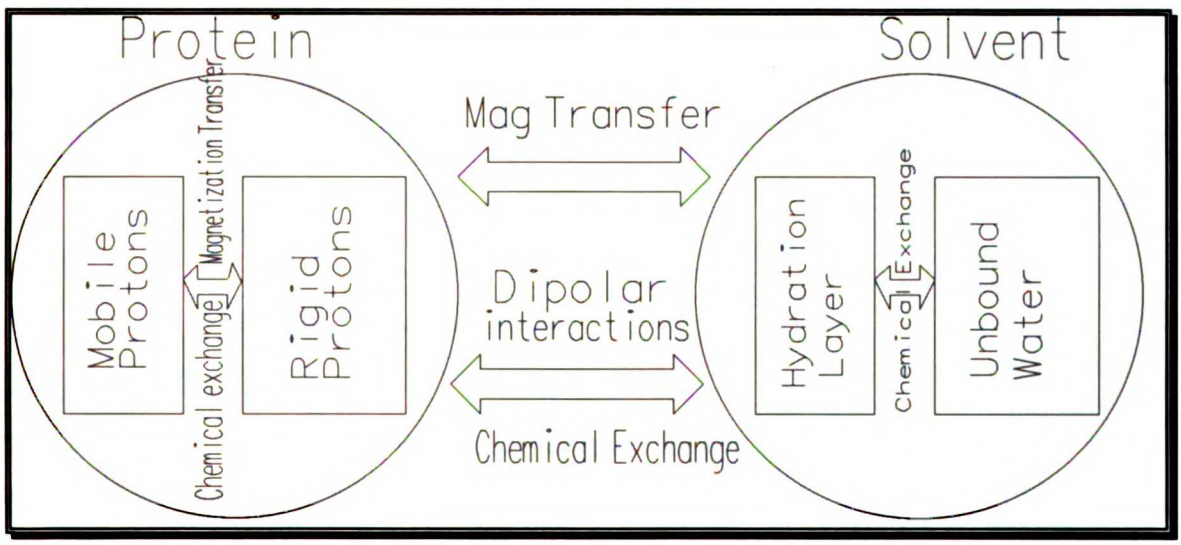

Figure 4.10
Schematic for a combined magnetization transfer and chemical exchange protein relaxation model. The discussion deals primarily with the magnetization transfer. The term magnetization transfer and cross relaxation are used interchangeably.

The model for the cross relaxation problem is presented in figure 4.5. The mobile and the "rigid" bound protons in the protein are major players in the cross relaxation picture. Magnetization and

chemical exchange can occur between the two phases and are coupled to unbound water via the hydration layer. The rate of change of magnetization in a given state, *i*, has three terms [*31*],

$$\frac{dM_i}{dt} = -R_1(M_i - M_{i\infty}) - k_{ij}(M_i - M_{i\infty}) + k_{ji}(M_j - M_{j\infty}) \qquad \text{Eqn 4.27}$$

The first is the standard rate of change without cross relaxation given by $-R_1(M_i - M_{i\infty})$, where $-R_1$ is the spin lattice relaxation rate and the minus sign is the convention of decreasing magnetization. The next two terms are the cross relaxation terms, one for the outbound magnetization transfer and one for the inbound magnetization transfer respectively. The cross relaxation rate constant k_{ij} is negative for the outbound and positive for the inbound term giving the expression for the rate of change for the magnetization. Defining a reduced magnetization m_i, will simplify the equation,

$$m_i = -\frac{M_i(t) - M_{i\infty}}{2M_{i\infty}} \qquad \text{Eqn 4.28}$$

and assuming that the inbound and outbound cross relaxation rates are equal give the rate of change for the water and protein magnetization, m_w and m_p respectively as

$$\begin{aligned} \frac{dm_w}{dt} &= -R_{1w}m_w - k_w m_w + k_p m_p \\ \frac{dm_p}{dt} &= -R_{1p}m_p - k_p m_p + k_w m_w \end{aligned} \qquad \text{Eqn 4.29}$$

The solution to the coupled differential equation begins by rewriting it into a matrix form, $\dot{\boldsymbol{m}} = \boldsymbol{A}\boldsymbol{m}$, whose general solution is $\boldsymbol{m} = e^{\boldsymbol{A}t}\boldsymbol{c}$,

$$\frac{d}{dt}\begin{bmatrix} m_w \\ m_p \end{bmatrix} = \begin{bmatrix} -\left(\frac{1}{T_{1w}} + k_w\right) & k_p \\ k_w & -\left(\frac{1}{T_{1p}} + k_p\right) \end{bmatrix}\begin{bmatrix} m_w \\ m_p \end{bmatrix} \qquad \text{Eqn 4.30}$$

where the c's are arbitrary constants. A standard procedure to determine e^{At} begins with finding the eigenvalues of the matrix A given by $\det(A - \lambda I) = 0$,

$$\det\begin{bmatrix} -\left(\frac{1}{T_{1w}}+k_w\right)-\lambda & k_p \\ k_w & -\left(\frac{1}{T_{1p}}+k_p\right)-\lambda \end{bmatrix}=0 \qquad \text{Eqn 4.31}$$

in which the following characteristic equation is obtained,

$$\lambda^2+\left(\frac{1}{T_{1w}}+k_w+\frac{1}{T_{1p}}+k_p\right)\lambda+\left(\frac{1}{T_{1w}}+k_w\right)\left(\frac{1}{T_{1p}}+k_p\right)+k_wk_p=0 \qquad \text{Eqn 4.32}$$

from which the eigenvalues via the quadratic equation, and expanding the terms under the square root sign and reducing the term gives the eigenvalues as,

$$2\lambda_{\pm}=\left(\frac{1}{T_{1w}}+k_w+\frac{1}{T_{1p}}+k_p\right)\pm\sqrt{\left(\frac{1}{T_{1w}}+k_w-\frac{1}{T_{1p}}-k_p\right)^2+4k_wk_p} \qquad \text{Eqn 4.33}$$

Which gives immediately e^{At} as,

$$\begin{aligned} e^{At} &= \alpha_1 At+\alpha_0 I \\ &= \alpha_1\begin{bmatrix} -\left(\frac{1}{T_{1w}}+k_w\right) & k_p \\ k_w & -\left(\frac{1}{T_{1p}}+k_p\right) \end{bmatrix}+\alpha_0\begin{bmatrix} 1 & 0 \\ 0 & 1 \end{bmatrix} \end{aligned} \qquad \text{Eqn 4.34}$$

The constants α_0 and α_1 are determined from knowing that

$$e^{\lambda_{\pm}}=\alpha_1\lambda_{\pm}+\alpha_0 \qquad \text{Eqn 4.35}$$

gives the constants as

$$\begin{aligned} \alpha_1 &= \frac{e^{\lambda_+ t}-e^{\lambda_- t}}{\lambda_+-\lambda_-} \\ \alpha_0 &= \frac{\lambda_- e^{\lambda_+}-\lambda_+ e^{\lambda_-}}{\lambda_+-\lambda_-} \end{aligned} \qquad \text{Eqn 4.36}$$

Replacing the constants into equation 4.34 gives,

$$\frac{1}{\lambda_+ - \lambda_-}\begin{bmatrix} -\left(\frac{1}{T_{1w}} + k_w - \lambda_-\right)e^{\lambda_+ t} - \left(\frac{1}{T_{1w}} + k_w - \lambda_+\right)e^{\lambda_-} & k_p\left(e^{\lambda_+ t} - e^{\lambda_- t}\right) \\ k_w\left(e^{\lambda_+ t} - e^{\lambda_- t}\right) & -\left(\frac{1}{T_{1p}} + k_p - \lambda_-\right)e^{\lambda_+ t} + \left(\frac{1}{T_{1p}} + k_p - \lambda_+\right)e^{\lambda_-} \end{bmatrix}$$

Eqn 4.37

producing the solution for $m(t)$,

$$m_i(t) = c_i^+ e^{-R_1^+ t} + c_i^- e^{-R_1^- t}$$ Eqn 4.38

where

$$2R_1^{\pm} = R_{1w} + R_{1p} + k_w + k_p \pm \sqrt{\left(R_{1w} - R_{1p} + k_w - k_p\right)^2 + 4k_w k_p}$$

$$c_w^{\pm} = \pm m_w(0)\frac{R_{1w} - R_1^{\mp}}{R_1^+ - R_1^-} \pm \left\{m_w(0) - m_p(0)\right\}\frac{k_w}{R_1^+ - R_1^-}$$

$$f_w k_p = f_p k_w$$

$f_{w,p}$ = fraction of protons in the water or protein phase

$$R_{1w,p} = \frac{1}{T_{1w,p}}$$

$m_i(t)$ is a sum of decaying exponential. Notice that $c_i^{\pm}$ are functions of the initial magnetizations $m_i(0)$ and $m_j(0)$. This has implications in which cross relaxation can be measured. Imaging sequences have very long pulse lengths, which at 10ms is about the same order of magnitude as the spin-spin relaxation times of tissue. This implies that an application of π pulse will flip the unbound water protons an angle π, but only a partial flip for the protein protons because of these protons have very short T_2's. The proton in the protein has a more solid-like relaxation characteristic, having a very short T_2s and relatively long T_1s has a fairly broad resonance. A pulse will flip a small fraction of the total protons and rapid spin diffusion will redistribute the spins to establish a spin temperature. The value of $m_p(0)$ is obviously less than 1. Thus, a pulse length with the condition $R_{2p}^{-1} < \tau_{pulse} << R_{2w}^{-1}$, will result in $m_p(0) < m_w(0)$ and $m_w(0) \sim 1$ with c_i^+ increasing and c_i^- decreasing. This will produce an increase in the measured relaxation rate.

The limit where the cross relaxation rate is much faster than the spin-lattice relaxation times, that is when $k_i >> R_{1i}$ and $k_j >> R_{1j}$, reduces the A matrix to

$$A = \begin{bmatrix} -k_w & k_p \\ k_w & -k_p \end{bmatrix} \qquad \text{Eqn 4.39}$$

and following the same procedure as the previous solution, (with considerably less labor) gives the relaxation rates and constants as,

$$\begin{aligned} R_1^+ &= k_w + k_p \\ R_1^- &= p_w R_{1w} + p_p R_{1p} \\ c_w^+ &= \left[m_w(0) - m_p(0)\right] p_p \\ c_w^- &= 1 - \left[m_w(0) - m_p(0)\right] p_p \end{aligned} \qquad \text{Eqn 4.40}$$

Edzes et. al. [*32*] studied cross relaxation in hydrated rat collagen where the differences in relaxation times of the two states are separable by inspection of the FID obtained from a π-t-$\pi/2$ sequence. The collagen signal decays very fast, hence acquisition must occur immediately after the pulse. The pulse length is very short (relative to typical imaging pulses) lasting about 1.5 μs with the acquisition occurring 10μs after the beginning of the pulse. Anything decaying earlier than 10 μs will not be seen. The transverse relaxation T_2^* is 16.7μs and 200μs for collagen and water respectively. The longer relaxation time is attributed to water, though this number is considerable shorter than free water. This relaxation time includes the inhomogeneity of the magnet since a straight FID was acquired. Duetrated collagen shows only the same fast relaxation time and does not show the water signal hence the conclusion that the long relaxation is due to free water. The experiments were done with the collagen along the bias field axis since collagen has been shown to show angular dependencies[*33*]. Edzes et. al. also studied cross relaxation for muscle [*34*] where the cross relaxation is present but is smaller than for collagen because muscle has a larger water content. The majority of the protein protons have about 15% of the total intensity with a short T_2~40μs. Another 7% of the signal intensity is due to a longer T_2~.5ms and is attributed to the more mobile side chains of the proteins.

Relaxometry and imaging sequencing do not acquire immediately following a transmitting pulse so the condition of a fast cross relaxation rate (i.e. $k_i, k_i >> R_{1i}$) will eliminate the R_1^+ and c_i^+ term because it will decay out well before the data acquisition starts, hence what remains for the magnetization is,

$$m_i(t) = \left\{1 - \left[m_i(0) - m_j(0)\right]p_j\right\}e^{-R_{ave}t} \qquad \text{Eqn 4.41}$$

where $R_{ave} = p_i R_{1i} + p_j R_{ij}$ is the apparent spin lattice relaxation rate. Equation 4.41 has the required characteristic that the relaxation rate is proportional to the inverse water content. In the parlance of Fullerton [*28*] and repeated here with the notation change of f for p.,

$$\begin{aligned} R_1 &= f_w R_{1w} + f_h R_{1h} \\ &= C_1\left(\frac{1}{P_w}\right) + C_2 \end{aligned} \qquad \text{Eqn 4.42}$$

The frequency dependencies attributed to the hydration layer in FETS model must include the protein protons via cross relaxation. Through cross relaxation, free water is able to "sense" the molecular dynamics of the protein. Proton relaxation in protein is mediated by cross relaxation between nitrogen and protons and cross relaxation is also the cause of the dispersion effects.

Winter and Kimmich [*35*] measured solid (i.e. dehydrated) proteins to determine the mechanism of relaxation of protons in proteins. Dry samples of BSA, Muscle, M. Luteus, and yeast yielded information showing probable separation of two proton relaxation pools. Proteins, as discussed previously, have a fairly rigid backbone. The rigidly bond backbone protons have the same correlation times as the protein itself. The free moving residues, having substantially smaller mass, have shorter correlation times. This difference in relaxation time can be seen on relaxometry data of solid and water solutions of the same proteins. The whole molecule with its backbone protons has a correlation time ~10^{-6} s while the less massive side groups have a correlation time ~10^{-9}. Unrestricted motion of the whole macromolecule occurs only for the solution and not for the solid, so the averaging effects due to the motion of the whole molecule would apply only to the solution.

Their data for BSA at fields above 10 MHz show similar relaxation characteristics. The solid and solution phases have but differ vastly at lower fields because of different effects in the two relaxation pools. Above 10 MHz, similarity between the solid and solution phases implies the mechanism at higher field is independent of the hydration of BSA, and independent of the various tumbling motions of the whole molecule. The authors proposed that the logical choice for the mechanism is the side chains that typically have correlation times of ~10^{-9} s.

At fields less than 10 MHz the dominant relaxation reservoir is from the backbone protons. These protons are bonded to either a carbon or nitrogen. The naturally occurring carbon has atomic number of 13 which is a spin 1/2 nuclei. The γ for carbon is about 1/4 of the proton's, so energy conserving relaxation requires coupling of 4 carbons per proton. This requirement is rather difficult to implement because close proximity is required for cross relaxation where the spatial dependencies are roughly $1/r^3$ and carbon in a protein has two of its four available bonds as the backbone foundation. The nitrogen is the most logical conclusion for the cross relaxation pathway and the quadrupolar dips are the prime example that this is the mechanism. From Kimmich's data, the dramatic difference of relaxation characteristics between solid and liquid BSA shows that at fields less than 10 MHz relaxation is dependent on hydration and molecular motion. Only in the liquid phase does BSA have unrestricted motion

Keonig et. al. show the cross relaxation rates for three types of proteins [*36*] by varying the dilution of proteins and measuring the corresponding "A" term in his Cole-Cole fit. A relaxometer of the type used by Keonig cannot measure the short relaxation times because of hardware limitations so only the relatively longer relaxation time is measured. He fitted his A parameters to the cross relaxation expression and concluded that cross relaxation is present.

Proton-proton cross relaxation is not the only relaxation coupling that occurs. Cross relaxation between nitrogen and protons are possible and can be observed by the fact that a spin 1 nitrogen nucleus has 3 transition frequencies and relatively independent of frequency, and will coupled to the proton relaxation at those frequencies. The proton relaxation dispersion will show some effects when the proton transition frequency equals the nitrogen's transition frequency. The details of the nitrogen-proton cross relaxation were discussed in quadrupolar section.

Chapter 5

Biological Models

Epithelium

Higher forms of life have a hierarchy of increasing structural complexity of cell-tissue-organ-system. The concern here is of the cell and tissue, with the particular interest in epithelial tissue. There are six types of epithelial cells, simple squamous, simple cuboidal, simple columnar, stratified, psuedostratified columnar, and transitional epithelium. The majority of adult cancers have an epithelial origin, and the reason why epithelial is an unanswered question. Some theories include the fact that epithelial is in contact with the external world thus subjecting it to the higher probabilities of contact with carcinogens.

The tissues imaged in this experiment are breast, skeletal muscle, and brain. We did not image breast tissue, which contains a large percentage of adipose tissue, rather we imaged an adenocarcinoma of the breast. The adenocarcinoma, as its name implies, is a cancer of an exocrine mammary cell origin, so the cells imaged are not the epithelial cells themselves rather aberrant cells. Secretory cells are generally epithelial cells, structurally asymmetric and have more of the protein producing apparatus (such as the rough endoplasmic reticulum, rough ER). Epithelial cells have a bipolar structure. The nucleus at the basal lamina side of the cell begins the synthesis of proteins by replicating the necessary RNA. After being synthesized by ribosomes, the proteins are attached to the rough ER and transported to the Golgi apparatus via the lumen of the rough ER. Exocytosis of the proteins is at the apical membrane distal to the basal lamina. Secretory

cells follow a regulated pathway where the synthesized proteins are packaged in special transport vesicles and released when triggered by an extracellar signal. The grouping of the cells form a gland and typically secrete their products into ducts. Blood vessels generally do not penetrate epithelial tissue, hence transportation of nutrition, gas, and waste occur by diffusion.

Muscle

There are three type of vertebrate muscle, skeletal, heart, and smooth muscle. The type of concern in this experiment is skeletal muscle. Skeletal muscle is very different from of an exocrine cell. A microenvironment signal during development triggers myoblasts to differentiate and fuse to form a huge multinucelated muscle cell (50μm diameter) with the nuclei immediately beneath the plasma membrane. The muscle cell consists of many long cylindrical myofibrils, some as long as the muscle cell, assembled along its axis. The myofibrils are the force generators with the application of ATP and Ca^{2+}. The myofibrils consist of repeating thick and thin filaments call sarcomeres. A sarcomere is approximately 2.5 μm in length and has dark and light bands. A dense line (Z disc) bisects the light band and separates the neighboring sarcomeres. Contraction of muscle occurs when the thick and thin filaments slide past one another shortening the sarcomere without reducing the length of either the thick or thin filaments.

The light band consists of light filaments which is composed of mainly actin, with tropmyosin and troponin complex. Actin filaments are constructed from actin monomers (G actin), creating tight uniform helical threads about 8 nm wide. Actin has a bipolar structure and mobility depends on this asymmetry. Wrapped around and along the helical structure of the actin threads is tropomyosin. Spaced at regular intervals along the actin threads are troponin complexes, with one troponin for every seven actin monomers. Tropomyosin and troponin mediate the Ca^{2+} regulation of muscle contraction.

The dark band consists of thick filaments which is composed of myosin with a pair of heads at the N terminus. Myosin is a long thread with two globular myosin heads consisting of six polypeptide chains -- a pair of each, heavy, light, and tail chains. The myosin assembles into two heavy-light-tail helical constituents and coils together producing a *coiled coil* of a paired helix. The myosin

molecules aggregate, along its axis, to form a thick filament. The head aligns itself in an orderly helical spacing.

The sarcomere is the assemblage of many thick filaments each surrounded by many light filaments. The sarcomers are connected by the Z-disc at the ends of each actin filament. Force is produced with the presence of ATP and Ca^{2+}. The exactly mechanism of motive power is still actively pursed, but the general idea is that in the presence of Ca^{2+} (release triggered by the nerves) allows the myosin head to hydrolyze an ATP and swing toward the tail end. This pulling on the actin filament will shorten the sarcomere producing muscle contraction.

Brain

The brains consist of hundreds of billions of neurons with hundreds of trillions of interconnections. 90% of the brain is glia cells. The brain contains an incredible variety of proteins. Though the brain shares the same vasculature system, the brain has its own unique protein environment. The separation between the brain and the rest of the brain is accomplished by the blood brain barrier. The brain is composed of white and gray matter. White matter contains myelinated and unmyelinated fibers, oligodenrocytes, fibrous astrocytes, and microglial cells. Gray matter contains perikaryons, mostly unmyelinated with some myelinated fibers, protoplasmic astrocytes, oligodendrocytes and microglial cells [*37*]. The primary cause for the obvious difference in appearance between the white and grey matter is the greater amount of myelination of the white fibers. The exact function of the glia cells is not definitive, but the oligodendrocytes forms the myelin sheath around the axons.

As complex the brain is, the single neuron is well studied. The neuron consists of a cell body, a long axon, and many dendrites. The neuron cellular construction is not very different from other types of cells -- lipid bilayer cell walls, the nucleus containing the same genetic materials, large amount of mitochondrias, ribosomes, smooth ER, and Golgi apparatus. The axon structure is a cylindrical process that originates at the axon hillock and typically remains unbranched until it terminates. The axon's length can be micrometers to meters. The axon can be encased in a myelin sheath (white matter) or without a sheath (grey matter). The myelin sheath is produced by the oligodendrocytes' membrane in the central nervous system and by Schwann cells' membrane in the

peripheral nervous system and contains a large amount of lipids. The cytoplasm of the glial cell is squeezed out during development leaving only the glial membrane surrounding the axon.

Cancer

Cancer is a disease where the host cells' proliferations have run amok. Normal cell proliferation is controlled by the host in ways depending on the cell type and is usually either the cell's microenvironment or its genetic expression, or both. The cancer's host has lost the ability to control the proliferation of the cancer cells. Our understanding of cancer biology is still incomplete. The epidemiology of cancer is poorly understood and the most effective cure is still radiotherapy. MRI can detect tumors, whether cancerous or benign, with relative ease. Cancers tend to have longer relaxation times relative to their cellular origins producing a brighter image with typical imaging sequences. The cause of this lengthening of relaxation times is due primarily to the extra water content of tumors but this does not account for all the increase. Biological factors such as different proteins in the vicinity or structural changes also contribute to the increase. The exact nature in which these biological factors affect the relaxation times is not known but work in relaxometry has elucidated some possible causes.

Large tumors tend to have a larger percentage of water because of the necrotic region in the center caused by the inability of nutrients to diffuse into that region. Cells less than 150μm distal to a capillary are well aerated while cells farther away will be hypoxic or anoxic. The hypoxic layer is about 1 or 2 cell layers thick. Cells beyond the hypoxic layer are depleted of oxygen giving rise to anoxic necrotic cells. The hypoxic cells are important to radiotherapy because hypoxic cells have a higher tolerance of radiation than aerated cells thus requiring a higher dose to insure non-survival of tumor cells since a single surviving tumor cell can restore the tumor. The resolution employed in this experiment was not high enough to distinguish between hypoxic and anoxic nor aerated and hypoxic but the differences between aerated and necrotic cells were easily distinguishable. The necrotic region is brighter because of the longer relaxation times, both T_1 and T_2. Relaxation times of tumors show this trend where the centers of tumors tend to have larger relaxation times, but this does not explain the larger increase in relaxation time than the increase in water content would indicate.

Relaxometry of tumor [*22*] has shown that tumor's NMRD has the same characteristics as that of homogenous tissues and of its cellular origin. An example given by Koenig is of breast cancer, where breast and fat tissue have the same NMRD characteristics while the cancerous tissue has

more "tissue-like" characteristics. These differences can be explained by the fact that breast tissue is largely adipose thus having "fat" characteristics while cancer tends to be epithelial in origin thus having "tissue" characteristics.

Cancer Biology

Cancer is a disease of abnormal cell differentiation [*38*]. Normal somatic cells have a well-defined cell cycle of asymmetric cell divisions, selective changes in gene structure and transcription, selective gene translation, and cellular differentiation directed by its microenvironment. Most cells in a multi-cellular organism have the entire genome in their DNA but only a tiny fraction is available for transcription. This selective gene expression occurs very early in life and, for some cells, is a continuing process. For example, lens cells have lost the ability to synthesize hemoglobin, myosin, etc. but retains the ability to synthesize crystallin. The cells can become determined, that is, produce changes that are self-perpetuating and are distinguishable from their progeny, well before they differentiate. The cues for cell determination and differentiation come from the microenvironment and genetic predisposition. The importance of the microenvironment was shown with epithelial stem cells that can be made immortal when removed from their original site and grown in an artificial environment, very much like tumor cells, but regain proliferation control when placed back into their natural environment. Multiple microenvironment cues tell the stem cell to stop proliferating.

Normal somatic cells divide and one of the two will differentiate to a cell that cannot reproduce itself. The remaining undifferentiated cell is the only one that can procreate itself. Cancerous cells are cells that have the differentiation process arrested, through a mutation, or lack of an environment cue, and proliferate indefinitely and unchecked.

The development of the cancer is different for different cancers. Typically, cancers with a long latency between the causal event and the onset of the disease develop in slow stages undergoing small succession of changes and involve progressive mutation and natural selection. The prodigality of the cancer follows the same process that an organism follows in the natural selection process. This process includes mutation rate, number in a population, rate of reproduction, and selective advantage. Cancers can mutate at an alarming rate where the later stage cells do not resemble the original cells. The number in a population and rate of reproduction of a tumor is not very different than the faster proliferating cells in the body such as the hair or epidermal of jejunum. The difference is the tumor does not obey the restraint that a normal cell abides by,

proliferating with abandonment. The late stage tumor cells have survived the host's most ardent defense mechanism thus having a higher selective advantage than its precursor or its progeny. Defects in the host's DNA repair process will accelerate the progression of the tumor and the enhanced mutability of the cancerous cells increases the survivability of the cells from the pressures of natural selection. Multi-drug resistance of cancer cells is correlated to the changes in karyotype with the inclusion of a multi-drug resistance (mdr1) gene [*38*] that codes for a plasma membrane bound transport ATPase that prevents the intracellular accumulation of certain lipophilic drugs by actively pumping them out.

Agents as diverse as retroviruses, x rays, chemicals, and ultraviolet light can induce cancers. The link between viruses and cancer was established in 1911 by Rous [*39*] where he determined that filtered extracts from chicken sarcomas can induce tumors in healthy chicken upon implantation. The oncogene was determined to be an RNA virus (retrovirus) acting like a tranducing phage, excising itself into the host DNA neutralizing the cell's proliferation regulation directly with a restriction point or indirectly with the regulation from terminal differentiation. Both DNA and RNA viruses can induce cancers with the necessary stable parasitic integration of the viral genome for the cancer to propagate but DNA viruses typically do not stabily incorporate their genome into the host's cells, rather they activate the host's cell into hyperactive DNA replication and using the replication machinery of the host to replicate. The ubiquitous retroviruses behave in a more clandestine manner,

Epidemiology of Cancer

Cancer is the second leading cause of death in U.S.A. and is the leading disease related death of children and young adults. The biological behavior of neoplasms can be classified into two categories, benign and malignant tumors. The structures of benign tumors are typically well differentiated similar to the tissue of origin. The growth rate of benign tumors is slowly progressive, and the mode of growth is expansive and capsulated. Metastasis is absent in benign tumors but is frequently present in malignant tumors. Cancers refer to malignant tumors. The structures of malignant tumors are poorly differentiated. The growth rate of malignant tumors is rapid, and the growth rate is expansive and not capsulated.

Most cancers are caused by a mutation in the cell's DNA sequence and less likely to be cause by an epigenetic change, though epigentic change may contribute to the progression of the disease. This change must be heritable. A single mutation is probably not enough to cause cancer. Given the probability of a mutation of 10^{-6} mutations per cell division, and 10^{16} cell divisions in a lifetime of

an individual, the number of mutations in a single lifetime is 10^{10} mutations. So from a mutation causation point of view, cancers are a rare occurrence with respect to the number of mutations. Current views are that induction of cancer is a cumulative effect, taking many sequential exposures to carcinogens for such induction. Deaths from cancer for persons under forty is less than 10 per million, increasing rapidly for older people to greater than 400 per million for persons over 65 years of age. The statistics may imply the cumulative effect of causation of cancer but it also may implicate the reduction of a person's ability to repair DNA at an older age.

The tumor *initiator* and *promoter* is another pathway of tumor progression . A tumor initiator is a carcinogen, that by itself, does not cause cancer but causes some latent genetic damage that is irreversible. Repeated application of the initiator does not promote the cancer but an application of tumor promoter may induce the tumor. This tumor promoter does, by itself, not cause cancer nor does it induce irreversible genetic damage. The application of the promotor may be many years after the initial application of the initiator and still be able to promote cancer causation. The long delay between the casual events and the onset of the disease can be 20 years or longer making the determination of casual event very difficult.

Cancers are results of the environment. A migrant from a country with a higher incidence of a particular cancer to another country with a lower incidence of the cancer will take on the pattern of the new country. This implies that the differences are due to the environment rather than to genetic factors, though genetic is a contributing factor. For example, breast cancer is mostly an environmental disease with United States women at a higher risk of contracting the disease than Japanese women. Second and third generation Japanese women have an incidence of breast cancer approaching the US. women. Among US. women, those with a sibling or mother with breast cancer has an elevated risk of contracting breast cancer.

Adenocarcinoma of the breast

Until the 1990's, cancers of the breast were the most common cancers in women. Because of increased smoking by woman, lung cancer has since overtaken breast cancer. The incidence of breast cancer is highest for women between the ages of 45-75 and is rare for women under the age of 25. As discussed in the previous passage, the increased incidence of breast cancer in second and third generation Japanese-American women, is largely an environmental factor. Heredity does have a role where the incidence of breast cancers increases by a factor of two if a female has a mother or sister with the disease.

The hormonal environment is significant in the incidence of breast cancer. It was known as long as 200 years ago that abstaining women, such as nuns, have a higher incidence of breast cancer than married women. Also breast cancers have a higher rate for single than married women, childless women who marry late, and late life lactation as compared to early life lactation. Oestogens are a suspected promoter of breast cancer though the mechanism is not understood. As discussed earlier, breast cancer has large environmental factors in addition to the hereditary factors.

Most carcinomas of the breast are of a ductal epithelium origin and, on rare occasions, from acinar epithelium. The prognosis is very dependent on whether the carcinoma is infiltrating and non-infiltrating. Carcinomas breaking thorough the basement membrane and infiltrating the connective tissue stroma have a considerable less favorable prognosis.

Brain Edema

Brain edema can be caused by many physiological insults such as trauma, meningitis, and ischemia [*40*]. Edema can be of three types, vasogenic, cellular, and interstitial. Cellular (cytotoxic) edema occurs with cerebral energy depletion induced by hypoxia, acute hypoosmolality of the plasma and extracellular fluid, and from osmotic disequilibrium. The swelling occurs in all components of the brain and has the characteristic of reduction of the extracellular fluid space due to the increased volume consumed by the edema. Hypoxia is induced by asphyxiation or by cardiac arrest and produces an osmotic gradient into the cells by the increase in intracellular osmoles. Hypoosmolality occurs with cellular dysfunction such as acute sodium depletion. Osmotic disequilibrium is the "opposite" effect where the osmostic gradient into the cells is not produced by the increased osmoles in the cell, rather by the depletion of osmolality of the plasma. Vasogenic edema is the most common form of brain edema and has the characteristics of increased brain water and sodium content, expanded extracellular space, and increased permeability of the capillary endothelial cells to macromolecules. The increased permeability is inversely proportional to the size of the macromolecule which suggest the mode of transportation is diffusive rather than bulk transport.

The protocol of inducing edema by cold injury is a well known method and the development of the edema after the insult has a delay of couple hours to a day as given by Chan et. al. [*41*]. The degradation of phospholipids is rapid with 32-52% degradation within 1 minute after the

application the cold probe and reaching 68% after 24 hours. The immediate decrease in potassium was also an indication of cellular damage. Other proteins such as polyunsaturated fatty acids, linoleic acid, and archidonic acids concentrations were increase by a factor of ~2-4. The water content of the edematous tissue is unchanged at 1 minute but increases to 7.8% after 24 hrs. The edematous fluid originates from the a circumscribed zone underlying the cortical necrotic lesion. The extravasted plasma progresses through the brain parenchyma preferentially through white matter because white matter has a lower tissue resistance to such fluid flow and the rate is a function of the hemodynamic pressure. The flow is of a bulk nature rather than of a diffusive nature hence the fluid constituents will be similar at different locations. The breakdown of the blood brain barrier may be mediated by the increase in ornithine decarboxylase (ODC) activity and by the increase in polyamine levels in the cortex [*42*]. The progression is rapid, increasing four fold in 1 minute and remaining high for about 5 minutes and gradually decreasing after 10 minutes. Another rise in ODC activity occurs at ~2-6 hours post insult and the activity does not peak until ~48 hours. At the 48 hour mark, a significant increase of putrescine (330%), spermidine (105%), and spermine (330%).

An ability to follow the resolution of brain edema is a useful tool for the radiologist. This would allow a real time assessment of the treatment plan. Bulk flow is a primary mechanism for removal of the extravasted proteins, emptying into the ventricular system. Glial cells and pericytes play an early role and macrophages are the long term players in the removal of the proteins. The removal of necrotic debris is required before major angiogenesis occurs. Macrophages do the majority of removal of the necrotic debris with the neo-vasculature aiding later in the process [*43*]. The water content of edematous tissue decreases linearly from a maximum at ~24-48 hours to normal levels at ~ 12 days. The resolution to normal water content correlates with the time when increased bordering vasculature and the glial cell uptake of extravasted proteins work in concert.

Inducing brain edema in-vivo can be quite difficult, that is, without euthaniazing the animal prematurely. The cold probe has been a standard method to induce brain edema of the vasogenic type. Creating osmotic imbalancing or ischemia are other edema producing methods but lack the precise control of location and scope that the cold probe method provides. In-vitro methods have a large repertoire of precise methods, from the brute force method of desiccant drying to creating artificial omostic solutions producing swelling or dehydration, but the very act of excision loses the correlation to physiological changes. Storage of excised tissue is also a problem that an in vivo experiment does not have.

Relaxation changes due to changes in water content for brain tissue are not very different from those found previously for tissue and protein solutions [*44*]. Longitudinal relaxation rate and transverse relaxation rate are proportional to the inverse of the water concentration for cat white and grey matter. The results for bovine white and grey matter were the same except for the transverse for white matter where the rate increase was greater than linear (i.e. concave up).

Pathological Correlations to Relaxation

The ability of MRI to produce contrast among similar tissue is remarkable. Differences in water content produce some contrast but differences in relaxation produce the major contrast especially among similar tissues. What physiological or histological changes can produce a doubling of relaxation time yet with water content increasing only ~8%? The biological discussions in the previous sections demonstrated the complexity of tissue, and finding correlations to MRI parameters are almost futile. The extraordinary increase in concentration of normally excluded proteins in brain edema is of importance to the biochemist, but trying to correlate this increase or the types of proteins to MRI parameters is extremely difficult. Of the three models used in the this experiment, muscle is the least heterogeneous yet any attempts to quantify the primary relaxation centers will probably not produce meaningful results because of our inability to separate the protein constituencies. This problem is worst for an in vivo experiment where physiological functions, such as blood perfusion, must also be considered.

A simplified solution is to approximate the relaxation centers at the surface-hydration layer. These types of model can work for macromolecule relaxation, but care must be taken in the interpretation because tissue does not contain only a single species of macromolecule rather it is a collection of different macromolecules with a dominant type representing the tissue type. Relaxation of tissue generally shows a mono-exponential behavior even with the obvious fact of the inhomogeniety of tissue contents. The observed tissue relaxation is a weighted average of ensembles of macromolecules' relaxation (possibly described by the fast exchange, FE, models). Whether two states (FETS) are enough to describe the relaxation depends on the range of hydration and tissue type.

The diagnostic ability of MRI depends on understanding the how diseased tissue changes and how these changes affect the relaxation times. We have a firmer grasp on the water content changes from disease tissue because it can be measured easily and does not change with imaging field. The

relaxation times change with imaging field. How a cellular change in a cancerous tissue effects relaxation maybe related to the different proteins it synthesizes or its mosiac cellular structure.

Cellular Membrane

Mammalians cells are encapulsulated by cellular membranes. The membranes consist of lipid bilayers where the amphilitic lipids orient themselves in a dipolar geometry. Embedded within the lipid bilayers are membrane proteins that have specific functions. The hydrophobic ends of the lipids will "attract" thus exposing the hydrophillic ends to the water solvent. This asymetric geometry occurs by entropic forces, as described in the protein section. Figure 5.1 shows the structure of a phospholipid. A typical eukaryotic cell has a variety of membranes surrounding the different structures within the cell. The structures encapsulated by membranes include the cell itself, the nucleus, the Golgi apparatus, lysomes, and mitochondrias. The major constituents of membranes are proteins, lipids and carbohydrates. The carbohydrate constituents, which are typically 10% of the total weight, occur in the form of glycolipids and glycoproteins. The ratios of proteins to lipid vary tremendously, from 20% protein for myelin to 80% protein for mitochondria [*45*].

To avoid a ghost image, MR sequences impose constraints on the chemical shift due to fat. The sequences have the frequency differences between fat and water protons at less than a pixel. These constraints will also have the membrane protons in the same pixels. Different membranes consisting of different types of lipid and protein may affect the observed relaxation times. The dynamics of a phosolipid are asymmetric. Tumbling about the long axis is considerably faster than tumbling end over end. The end over end tumbling is assumed to not be a factor since the lipid is geometrically constrained by the entropic forces. The rotation about the long axis is dependent on the type lipid and the severity of the gauche (present). Diffusion occurs primarily in the plane of the lipid bilayer. PMR spectras of unsonocated lecithin bilayers show particular charateristics [*46*]. The groups with a narrow linewidth are the choline methyl and the chain terminal methyl groups. These groups have T_1's~0.5 s and T_2's~2ms. The correlation times for methyl group rotations about the parallel axis and perpendicular axis are ~10^{-6} and 10^{-10} s respectively.

The linewidths of protons in phospholipids are known to decrease with increasing water content and increasing amount of unsaturated lipids. This implies that the transverse relaxation time will increase with increasing water content and unsaturated lipids. The linewidths of unsonicated egg yolk lecithin has a strong frequency dependency at fields above 60 MHz [*47*], increasing linearly

with increasing fields. The slope of the linewidth is dependent on the sample preparation and not simply dependent on the hydration. The lipid bilayer's linewidth dispersions have similar characteristics to the tissue's T_2 dispersions but the dependency to water content is opposite. The CH_2 contribution cannot be the dominate term because the CH_2's proton relaxation rate is considerably faster than observed in tissue and has opposite dispersion dependency on water content.

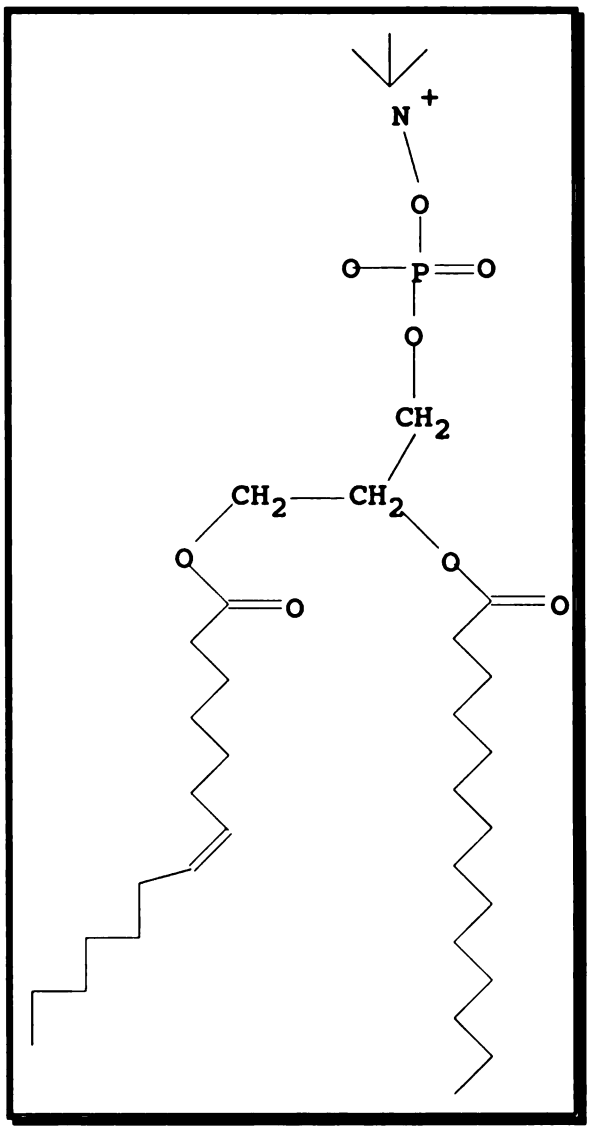

Figure 5.1
Structure of a cellular membrane phospholipid. This lipid has a trans gauche (kink). Other lipids have no gauche or a β gauche.

Chapter 6

Animal Preparation

Adenocarcinomas

Disease-free female Fischer 344 rats were inoculated subcutaneously with 1-2 mm^3 pieces of R3230AC (Biomeasure; Bogden Laboratories, Hopkinton, ME) mammary adenocarcinomas. The rat's average age at the time of inoculation is 50 days, with a typical weight of 210 grams. The tumors typically show a central necrotic region with an encapsulating sphere of "viable" tumor tissue. The tumor growth is typical, growing slowly for the first 15 days after inoculation and increasing dramatically afterwards. This is probably attributed to angiogenesis given that oxygen diffusion from a vascular capillary is typically less than 150 μm and the tumors imaged have cross sections greater than 10 mm. The tumors imaged in these experiments were adenocarcinoma of the breast implanted subcutaneously in the thigh of a female Fisher rat. Anthony Brito performed all the surgical procedures. The tumors were allowed to grow for 10-14 days after inoculation to a size of about 20mm. The tumors are encapsulated growing subcutaneously and feeding primarily from diffusion and from angiogenetic vessels. The structure is nodular and depending on the size has varying size of necrotic centers. The tumor is propagated by repeatedly implantation of a newer generation of rat using resected tumor from the previous generation.

Brain Edemas

The rats are anesthetized with pento-barbitol and an incision made to the skin and muscle immediate to the right cranial suture of young disease-free female Fischer 344 rats and reflected to expose the skull. Petroleum jelly was applied onto the exposed cranium prior to the application of the probe to improve the thermal conduction to the skull. A 36 mm^2 copper probe is dipped in

liquid nitrogen until thermal equilibrium and then placed onto the cranium. The probe is kept on the cranium for 90 seconds. The probe is then re-dipped in the liquid nitrogen to cool the probe for 2 minutes and the probe is re-applied on the cranium of the same rat. This is repeated for a total of 5 applications.

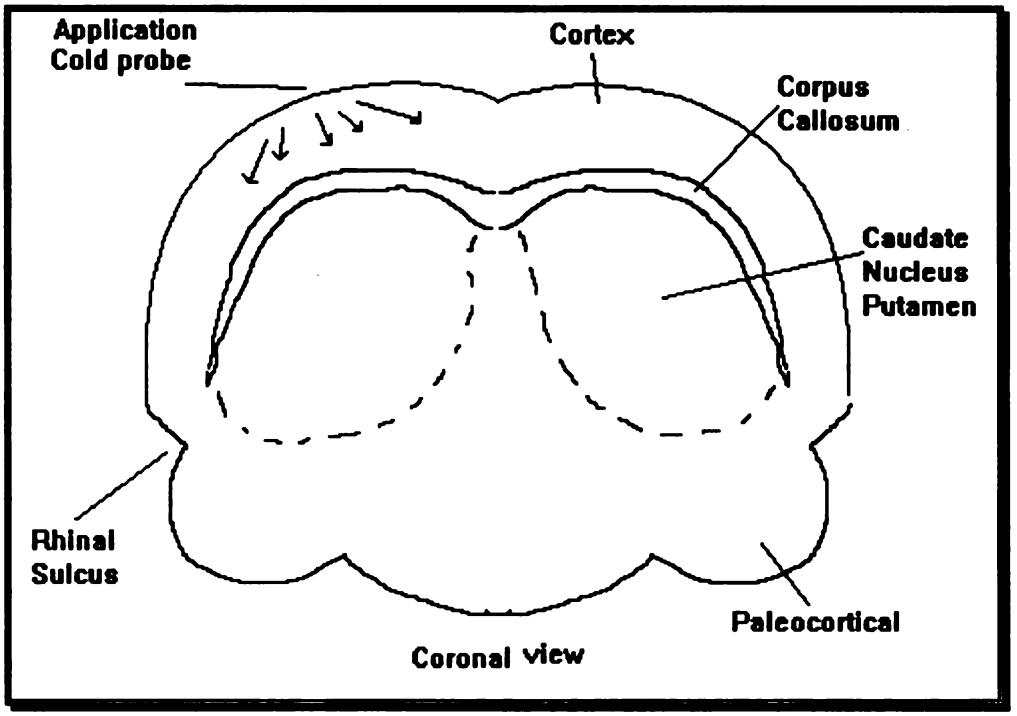

Figure 6.2
Cross sectional of a rat brain about 10mm inferior to the plane of de Groot. The edematous progression is typically along the cortex and occasionally traversing the corpus callosum. Very rarely does the edema cross the medial sagital plane.

The application of the cold probe is directly onto the skull so the drop in temperature is transferred via the skull. The edema typically is only visually evident in the cortex region but occasionally traverses the corpus callosum into the central caudate nucleus putamen of the brain. Rarely does the edema in the cortex cross the median sagittal plane and when it does, it is probably cause by the conduction of heat along the skull to the contralateral side of the cortex. The intensity of infarction is highly variable among different rats, where younger rats tend to have greater damage. The ease of inducing larger infarctions in younger rats is probably due to the younger rat having a thinner skull.

Chapter 7

Experimental Analysis

Data

Data were obtained directly from images of the tumor/hip and brain/edema. As discussed previously, four images were obtain for each rat, two TR's with two echoes. T_1, T_2, and hydrogen density were obtain for outlined regions of interest such as those displayed in figure 7.1, which is an image of the hip a normal control rat. The white penciled areas are the typical regions of interest (ROI) used to determine the MRI parameters. The number of voxels in each ROI is about ~75-100 voxels for the body images and ~50 voxels for the head images. The images have a spatial resolution of 0.8mm x 0.8mm with a slice thickness of 4 mm. Table 7.1 lists the image parameters for both the head and body scans. The errors given in all the following tables are the standard deviation of the mean.

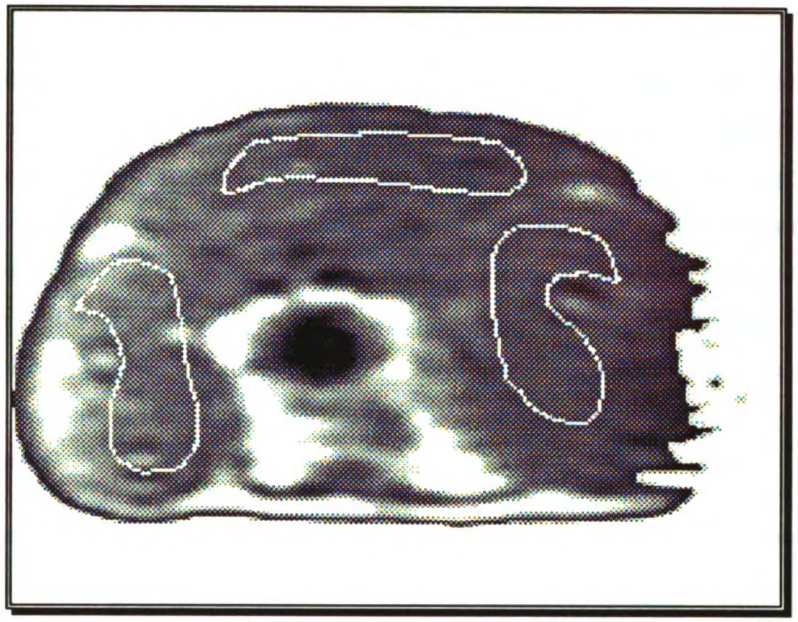

Figure 7.1

A 64x64 image of a control rat rump area. The penciled outlines are typical regions of interest (ROI) used to calculate T_1, T_2, and H density.

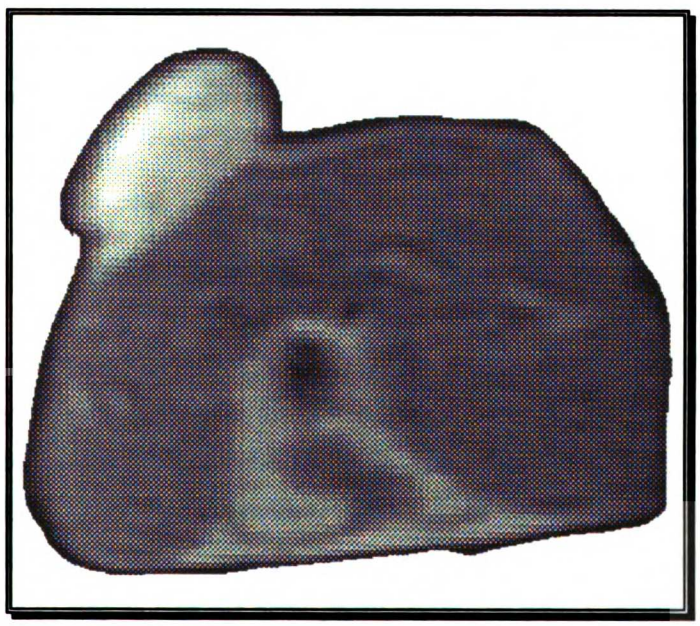

Figure 7.2

Image of rat thigh and large adenocarcinoma on the upper portion of the right flank. This image is a couple of centimeters inferior to that shown in figure 7.1. The tumor is well encapsulated, growing subcutaneously and does not invade the adjacent muscle tissue.

The tumors were positioned in the imaging coil to center the tumor in the center slice. The tumors were imaged when their size was ~20mm^2. The tumors typically have a slightly higher intensity region near the center of the tumor. This was assumed to the be the necrotic region. The tumors were not invasive and very well capsulated, staying within the subcutaneous region where implantations were made. This capusulization allowed Mr. Brito to peel the tumor away from the thigh to do the water content measurements. Angiogenesis occurs with the feeding network growing from the subcutaneous environment with mostly capillaries and occasionally small arteries. As the tumors get large, the demand for blood increases thus increasing the probability for arterial genesis.

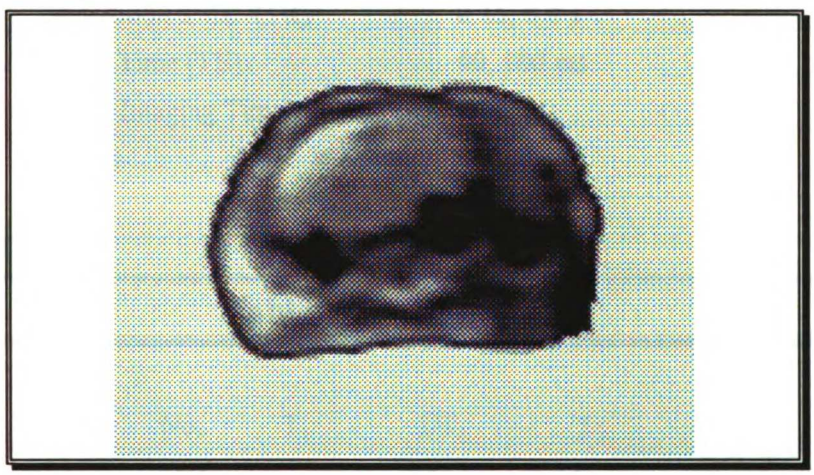

Figure 7.3
Image of a cold induced brain edema. The edema is clearly distinguishable from the rest of the normal brain on the upper left hand side of the image (actually the right side of the brain).

The brain images clearly show the edematous areas. The higher intensity of the brain edema is due mainly to the longer T_2 and increase in hydrogen density. An increase in T_1 will decrease the intensity. Hydrogen density is higher due to the increase in water content, and both T_1 and T_2 increased substantially. The edema generally stays within the cortex but on many occasions progresses beyond the cortex, past the corpus callosum, and into the caudate nucleus putamen. The edema also tends to stay within the hemisphere where the infarct occurred. Figure 7.3 is an image of an infarct of the brain, showing that the infarct is confined mainly to the cortex and to the right side of the brain. The edemas were image 24 hours post application of the cold probe to allow the edema to develop.

Table 7.1 Experimental Parmeters

Slice Selection thickness [z]	4 mm
Resolution [x,y]	.8 mm x .8 mm
Image dimensions [pixels]	64x64 pixels
Image dimensions (FOV)	33 mm
Length of $\pi/2$ pulse	10240 μs
Sampling Interval	675 μs
Sampling Window	43.2 ms
Repetition Time (TR)	0.15, 0.9 s
Echo Time (TE)	40, 100 ms
Total Imaging Time	72 min
Slices	4

Table 7.2 Viable Tumors

Field [Gauss]	No. Rats	T_1 [msec]	$1/T_1$ [1/sec]	T_2 [msec]	$1/T_2$ [1/sec]
340	15	255±8.2	3.91±0.13	122±11	8.23±0.13
386	27	278±7.9	3.60±0.10	125±7.2	7.99±0.09
478	25	276±12	3.63±0.16	147±8.2	6.82±0.08
589	25	303±8.4	3.30±0.09	128±8.6	7.81±0.09
653	50	298±6.6	3.36±0.74	134±7.5	7.49±0.07
675	25	296±7.7	3.38±0.09	115±7.2	8.69±0.10
800	25	316±5.0	3.17±0.05	118±5.1	8.44±0.06
1011	25	329±8.3	3.04±0.08	119±8.6	8.41±0.07

Table 7.3 Whole Tumors

Field [Gauss]	No. Rats	T_1 [msec]	$1/T_1$ [1/sec]	T_2 [msec]	$1/T_2$ [1/sec]	Water Content [%]	Relative Hydrogen Density [%]
340	15	257±8.3	3.89±.13	135±10	7.38±.57	82.2±0.37	105±8.0
386	27	287±7.6	3.48±.09	136±8.8	7.34±.47	81.2±0.35	133±5.8
478	25	291±7.0	3.43±.08	152±7.5	6.56±.32	82.4±0.44	122±5.3
589	25	306±8.2	3.27±.09	136±8.7	7.37±.47	83.1±0.34	123±7.3
653	50	306±6.7	3.27±.07	141±7.4	7.10±.37	81.1±0.24	115±8.7
675	25	301±8.7	3.32±.09	118±6.9	8.49±.49	81.1±0.41	125±7.1
800	25	330±6.3	3.03±.06	131±5.0	7.62±.29	81.2±0.42	116±6.6
1011	25	337±8.3	2.96±.07	121±7.5	8.25±.51	81.3±0.47	129±6.8

Table 7.4 Muscle

Field [Gauss]	No Rats	T_1 [msec]	$1/T_1$ [1/sec]	T_2 [msec]	$1/T_2$ [1/sec]	Water content [%]
340	15	144±6.0	6.93±.03	47.9±2.0	20.86±0.87	72.5±0.42
386	27	154±3.7	6.50±0.15	43.2±1.9	23.16±0.98	72.2±0.25
478	25	143±2.6	6.98±0.12	43.2±1.5	23.16±0.81	72.0±0.29
589	25	154±3.1	6.49±0.13	38.5±1.3	25.99±0.86	72.0±0.25
653	50	141±1.9	7.09±0.10	40.0±1.3	24.98±0.78	72.6±0.16
675	25	141±3.0	7.09±0.15	36.9±1.1	27.16±0.79	72.4±0.23
800	25	179±3.5	5.59±0.11	38.5±1.3	26.06±0.89	72.4±0.32
1011	25	201±6.3	4.99±0.16	38.6±1.5	25.91±1.0	72.3±0.27

Table 7.5 Contralateral Normal Brain

Field [Gauss]	No Rats	T_1 [msec]	$1/T_1$ [1/sec]	T_2 [msec]	$1/T_2$ [1/sec]	Water content [%]
340	25	254±11	3.94±.10	93.8±1.0	10.66±.19	78.78±.12
386	25	245±6.7	4.09±.09	82.5±1.7	12.12±.28	79.09±.13
478	25	246±4.6	4.06±.06	84.5±1.2	11.83±.19	78.97±.12
589	25	237±3.3	4.23±.05	74.1±0.7	13.50±.17	78.53±.11
653	25	235±2.7	4.26±.04	75.2±0.6	13.30±.15	78.52±.08
675	25	231±2.3	4.33±.03	70.9±0.6	14.10±.16	78.54±.13
800	25	260±2.1	3.85±.03	75.1±0.6	13.32±.12	78.19±.12
1011	25	279±2.0	3.58±.02	73.1±0.5	13.68±.02	78.22±.13

Table 7.6 Edematous Brain

Field [Gauss]	No Rats	T_1 [msec]	$1/T_1$ [1/sec]	T_2 [msec]	$1/T_2$ [1/sec]	Water content [%]
340	25	325±15	3.08±.14	115±3.2	8.66±.24	84.1±.19
386	25	317±9.0	3.15±.09	122±3.1	8.19±.21	84.5±.32
478	25	310±6.2	3.22±.06	121±2.2	8.28±.15	84.1±.20
589	25	294±4.6	3.40±.05	104±1.6	9.62±.15	84.8±.22
653	25	306±3.7	3.27±.04	107±1.3	9.39±.12	84.5±.22
675	25	317±3.1	3.15±.03	106±1.2	9.44±.10	84.7±.21
800	25	323±2.8	3.09±.03	101±1.1	9.91±.10	84.8±.17
1011	25	364±2.9	2.75±.02	106±1.0	9.45±.09	84.0±.18

Table 7.7 Calibration of Body Coil

Field	Location of Tumor loc	Left leg	Back
340	1.13	0.86	1
386	1.48	1.08	1
478	1.56	1.05	1
589	1.33	0.99	1
653	1.30	0.87	1
675	1.58	1.22	1
800	1.88	1.01	1
1011	1.64	1.23	1
Ave	1.49±0.23	1.04±.14	1

Table 7.7 shows the homogeneity calibration for the body coil. At each field 4 or 5 normal rats where imaged and hydrogen density of muscle was measured for the typical locations where the tumors, leg, and back muscles would be. The data is normalized to the back muscle location. The average at each field were used to calibrate the measured image hydrogen density .

Table 7.8 Head coil calibration

Field	Edema	Lower Left	Normal Right
340	1.12	1.00	1
386	1.13	1.08	1
478	1.15	1.11	1
589	1.07	1.07	1
653	1.09	1.07	1
675	1.13	1.07	1
800	1.14	1.05	1
1011	1.09	1.06	1
Ave	1.12±.03	1.06±.03	1

Table 7.8 shows the homogeneity calibration for the head coil. Each field has 4 or 5 normal rats brains imaged. Hydrogen density was measured on the normal brain at locations typical of the locations of edematous, and normal brain tissue. The average at each field was used to calibration the measured hydrogen density for rat brain.

Table 7.9 Water Content of Muscle and Tumor

	Muscle		Tumor	
Field	Weight Percentage	Hydrogen Density	Weight percentage	Hydrogen Density
340	72.5±0.4	1	82.2±0.4	105±8.0
386	72.2±0.3	1	81.2±0.4	133±5.8
478	72.0±0.3	1	82.4±0.4	122±5.3
589	72.0±.03	1	83.1±0.3	123±7.3
653	72.2±0.2	1	81.6±0.2	115±8.7
675	72.4±0.2	1	81.1±0.4	125±7.1
800	72.4±0.3	1	81.2±0.4	116±6.6
1011	72.3±0.3	1	81.3±0.5	129±6.8
Ave	72.3±0.06	1	81.8±0.24	121±3.2

Table 7.9 shows the average water content of muscle and tumor at different fields. The deviation for muscle is small, showing that the water content of muscle is consistent among the different sets of rats. The tumors have a much larger deviation showing that the tumors' water content has dependencies that vary among the different sets of rats. The water content difference is about 9%. The hydrogen densities were obtained from the MR images and normalized relative to the muscle.

Table 7.10 Table of Water Content for Normal and Edematous Brain

Field	Edema Water content	Edema Hydrogen Density	Normal Edema side Water Content	Normal Edema side Hy Density	Normal Contralateral Water Content
340	84.1±0.2	106±4.5	79.3±0.2	114±8.7	78.8±0.1
386	84.5±0.3	107±3.6	79.6±0.1	104±3.0	79.1±0.1
478	84.8±0.2	109±2.6	78.5±0.1	106±2.6	78.5±0.1
589	84.1±0.2	103±7.1	78.8±0.2	98.1±4.6	79.0±0.1
653	84.5±0.2	102±5.5	78.3±0.1	101±4.0	78.5±0.1
675	84.7±0.2	98±3.3	78.6±0.2	98±2.7	78.5±0.1
800	84.7±0.2	105±5.5	78.1±0.2	102±5.15	78.2±0.1
1011	84.0±0.2	105±3.6	78.3±0.2	101±3.2	78.2±0.1
Ave*	84.5±0.32	104±3.6	78.6±0.52	101±2.9	78.6±0.34

*The average does not include the 340 Gauss values because the normalization factor is more than three standard deviations of the typical point.

Table 7.10 shows the water content and the corresponding hydrogen density measurement of rat edematous and normal brain. The water content of the edematous brain was determined by excision and drying. Normal brain has two portions to serve as controls. Normal brain on the same side and anterior to the lesion, and the hemispheres contralateral to the lesions are used for controls. The water content difference between the edematous and normal brain is about %6.

Longitudinal Relaxation: N^{14} Cross Relaxation and dipolar relaxation

Muscle and Adenocarcinomas

Muscle and adenocarcinomas are very different pathologically but will be discussed together because the data were obtain from the same image sections. Tables 7.2, 7.3, 7.4 show relaxation data for "viable" tumor, whole tumor, and muscle respectively. The "viable" tumor is the outer portion of the tumor where necrosis is not apparent. The uncertainties represent a single standard deviation of the mean. The number of rats were typically 25 or greater with the exception of 340

Gauss. The "viable" portion of the tumor is defined as the outer perimeter of the tumor surrounding the necrotic center. This was done to compare the effect of the larger water content of the necrotic center and compare the effects of hypoxia. The water content measurements were done for the whole tumor and were not separated into viable and necrotic sections. Comparisons of the viable and whole tumors show the obvious trend of water content dependencies of MRI parameters. T_1, T_2 were slightly longer for whole tumors and H density is slightly higher for whole tumors. Because water content measurements were done with only whole tumors, all tumor data will represent whole tumors for proper comparison. Figure 7.1 shows the relationship between the T_1 relaxation time of viable and whole tumors. Notice that the dispersion is identical for both tumors with the whole tumors having a longer T_1 because of the whole tumors' higher water content. Comparison of T_2 and H density for the tumors yields the same general behavior as that of T_1.

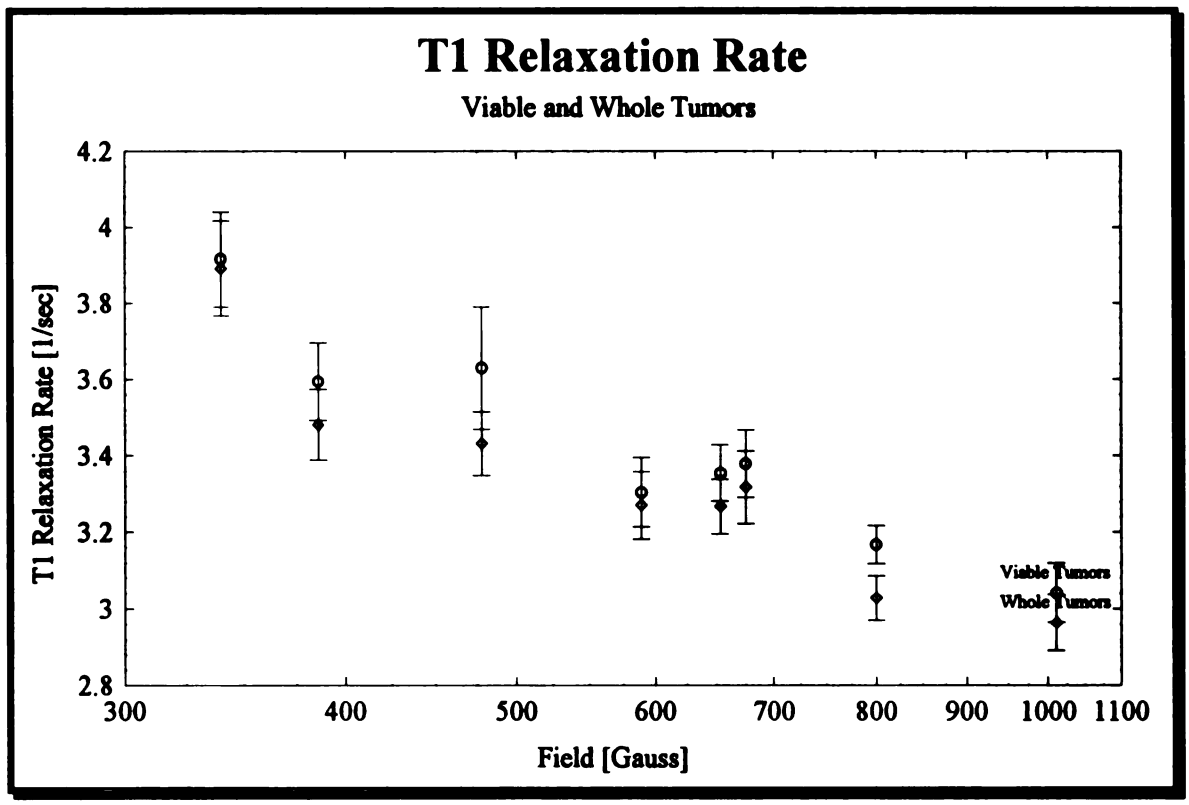

Figure 7.1

Graph of 1/T1 for the "viable" and whole tumors as described in the text. The dispersion behavior for either type is the same with the whole tumors having a slightly longer T1. This follows logically from the fact that the whole tumors have a necrotic center which contains more water.

Figure 7.2 shows the longitudinal relaxation rate dispersion obtained for muscle and tumors. The error bars represent one standard deviation of the mean for the set of 25 rats (except for 340 and 653 G which have 14 and 50 rats respectively). The rate for muscle is about twice as fast as the tumors over most of the range measured. The nitrogen induced peaks are obvious in the muscle data at 653 and 489 Gauss, but are not obvious in the tumor data. Tumor data has remote resemblance to the nitrogen peaks at 489 and 653 but are not statistically significant. The $1/T_1$ dispersions for the two tissues have very similar power montonic decreasing trends, differing by their amplitude and correlation times.

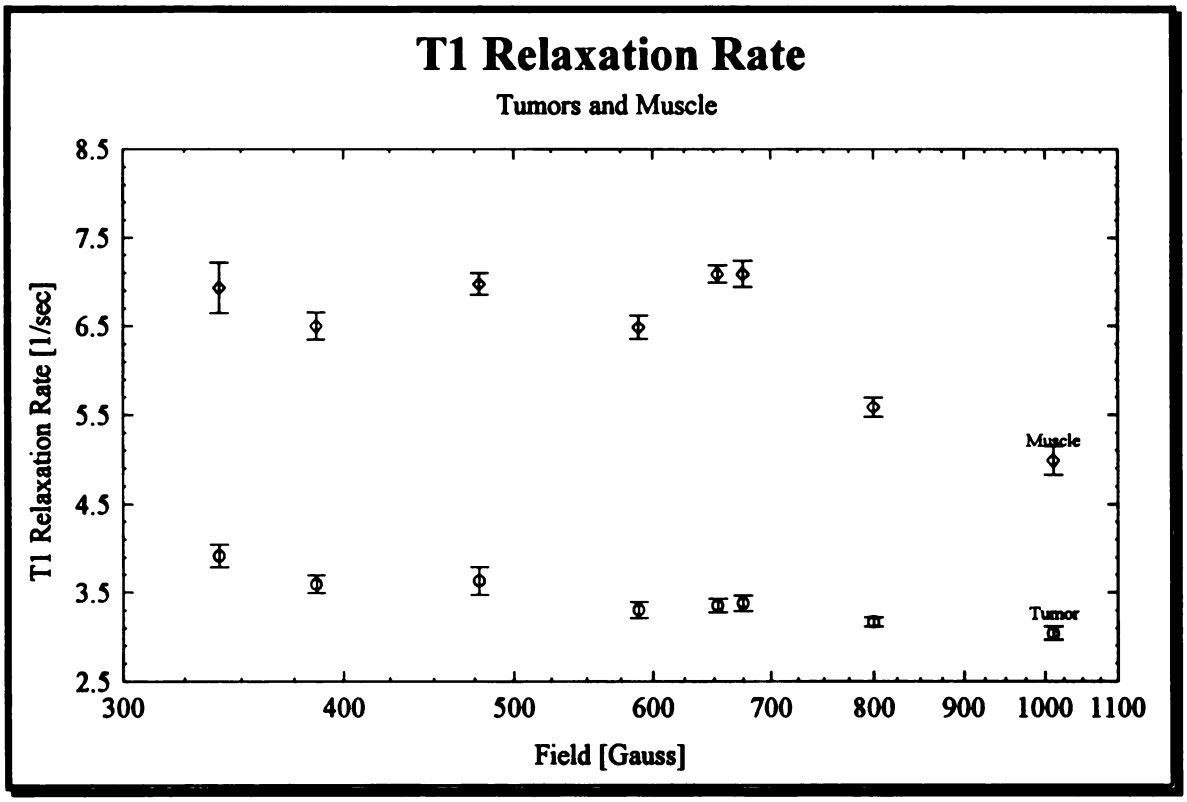

Figure 7.2
Relaxation rates for muscle and adenocarcinoma of the breast. The cross relaxation peaks can be seen at 475 and 653 Gauss in the muscles NMRD but not in the tumor NMRD.

Figure 7.3 shows a χ^2 fit to the equation $1/T_1 = a\omega^{-1/2} + b$ as done by Escanýe. The fit is good with a reduced χ^2 of .72 and 1.5 for tumors and muscle, respectively. All eight field points were used in fitting the tumor data but only four were used for muscle. Only the two low fields and two high field points were used to establish a baseline for the muscle dispersion. The increase in proton

relaxation due to ^{14}N cross relaxation is about 17% at 489G and 20% at 653G which is what generally is seen for muscle.

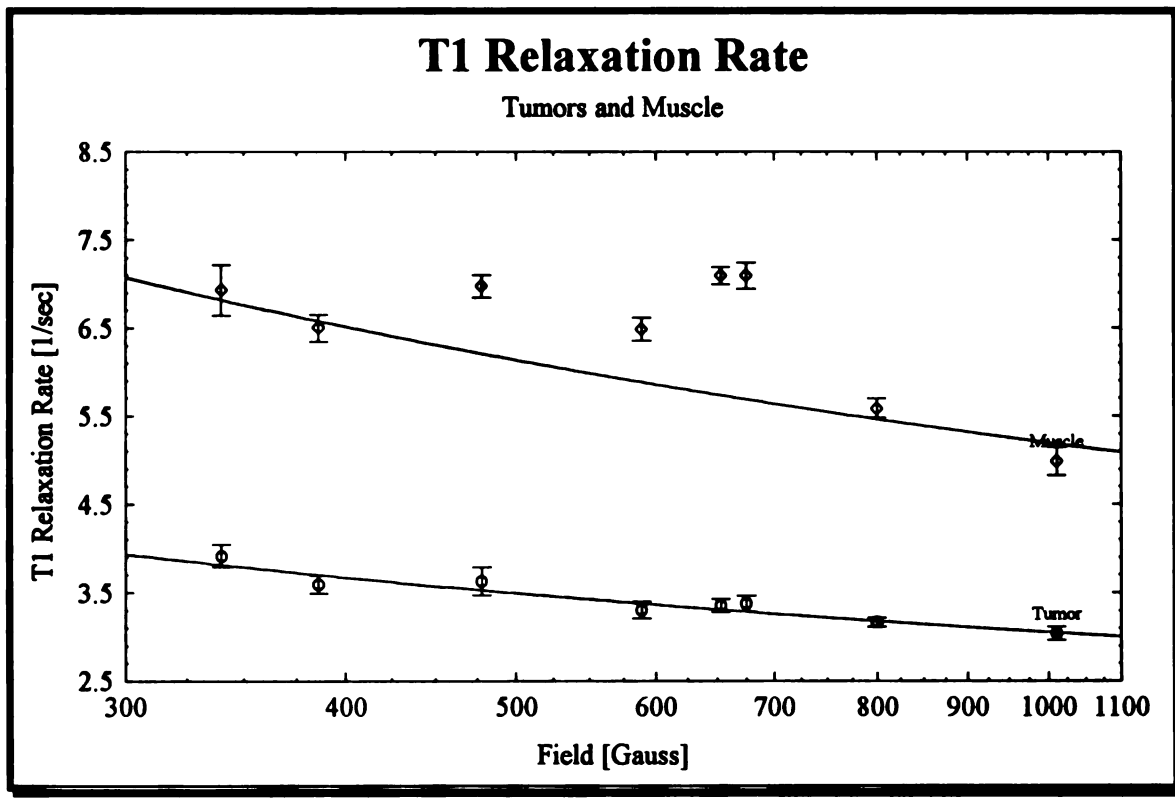

Figure 7.3

Tumor and muscle 1/T1 NMRD. The curves plotted are χ^2 fit to $y = a\omega^{-1/2} + b$. The tumor plot used all 8 points while the muscle used 5 points excluding 478G, 653G, and 675G to produce a baseline for comparison of the N^{14} peaks.

The data for muscles clearly show the cross relaxation of proton to the nitrogen in the form of peaks. The peaks represent the increase in relaxation rate at the crossing frequencies. The other pronounced feature of the data is that tumors do not show the nitrogen peaks. The current belief is that the peaks are present in all tissue (since cross relaxation is present in all tissue), and the solid-like structure of the tissue is the determining factor for their magnitude. The meaning of "solid" in a context of tissue does not have a clear definition. All tissue is "wet", consisting of roughly 75% water by weight. Solid in a relaxation sense can be defined in a relaxation context by the correlation time. Quadrupolar cross relaxation requires that the quadrupolar correlation time needs

to be relatively long ($\omega_q \tau_c > 1$). For a Larmor frequency of 2.78 MHz (653 G), the corresponding correlation time for a freely moving protein solute is constrained by,

$$\tau_c > \frac{1}{\omega_q} = \frac{1}{2(\pi)2.78\text{MHz}} = 57\text{ns} \qquad \text{Eqn 7.1}$$

Assuming the standard Debye relation for correlation time, with the viscosity of water at 37°C as 0.6915cp, this translates to a volume of,

$$V > \frac{\tau_c kT}{\eta} = \frac{57\text{x}10^{-9} \cdot 1.38\text{x}10^{-23} \cdot 310}{0.006916 \cdot} = 3.53\text{x}10^{-26}\,\text{m}^3 \qquad \text{Eqn 7.2}$$

which translates to a radius of 20Å. Easily fulfilled by a macromolecule. Muscle as describe in the previous section is long fibrils with a rotational head that provides the power stroke. The most probable motion is random tumbling of the myosin head since most of the muscle is stationary except for the sliding of the myofibrils. The myosin head has a molecular weight of 510 kDa. The rotation correlation frequency (taken from Fig. 2 of ref [23]) is 0.05 MHz. Koenig proposed that the correlation frequency and correlation time are related by $\nu_c = \left(1/_{2\pi\sqrt{3}}\right)\tau_c$, giving the rather long correlation time for the myosin head as

$$\tau_c = \frac{1}{10.9(0.08\text{MHz})} = 1.83\text{ms} \qquad \text{Eqn 7.3}$$

Considerably longer than the minimum required for the quadrupolar cross relaxation to occur. Since muscle has such relatively long correlation time, the requirement for quadrupolar cross relaxation may be more severe than given previously in the quadrupolar section.

Figure 7.4 is a Lorentzian fit to the muscle data.

$$\frac{1}{T_1} = A\left(\frac{\tau_c}{1+(\nu\tau_c)^2}\right) + C \qquad \text{Eqn 7.4}$$

Again, the fit uses only the same four data points. The fitted *dipolar* equation resulted with the parameters A = 455 MHz, τ_c = 14 ns, and C = 0.5 Hz. This correlation time is very short, considerably shorter than the earlier estimate of 1.8ms. The profile of tissue is known not to follow a Lorentzian fit, rather a power type function usually has a better fit. Why a power type function

is not answered but is rationalized. For a comparison, both a $1/T_1 = A\,\omega^B$ and a Lorentz fitting were done. A and B were the fitting parameters for the power law expression. Both can be fitted to the data fairly well because of the limited number of data points with 5 fitting parameters.

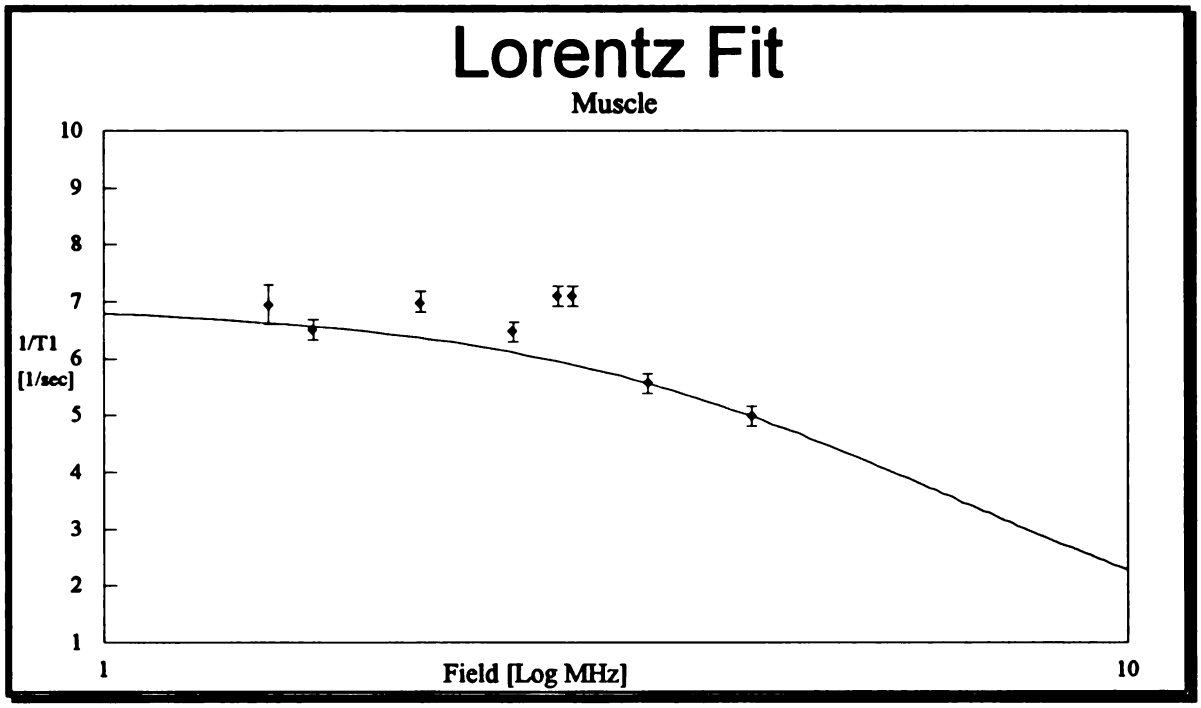

Figure 7.4
Graph of a Lorentz fit to the muscle T1 data. The fit includes only four points, the two low fields and two at high field. The four mid field points were not used so a baseline can be fitted without the contamination from the quadrupolar terms. Tumor and muscle T1 NMRD. The curves plotted are χ^2 fit to the equation $y = A[1/1+(\frac{\omega}{B})^2]+C$. The tumor plot used all 8 points while the muscle used 4 points excluding 478G, 589G, 653G, and 675G to produce a baseline for comparison of the N^{14} peaks.

The functional form found to be most useful is the inverse power form,

$$\frac{1}{T_1} = \frac{A}{\omega^B} \qquad \text{Eqn 7.5}$$

where A and B are fitting parameters. Figure 7.5 is a χ^2 to the muscle data using equation 7.5 with only four data points. Only the 340, 389, 800, and 1011 Gauss points were used to calculate

a baseline without a bias due to the quadrupolar component. The resulting fitting parameters were A=7.4 and B=0.25.

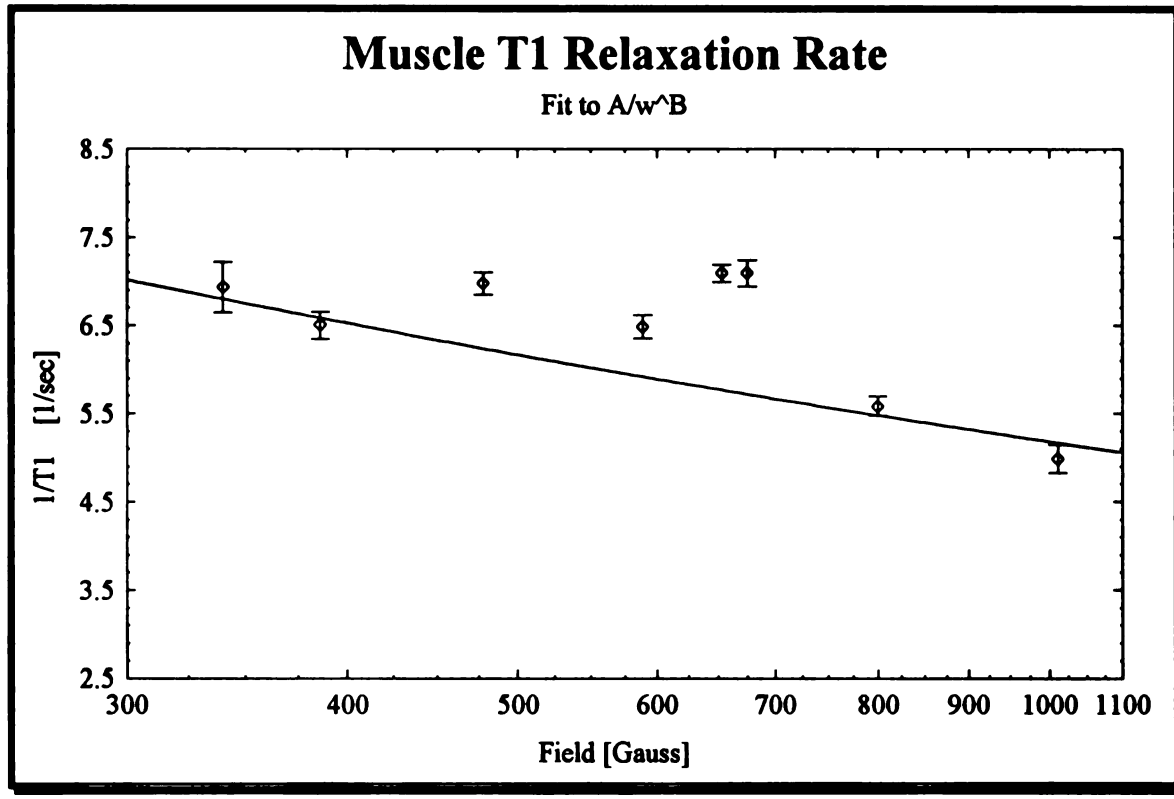

Figure 7.5

χ^2 fit to $\frac{1}{T_1} = \frac{A}{\omega^B}$ for muscle using only the two lowest and two highest field points to obtain a baseline for the dipolar contribution.

With the dipolar baseline known, the quadrupolar terms can be extracted from the data. From the previous quadrupolar section, the fit equation for the quadrupolar term is

$$\frac{1}{T_1} = \frac{\mu_0 \gamma_I \gamma_S \hbar^2}{12\pi r_{IS}^3} \left\{ \begin{array}{c} \frac{1}{2}\left(\frac{2}{3} + \sin^2\theta_S\right)[j(\omega_1 - \omega_I) + j(\omega_1 + \omega_I) \\ + j(\omega_2 - \omega_I) + j(\omega_2 + \omega_I)] \\ + \left(\frac{4}{3} - \sin^2\theta_S\right)[j(\omega_3 - \omega_I) + j(\omega_3 + \omega_I)] \end{array} \right\} \quad \text{Eqn 7.6}$$

This function behavior depends on the correlation times as described in figure 2.5, where to get a pair of peaks requires that $\omega\tau_c \sim 1$. From figure 7.2, the two visible ^{14}N cross relaxation peaks are at 675±25 and 478±25 Gauss, where the uncertainty given is a visual guess at what the true uncertainty is. The muscle shows a pair of peaks, implying that the quadrupolar asymmetry factor is greater than zero. From the quadrupolar discussion, either the quadrupolar or the asymmetry coupling constant can be determined if two of the three cross relaxation points are known. Calculating these values begins with taking the ratios of the peak frequencies,

$$\frac{\omega_2}{\omega_1} = \frac{(3-\eta)}{(3+\eta)} \qquad \text{Eqn 7.7}$$

which give the asymmetry constant for muscle as,

$$\eta = \frac{3\left(\frac{675}{478}-1\right)}{\frac{675}{478}+1} = 0.513 \pm .05 \qquad \text{Eqn 7.8}$$

From this we get the quadrupolar coupling constant as,

$$\frac{e^2qQ}{\hbar} = \frac{4K}{\hbar} = \frac{4\omega_2}{(3+\eta)} = \frac{4\cdot 2.89\text{MHz}}{(3.513)} \qquad \text{Eqn 7.9}$$
$$= 3.29 \pm .09 \text{ MHz}$$

From the K value and $\gamma_S = 3.075\text{MHz}\cdot\text{T}^{-1}$, the low field condition becomes,

$$B_0 << \frac{4K}{\hbar\gamma_s} \sim 1.07\text{T} \qquad \text{Eqn 7.10}$$

Thus the low field requirement is easily met. The three transition quadrupolar frequencies for muscle are easily determined as,

$$\omega_1 = 2.038 \text{ MHz}$$
$$\omega_2 = 2.87 \text{ MHz}$$
$$\omega_3 = \frac{2K}{\hbar}\eta = \frac{3.29}{2}(.513)$$
$$= 0.86 \text{ MHz}$$

where ω_1, and ω_2 were read directly from the graph and ω_3 calculated. With these given values of the quadrupolar transitional frequencies, and assuming a standard form for $j(\omega)$, a fit to the muscle data was done. Figure 7.6 is the result of the fit separating the two contributing components. The top curve is the power law component and the bottom curve is the quadrupolar component. The parameters for the quadrupolar terms are, τ_c = 523μs, D = 0.255 MHz, and θ = 1.6 rads.

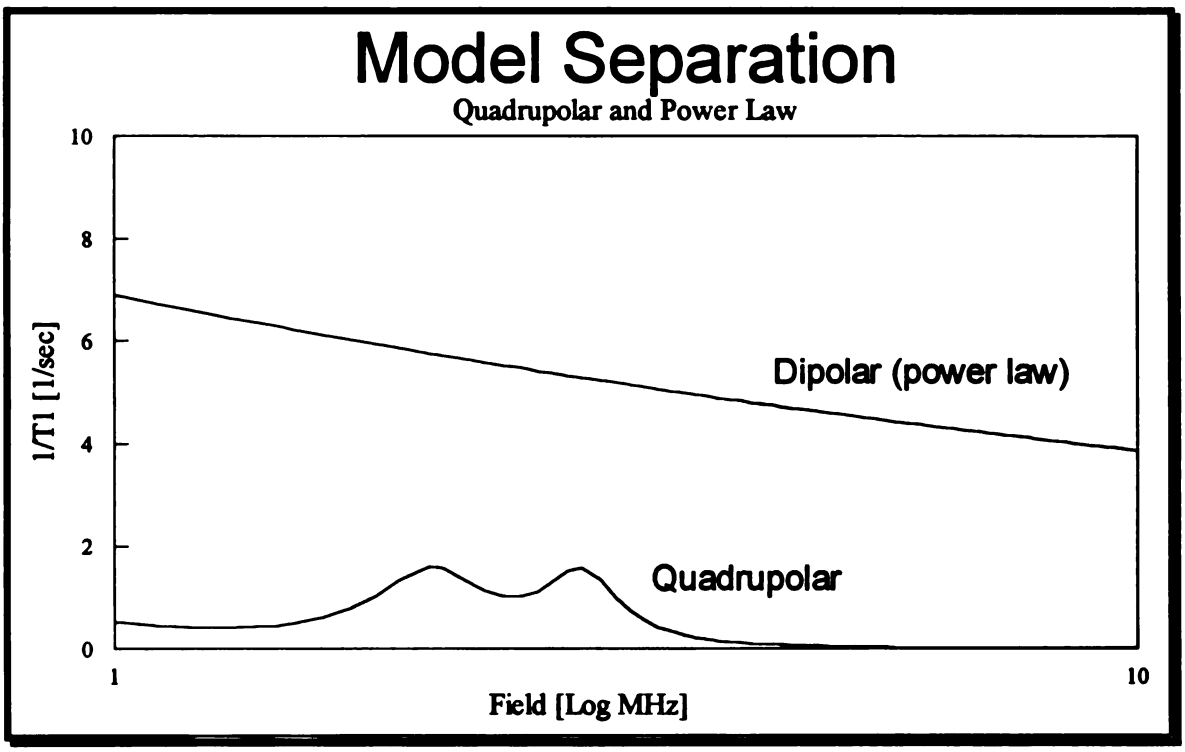

Figure 7.6

Graph showing the two models' dispersion behaviors. The graph shows the shape and amplitude of both models used in fitting the data to produce figure 7.7. The dipolar relaxation is an order of magnitude larger than the quadrupolar relaxation. From the previous quadrupolar section, the number of peaks depends on the correlation and the angle θ. Muscle has been seen to have a third low field peak. The power law has a similar separation.

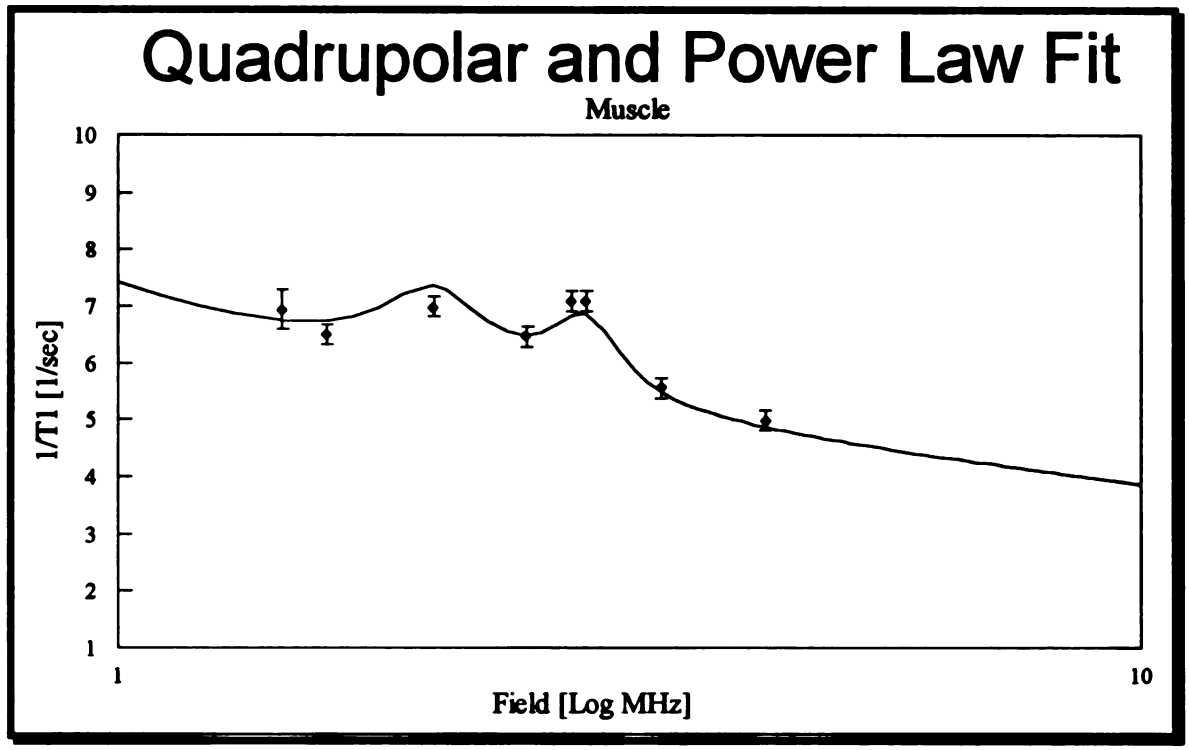

Figure 7.7
Fit of muscle data to a sum of a quadrupolar and power law fit. The Lorentzian fitting parameters are A=6.9 MHz, and B=0.252. The quadrupolar fitting parameters are τ_c= 523 μs, D=.255 MHz and 1.6 rad, using the quadrupolar transition frequencies extracted from the data, ω_1=2.0 MHz, ω_2=2.87 MHz, and ω_3=0.859 MHz.

Figure 7.7 has the sum of both, the quadrupolar and power law fit, plotted with the muscle data. Care must be given in any model fit, especially in this case because the muscle fit may have marginal statistical significance since there were only 8 points and 5 fitting parameters.

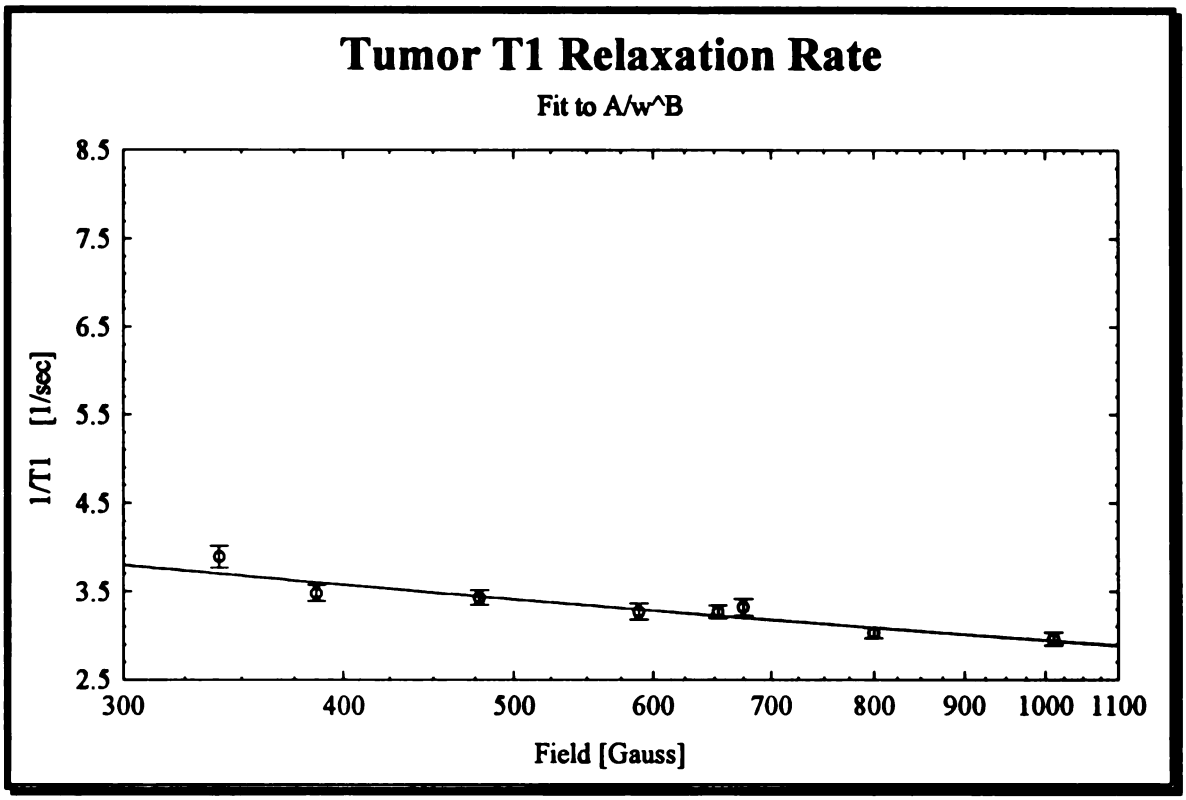

Figure 7.8

χ^2 fit of tumor longitudinal relaxation rate data. The resulting parameters to the power law fit $y = A/\omega^B$ were A = 4.0 MHz and B = .212

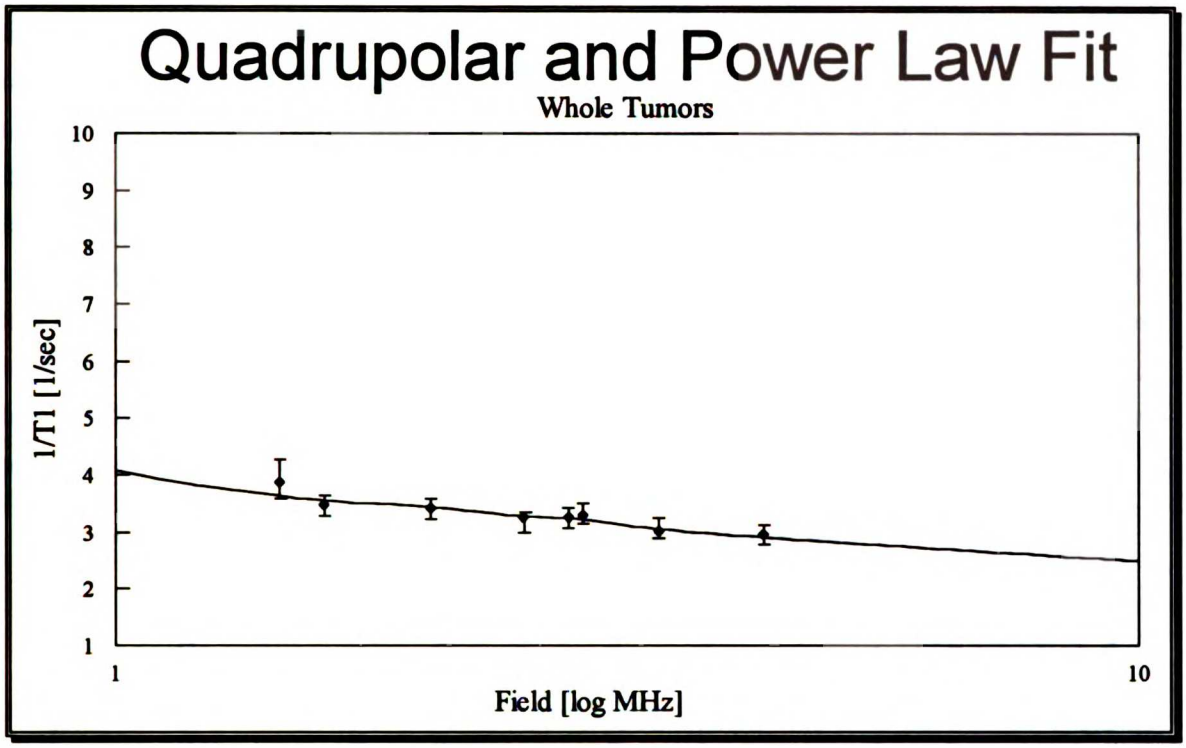

Figure 7.9
Graph of χ^2 fit to tumor data using the sum of quadrupolar and power law expression. The peaks were assumed to be at the same location as the muscle.

Table 7.11
Power law fits to tissue data

Tissue Type	A	B
Muscle	6.9	.252
Adenocarcinoma	3.7	.181
Normal Brain	4.1	.106
Edematous Brain	2.4	.01

As show in the figure 7.9, tumor does not show any ^{14}N cross relaxation peaks of statistical significance. The tumor show signs that the peaks may at least be at the same frequency but because to the insignificance of the tumor peak data, nothing more can be extrapolated. Being at

the same frequency is saying that the proton's asymmetry environment of tumor is very similar to muscle which implies that the backbones of proteins are very similar in their geometric arrangements regardless of the tissue. The asymmetry factor being the same for most tissue types is not too surprising because the nitrogen causing the relaxation is in the backbone which more or less is the same for most proteins. Figure 7.10 shows the reason for this relative invariance of asymmetry factor. The dominate nitrogen sink at low fields is from the backbone which is bonded to a couple of carbons and the proton in which the cross relaxation occurs. The only nuclei that have the possibility of affecting the asymmetry are the different side chains, but the typical distance between the side chain and nitrogen is much larger than the ~1Å bond between the nitrogen and proton making the effects from the side chain and other nuclei very small.

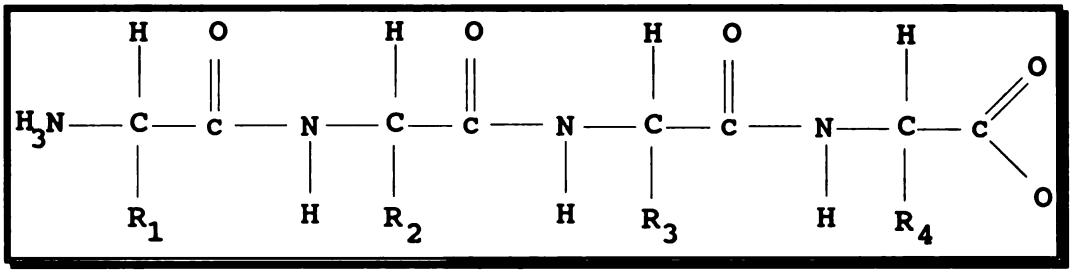

Figure 7.10
Schematic of a very short polypeptide (protein) chain. At the left, is the amino terminus and opposite to it is the carboxyl terminus. At physiological pH, the terminals are charged.

The non occurrence of peaks requires the condition of $\omega_q \tau_c << 1$, and assuming that this condition is the primary cause of the non occurrence of peaks gives the quadrupolar correlation time for tumors as,

$$\tau_c < \frac{1}{\omega_q} \approx \frac{1}{2\pi(2.87\text{MHz})} = 55.5\text{nS} \qquad \text{Eqn 7.11}$$

Assuming that the primary cause of cross relaxation is the backbone NH, the cross relaxation condition means that the correlation time represents the whole macromolecule motion. This implies that the volume of the macromolecule is given as,

$$V < \frac{\tau_c kT}{\eta} = \frac{55.5\text{x}10^{-9} \cdot 1.38\text{x}10^{-23} \cdot 310}{0.006916 \cdot} = 3.4\text{x}10^{-26}\,\text{m}^3 \qquad \text{Eqn 7.12}$$

which gives a radius of 32 Å. The adenocarcinomas by not showing the peak imply that the macromolecule is smaller than 36 Å, though the hint that the cross relaxation peaks being present may also imply that the macromolecule in question may have a radius of ~36 Å, which corresponds to a macromolecule of mass ~200k Daltons.

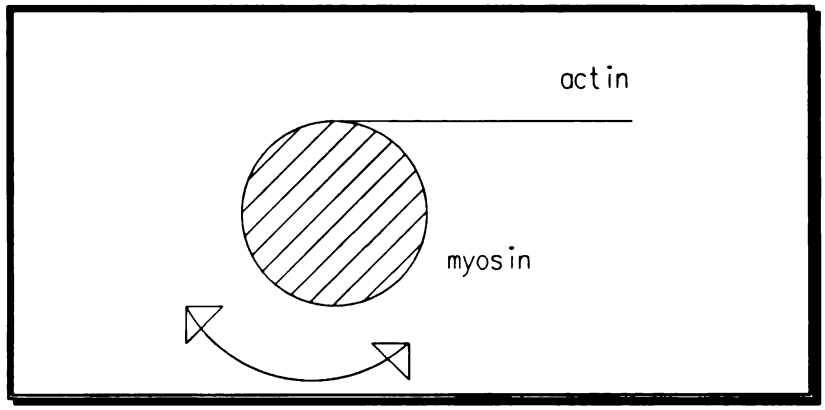

Figure 7.11
A simple model of a muscle fiber. The myosin head is assumed as the primary macromolecule providing the relaxation pathway for the protons.

A simple model for muscle can be used to calculate the correlation time. The myosin head has a restricted motion, very much like a balloon at an end of a stick. The moment of inertia is different for an attached sphere than a free sphere spinning about its own axis. The number of degrees of freedom is two rather than three and is confined to rotations about the attachment point of the action strand as represented in figure 7.11. The moment of inertia is given as

$$I_{ij} = \int_V \rho(\mathbf{r}) \left[\delta_{ij} \sum_k x_k^2 - x_i x_j \right] dv \qquad \text{Eqn 7.13}$$

Because of the symmetry, the problem is more tractable than it looks. The moment of inertia for a sphere rotating about a point on its surface is simply,

$$I = \int_V r^2 dm = r^2 \cdot (\text{mass of myosin head}) \qquad \text{Eqn 7.14}$$

and assigning the angular energy to kT,

$$kT \sim \tfrac{1}{2} I\omega^2 \qquad \text{Eqn 7.15}$$

Using the radius of a myosin head as 5 nm, (taken from photograph in ref [*39*]) and knowing that the moment of inertia for a solid sphere is $(2/5)Ma^2$, gives the ratio of a free head versus a semi bound myosin head as,

$$\frac{I_{free}}{I_{bound}} = \frac{\frac{2}{5}Ma^2}{Ma^2} = \frac{5}{2} \qquad \text{Eqn 7.16}$$

So the correlation time should be longer by a factor of $\sqrt{5/2} \sim 1.5$ from that given from Koenig's graph. For a 510kD protein, the graph gives .8MHz, so the myosin head should have an inflection frequency of .53 MHz, which gives a correlation time of $\tau_c \sim$ 172 ns. This model maybe conceptually nice, but the amount of myosin is considerably smaller than the amount actin in muscle so the exact contributions from either the myosin or actin is not known.

Normal and Edematous Brain

Figure 7.12 is the T_1 NMR dispersion for normal and edematous rat brain. The dispersions for the two types of tissues are very similar. Tissue longitudinal relaxation rate is known to scale linearly with the inverse of water content. To test this hypothesis, table 7.12 calculates the average of the ratio of the normal and edematous longitudinal relaxation rate. The average ratio of 1.29±.04 has a fairly small standard deviation, implying that the ratio may not have a dispersive nature. Figure 7.13 has the edematous data multiplied by 1.29 and plotted on top of the normal brain data. The general behavior scales very nicely, with the only exception being where the maximum occurs. The maximums are slightly different, 589 G for edema and 653 G for normal brain. Assuming that the water content dependency is correct, this scaling implies that

$$\frac{T_{1,edema}}{T_{1,normal}} = \frac{P_{water,edema}}{P_{water,normal}} = 1.29 \qquad \text{Eqn 7.17}$$

which is higher than the value obtained from dehydration. Table 7.10 gives a water content ratio of 84.5/78.6 = 1.08 between edematous and normal brain tissue. The 1.08 ratio figure may be misleading because, as discussed before, not all water protons contribute equally to the relaxation

rather it is the proton fractions coupled to the macromolecules that are the primary relaxation protons.

Cold probe induced edema is a vasogenic type of edema. The breakdown of the blood brain barrier releases large amounts of macromolecules not normally found in the extracellular spaces of the brain. Water in the edematous portion of the brain increases but the total amount of protein in that portion of the brain probably does not increase as much. Some proteins may be transported to the edematous area from the blood flowing into the area. The water content determination from the desiccant method shows an increase in water content of 8% over any increase in protein content since such a procedure will produce a normalized water-protein concentration measurement.

Apparent in figure 7.13 is the independence of the dispersion profile with water content. The basic functional behavior is the same for the edematous and normal brain. The primary difference is the different field values where the quadrupolar peak is maximum. This similarity in profile may have implications for the dispersion mechanism. The edematous tissues have essentially the same pathological structure as normal tissue except for increased protein and water in the extracellular space from the breakdown of the blood brain barrier. The increase in protein and water content produces an increase in relaxation time but does affect the NMRD.

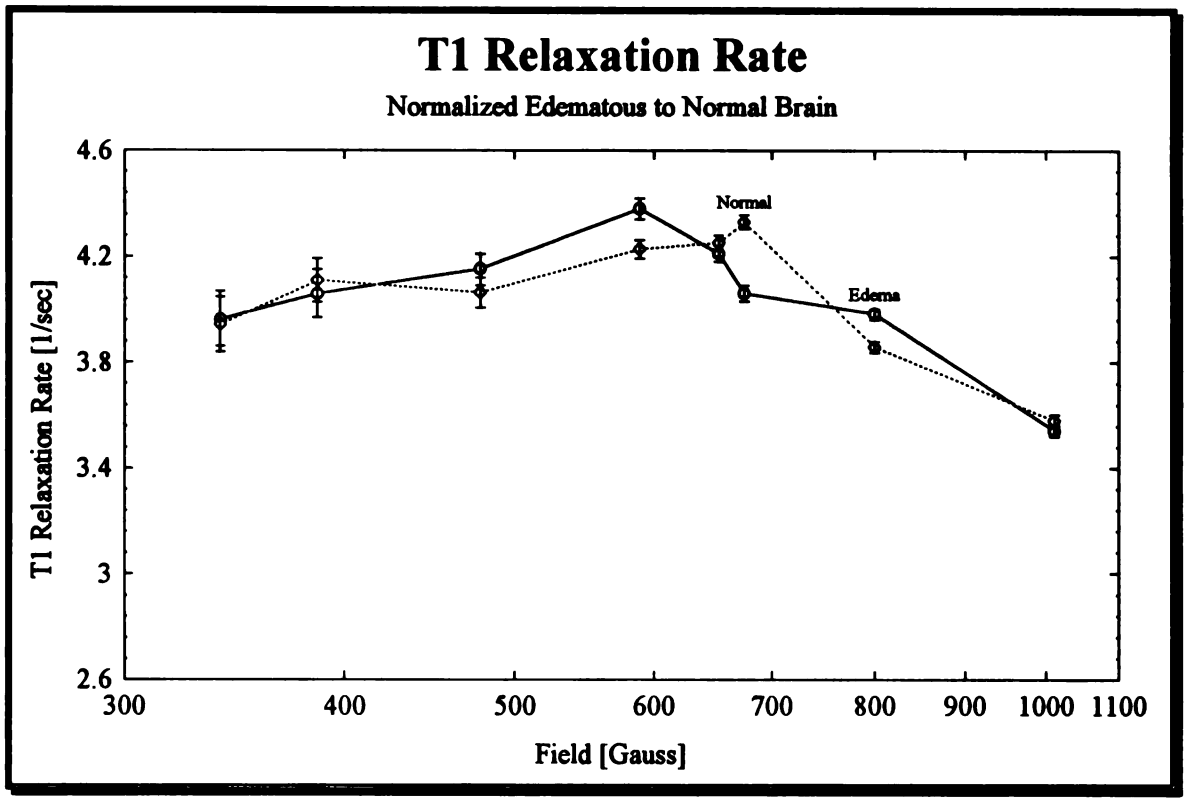

Figure 7.12

Longitudinal relaxation rates for normal and edematous brain. Notice that the trend is very much alike having a curvature peaking ~600Gauss.

Table 7.12

Table of normal and edematous brain T1s. Column one is the ratio of edmatous and normal brain T1 and the last column is the edematous T1 normalize by this ratio.

Field	$(T_{1,edema}/T_{1,normal})^{-1}$	$1/T_{1,edema}$	$1/T_{1,normal}$	$\left(\frac{T_{1,edema}}{T_{1,normal}}\right)^{-1}_{Ave} T_{1,edema}$
340	1.28	3.08	3.94	3.97
386	1.30	3.15	4.09	4.06
478	1.26	3.22	4.06	4.15
589	1.24	3.40	4.23	4.39
653	1.30	3.27	4.26	4.22
675	1.37	3.15	4.33	4.06
800	1.25	3.09	3.85	4.12
1011	1.30	2.75	3.58	3.55
Ave	1.29±0.04			

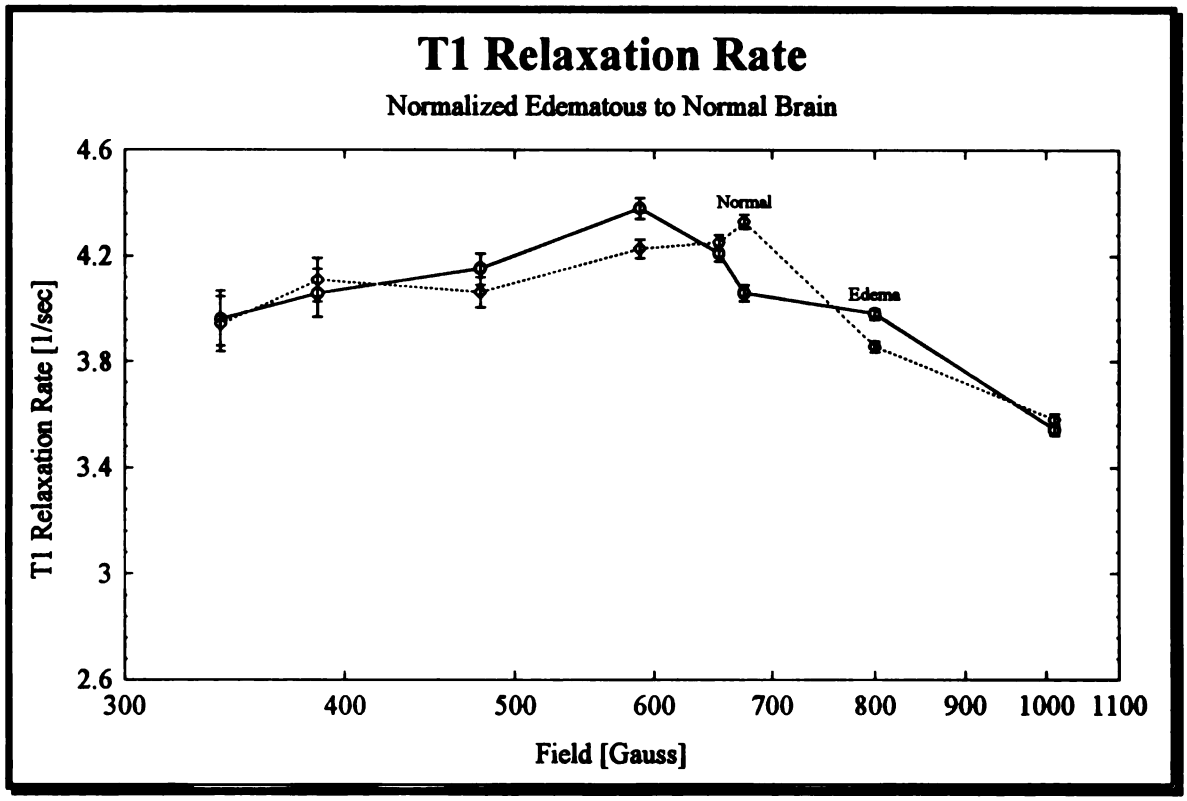

Figure 7.13

Plot of longitudinal relaxation rate of the normalized edematous tissue and normal tissue. The edematous data were scaled by a factor of 1.29 and plotted on top of the normal tissue. The edematous data scale nicely. The main difference between the edematous and normal tissue is where the maximum occurs.

Only a single peak is apparent on both brain NMRDs. From the previous discussion on quadrupolar cross relaxation, equation 2.31 predicts that for single peak to occur requires either $\eta \sim 0$ or $\eta \sim 1$. The case where $\eta = 0$ has ω_1 and ω_2 being equal, has these two peaks coalesce and the second peak at $\omega_3 = 0$ (i.e. DC). The possibility that a second peak is at a field lower than the field range obtained can be accommodated by an asymmetry factor fitting the condition,

$$\eta > \frac{3\omega'}{1-\omega'} \sim .946 \qquad \text{Eqn 7.18}$$

where

$$\omega' = \frac{\omega_1 - \omega_2}{2\omega_1} = .24$$

which is not much different for η~1. Assuming that the asymmetry factor is one, the quadrupolar coupling constant becomes

$$\frac{K}{\hbar} = 4.37 \text{rad} / \text{sec}$$

which provides the location of the three peaks for $\eta = 1$ as,

$$\omega_1 = (2\pi)(1.39 \text{ MHz})$$
$$\omega_2 = (2\pi)(2.78 \text{ MHz})$$
$$\omega_3 = (2\pi)(1.39 \text{ MHz})$$

Having $\eta = 1$ is not as good a choice as $\eta = 0$ for the reason that two of the peaks will coalesce at a field less than 340 G. Having two at the same field implies that this peak will have twice the amplitude as the higher field single peak. From the brain NMRD, this skewing is not apparent so the logical choice for the asymmetry factor is $\eta = 0$.

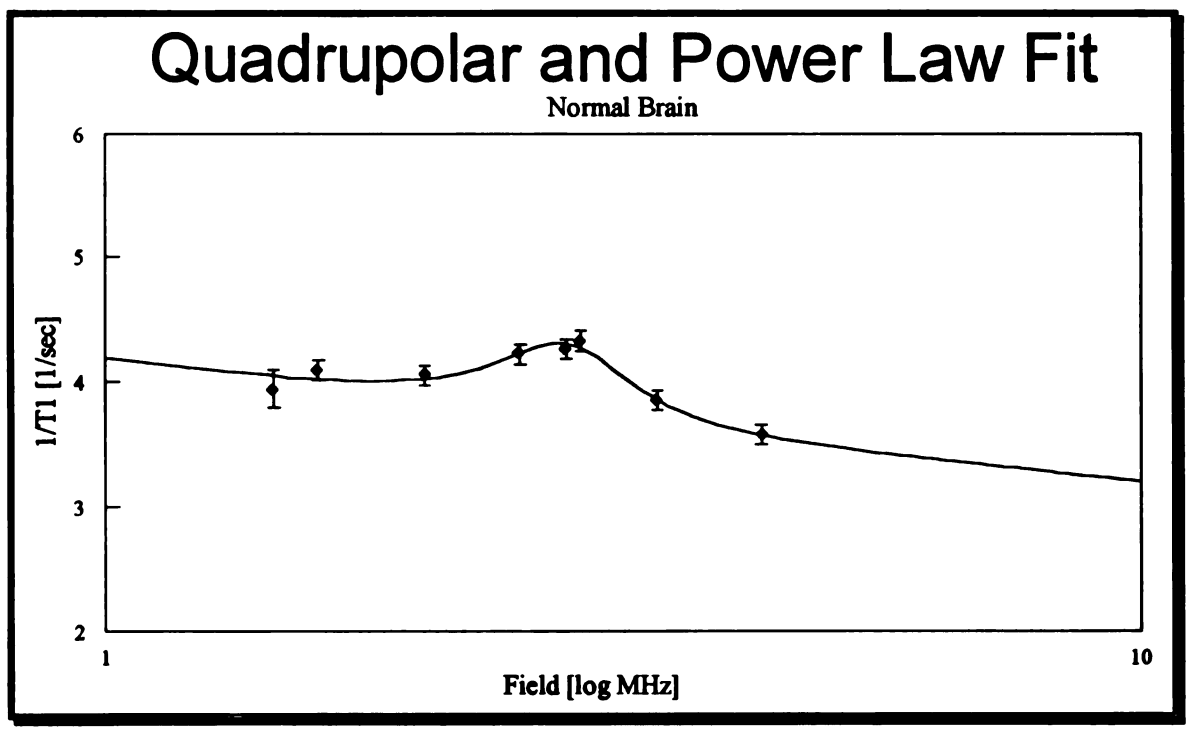

Figure 7.14
A χ^2 fit to the normal brain T1 relaxation data. The model is a sum of the quadrupolar and power law models. The quadrupolar model assumes a single peak a 653 G.

Figure 7.14 is a χ^2 fit of normal brain data to a sum of the quadrupolar and power law fit. The biological complexity of the brain will thwart any attempt to rationalize the significance of the fit. The only statement that is justified is to say that the correlation times represent an in vivo ensemble average of MR correlation times.

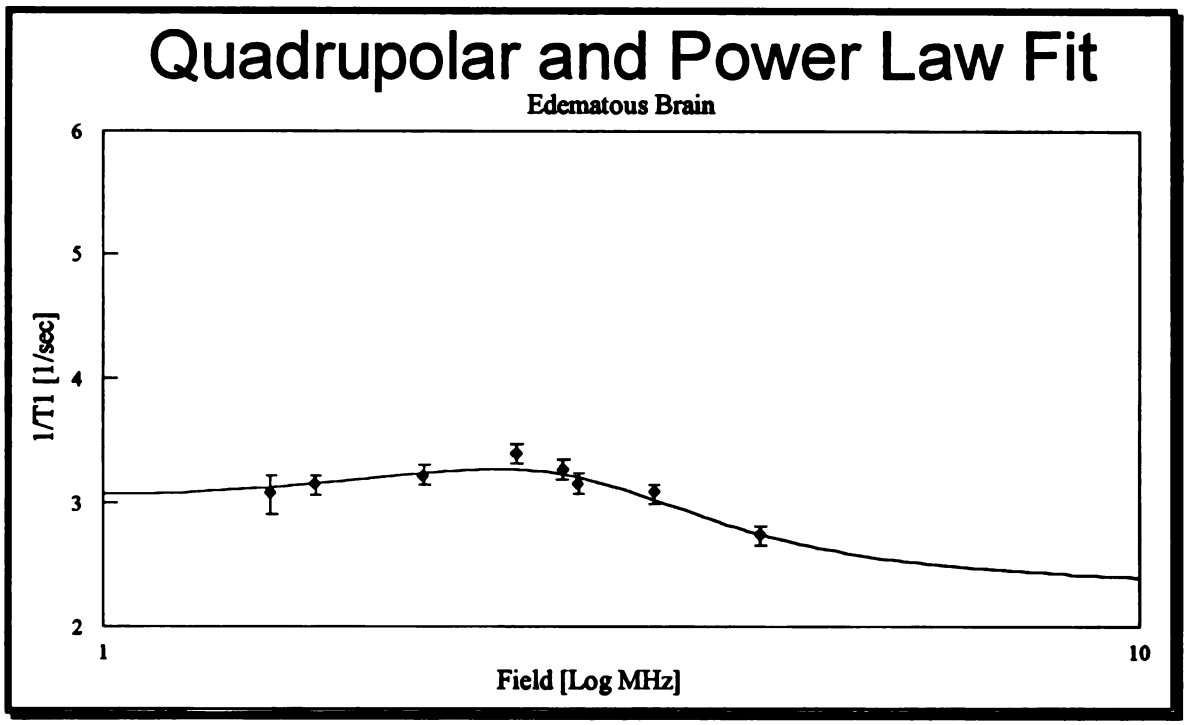

Figure 7.15
A χ^2 fit to the edematous brain T1 relaxation data. The model is a sum of the quadrupolar and Lorentz models. The quadrupolar model assumes a single peak a 589 G.

Figure 7.15 is a χ^2 fit of edematous brain data to a sum of the quadrupolar and Lorentizian. The $\chi^2 = 8.5$, with a dipolar correlation time of 7.9 ns and a quadrupolar correlation time of 105ns. As discussed in the previous paragraph, not much can be said about the correlation times except for the fact that the values are unusually short represents very small molecules.

Table 7.13

Lorentzian fits to the tissue data, and relationship between correlation time and molecular weight obtained from data.

Tissue Type	Dipolar Correlation Time	Quadrupolar Correlation Time	Peaks ?
Muscle	16 ns	800ns	two
Adenocarcinoma	1780ns	428ns	?No
Normal Brain	1107ns	270ns	one
Edematous Brain	217ns	105ns	one

Table 7.13 shows the fitting parameters for the combined Lorentz and quadrupolar fits. The one number that is unsettling is the dipolar muscle correlation time which is extremely short. The large difference between the dipolar correlation time between normal and edematous brain is also extreme.

Table 7.14 shows the fitting parameters for the combined power law and quadrupolar fits. The interesting result is the two fits produced rather similar correlation times for the quadrupolar components. The quadrupolar function behaves the same irrespective the dipolar baseline used for the fit. The only tissue type that differs substantially was muscle and only by 35%.

Table 7.14

χ^2 fit to tissue data using a sum of a quadrupolar and power law fit

Tissue Type	A	B	Quad Cor Time	θ	D	χ^2	Peaks ?
Muscle	6.9	.252	523ns	1.6	.26	24	two
Adenocarcinoma	3.7	.181	512ns	~0	.05	5.9	?No
Normal Brain	4.1	.106	300ns	1.6	.10	8.2	one
Edematous Brain	2.4	.01	103ns	1.6	.35	16	one

Transverse Relaxation

Transverse relaxation dispersion is not as well studied as longitudinal relaxation dispersion. The primary reason is the difficulty in obtaining T_2 relaxometry data because relaxometers can easily obtain T_1 data over a few orders of magnitude field points but cannot measure T_2's. The difficulty measuring T_2 on an relaxometer is that the field switch rise time needs to be very fast and switching hardware at such a large current is very difficult. This experiment was designed to obtain T_2 as well as T_1 at every field. T_2 dispersion is a relatively unknown territory where typical speculation is that it behaves as predicted by the BPP theory and differs from T_1 by a susceptibility term.

Muscle and Adenocarcinomas

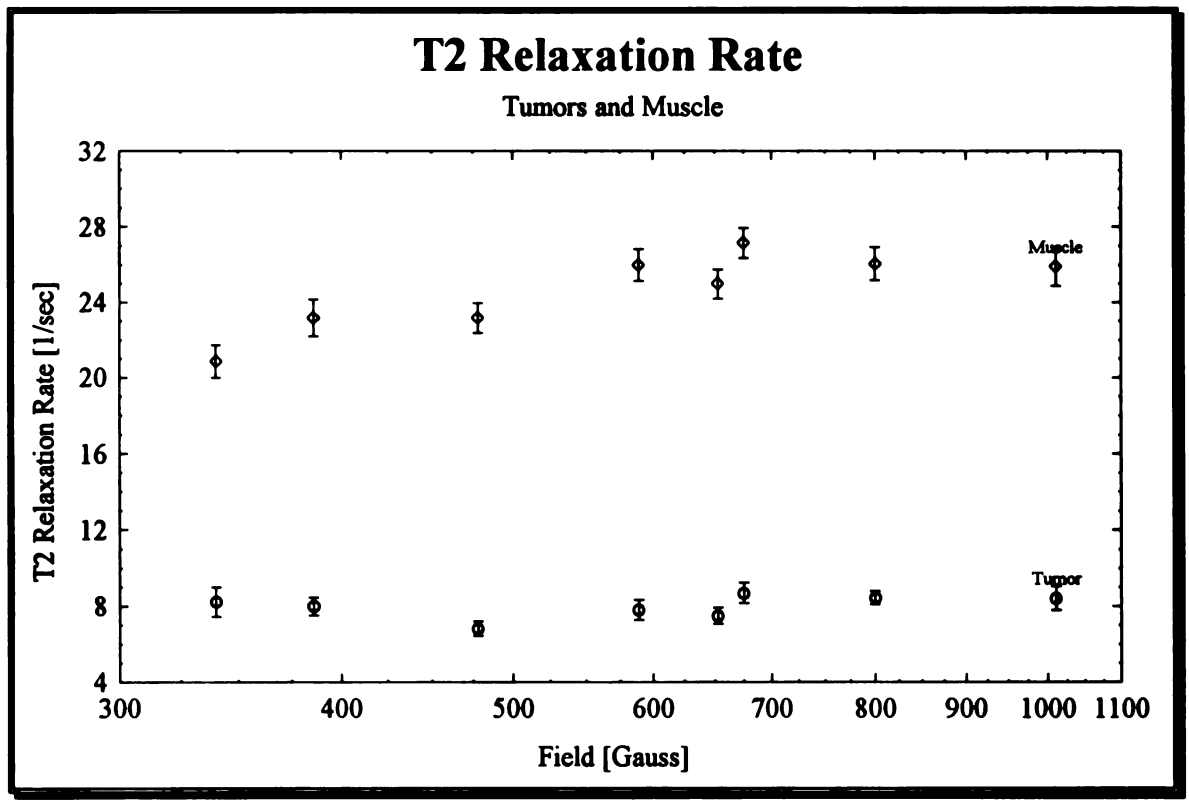

Figure 7.16
Neither the muscle or tumor T2 relaxation were affected by cross relaxation. The tumor NMRD does not have any dispersion while the muscle NMRD has an increasing relaxation rate.

Figure 7.16 shows the transverse relaxation rate dispersion for muscle and tumors. Muscle and tumors have very different $1/T_2$ dispersion in contrast to their similar $1/T_1$ dispersion. The tumors $1/T_2$ have no dispersion while the muscle has a monotonic increasing transverse rate. The transverse rate dispersions for muscle have a vague resemblance to the ^{14}N dips, which is opposite to that of the longitudinal rates. These dips are small and should not be used as proof of transverse ^{14}N cross relaxation because the dips are within the statistical uncertainty.

Muscle has a T_2 relaxation rate (R2), that is monotonically increasing with increasing field while tumors have virtually no dispersion. The muscle's increasing R2 is a little puzzling if the assumption that the BPP function for T_2 is used. T_2s should, more or less, have the same functional form as R1s, except for a *j(0)* contribution which can provide the explanation for the differences between T_1 and T_2 at low fields, but have $T_1 \sim T_2$ at high fields. Data at higher field (~5T) show that R1 decreases with field while R2 continues to increase at this field. Examining the relaxation equation in the Redfield limit may elucidate a possible mechanism for this difference. The expression for the transverse relaxation in the Redfield limit is,

$$\frac{1}{T_2} = \gamma_n^2 \left[\overline{H}_z^2 \tau_c + \overline{H}_y^2 \frac{\tau_c}{1+\omega_o^2 \tau_c^2} \right] \qquad \text{Eqn 7.19}$$
$$= \frac{1}{T_2'} + \frac{1}{2T_1}$$

The T_1 and T_2 are the measured data, and T_2' is the *j(0)* contribution to T_2. Subtracting the $1/2T_1$ term from equation 7.19 will produce the j(0) term. Figure 7.17 shows the $1/T_2'$ for muscle and tumors. The slope is considerably larger for muscle than for tumors. A proposed mechanism for this dispersion is due to the susceptibility effects of the molecular interface of the protein. From Curie's law, the magnetization is given as,

$$M \approx \frac{N\mu^2 B}{k_b T} \qquad \text{Eqn 7.20}$$

The local magnetization near a proton will increase proportionally with increasing field. This will provide an increase in local inhomogeniety around the microenvironment of the relaxing proton. Comparing tumors with muscle would be difficult because of the obvious difference in tissue type, but the edematous brain model may provide some insight on T_2. Curie's law implies that the slope of the line is proportional to the strength of the magnetic moment squared and to the number of sites.

Figure 7.17 shows linear fits for muscle and tumors to their corresponding $1/T_2'$ component of the transverse relaxation. Taking the ratio of the slopes for the two tissue models will not reveal enough information because of the dissimilarity of tissue origin between muscle and tumors. The ratio will yield more information for the edematous brain model, as will be shown later.

Table 7.15

χ^2 fit to 1/T2' of muscle and tumors.

Tissue Type	Slope	Intercept	χ^2
Muscle	3.01	3.79	13
Adenocarcinoma	.368	0	19

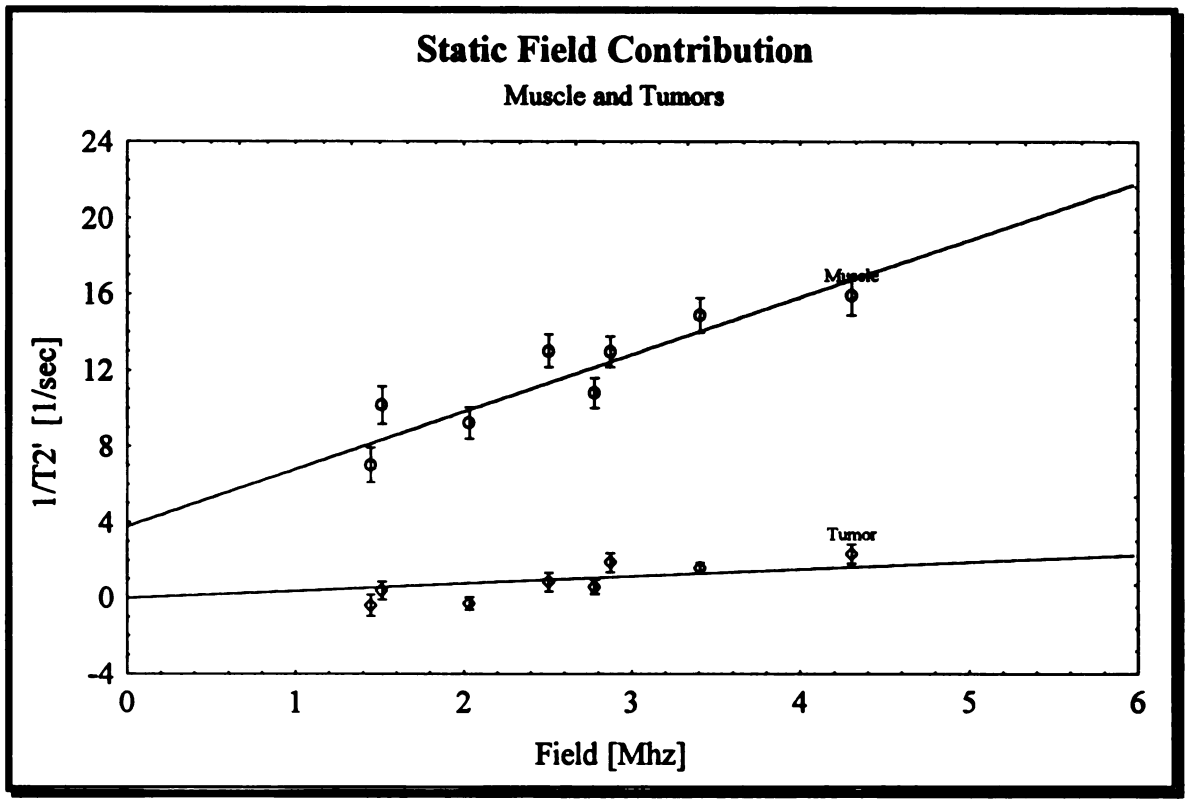

Figure 7.17

Linear χ^2 fit to $1/T_2'$ for muscle and tumors. The slope is related to magnetization via Curie's law.

Edematous and Normal Brain

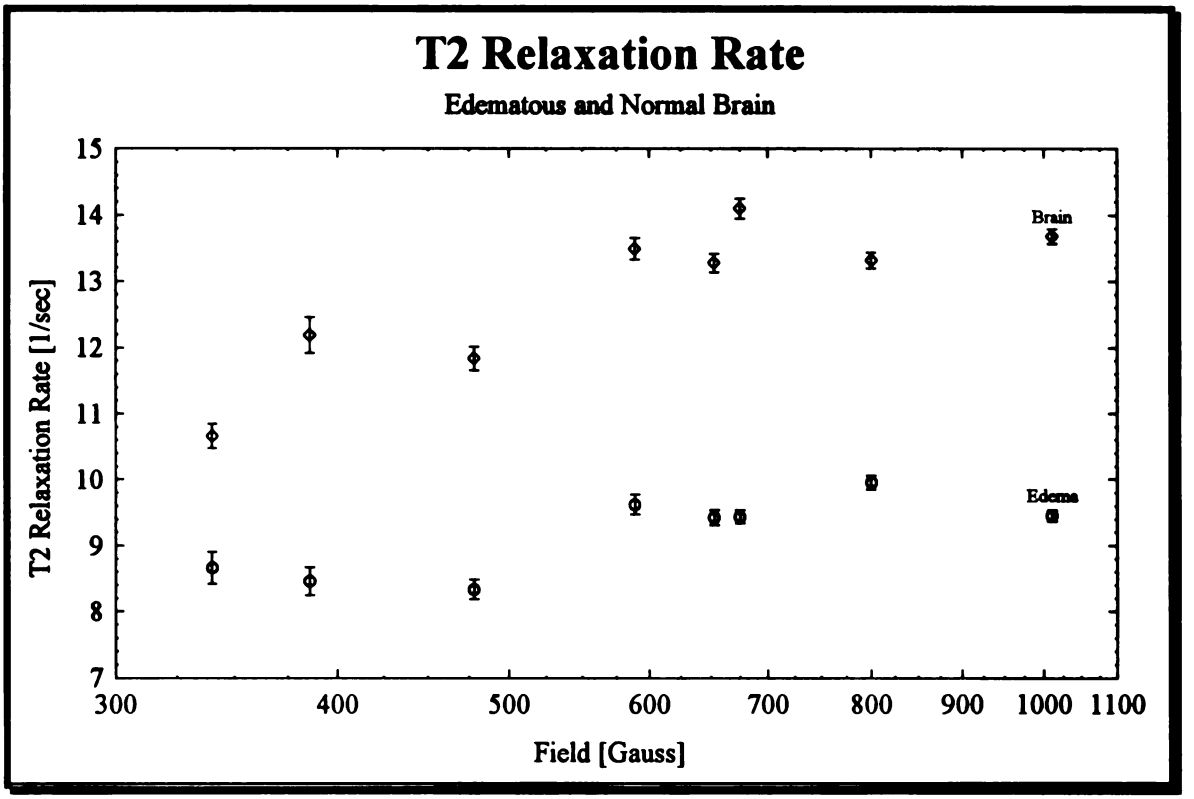

Figure 7.18
The transverse relaxation rate dispersions have a monotonic increasing behavior, more like muscle than adenocarcinomas.

Table 7.16

Normalized T2 rate for Edematous and Normal Brain

Field	$R_{2,edema}/R_{2,normal}$	$R_{2,edema}$	$R_{2,normal}$	$\left(\frac{T_{2,edema}}{T_{2,normal}}\right)^{-1}_{ave} T_{2,edema}$
340	1.23	8.66	10.66	12.21
386	1.48	8.19	12.12	11.55
478	1.43	8.28	11.83	11.67
589	1.40	9.62	13.50	13.56
653	1.42	9.39	13.30	13.24
675	1.49	9.44	14.10	13.31
800	1.34	9.91	13.32	13.97
1011	1.45	9.45	13.68	13.32
Ave	1.41±0.030			

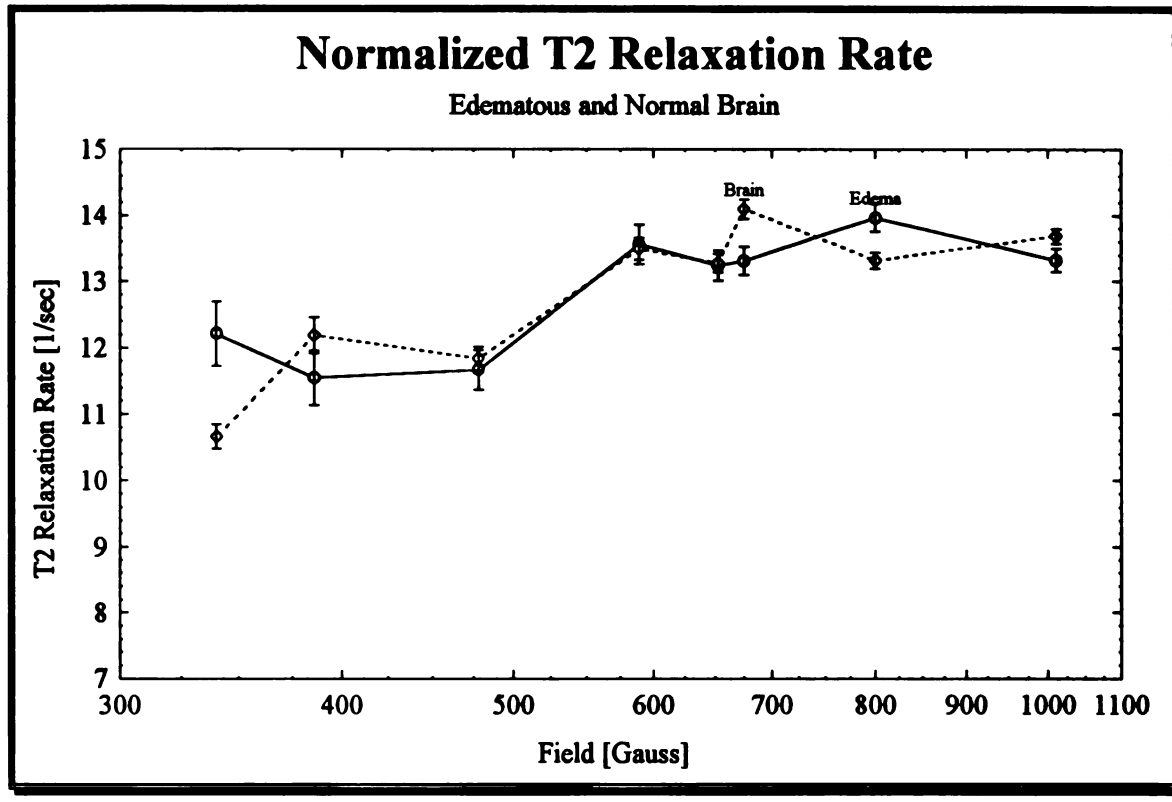

Figure 7.19
Graph of normalized edematous and normal brain. The relaxation times of the edematous brain were multiplied by the average of the ratio of $(T_2\text{edema}/T_2\text{normal})^{-1}$.

As figure 7.18 shows, the dispersion behavior of edematous and normal brain look very much alike, except for a baseline shift. Table 7.16 calculates the T_2 ratio of normal and edematous brain producing an average ratio of 1.4. This value is used to normalize the edematous brain data to superimpose it to the normal brain data. Figure 7.19 plots the result of this normalization. As with T_1, the edematous data scales fairly well. The T_2 ratio is higher than the T_1 ratio, with both higher than the water content ratio of 1.08.

Figure 7.20 plots the measured water content for edematous and normal brain. Notice that the water content varies little over the experiment field, within a percent.

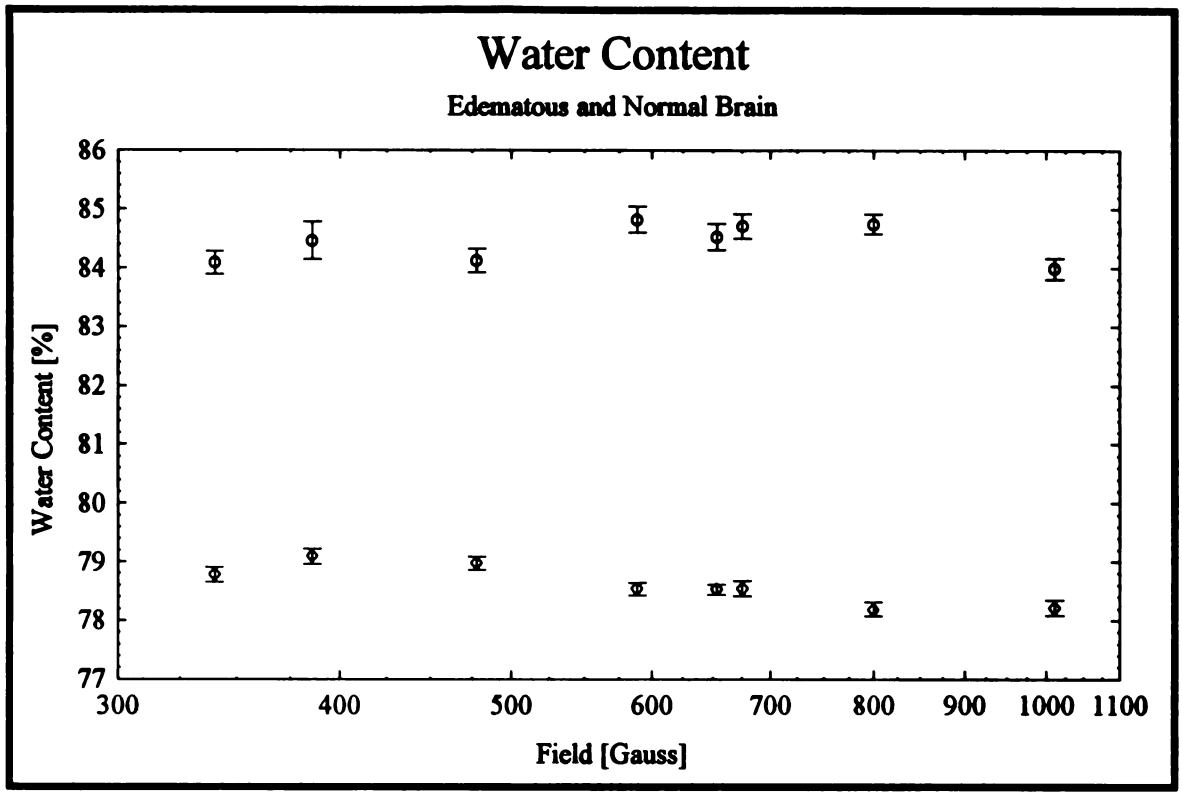

Figure 7.20
Water content of edematous and normal brain tissue at different fields

All three relaxation parameters are dependent on water content. Pure water has T_1 and T_2 of about 3 secs with no dispersion. MRI is looking at water molecules having relaxation times considerable shorter than 3 secs and having dispersion. The obvious cause is the macromolecue's molecular dynamics influencing the water molecule but the details of the mechanism of this influence is open to discussion. Because adenocarcinomas and muscle are very different tissue types, comparing the two relaxation times as a function of water content would not be correct. Figure 7.22 shows this incompatibility. Relaxation rates generally decrease with increasing water content, and for many tissues are inversely proportional to the water content. The relaxation rate of muscle is twice that of tumors but only has about 14% lower water content.

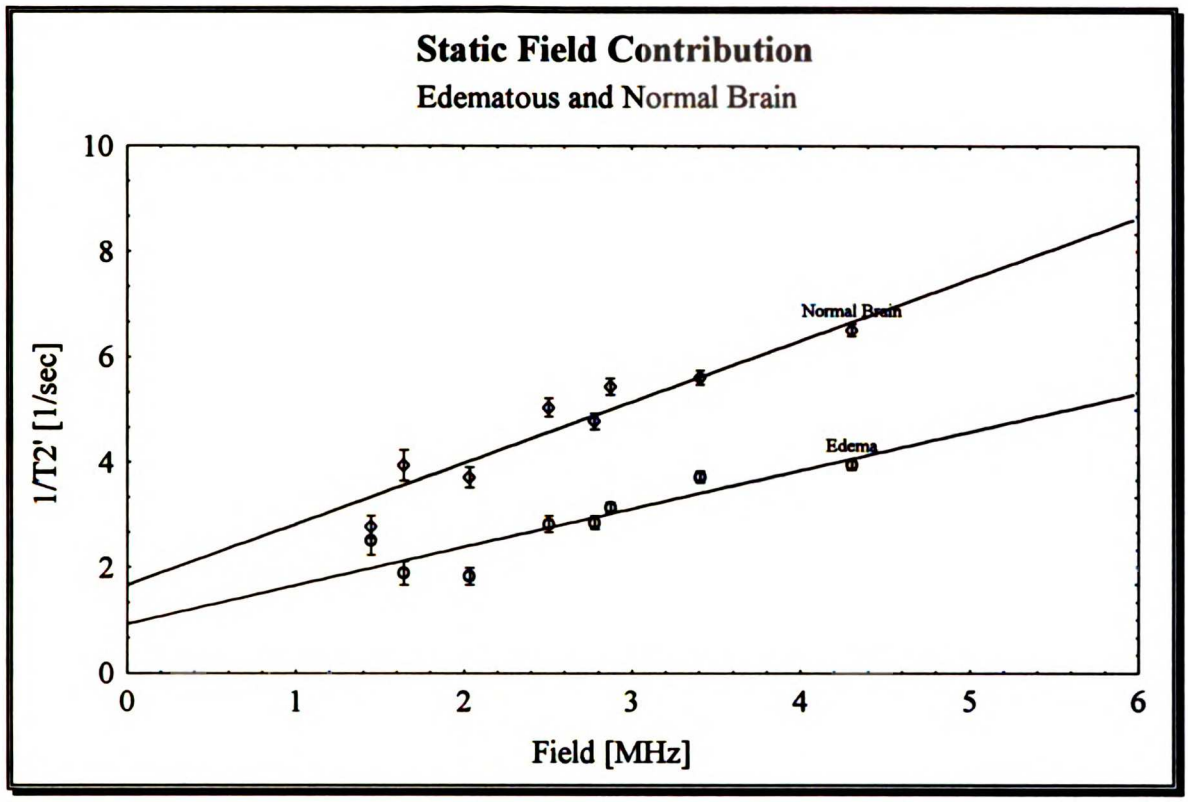

Figure 7.21
Linear χ^2 fit to $1/T_2'$. $1/T_2'$ is obtain by subtracting the $1/T_1$ term.

Table 7.17
χ^2 fitting parameter to edematous and normal brain T2 data.

Tissue Type	Slope	Intercept	χ^2
Normal Brain	1.16	1.66	28
Edematous Brain	.730	.93	29

The edematous brain T_2 data may provide other information if susceptibility is the primary cause for dispersion in T_2. Assuming the edematous and normal brain are similar, (though from the previous discussion, this is not totally true), we may extract the number of sites from the slope. From table 7.17, the ratio of the slope is,

$$\frac{A_{Normal}}{A_{Edema}} = \frac{(N\mu^2)_{Normal}}{(N\mu^2)_{Edema}} = \frac{1.16}{.730} = 1.59$$

If the magnetic moments are the same, this implies that the normal brain has more binding sites available than edematous tissue. The more likely scenario is the moments are different and are larger for normal tissue than edematous tissue.

Water Content

Water content plays a major role in MR imaging. Experiments that vary the water content of a given tissue produce relaxation times that have simple relations to water content. Correlation between different tissues with the same water content does not show such a simple relationship (if this was true, MRI would be a hydrogen density imager).

Figures 7.22 and 7.23 are plots of relaxation rates for tumor and muscle versus tissue water content and table 7.18 shows the corresponding linear fit parameters. The plots show the obvious grouping of relaxation rates for a particular water content. A normalization can be done on the relaxation rate data by assuming that the relaxation rate changes are due only to the changes in water content. With this assumption, the normalization parameter is the ratio of the average relaxation rate difference and the average water content difference.

Assuming that differences in water content are the primary causes for relaxation changes, normalization of the relaxation time relative to the water content should have the same behavior characteristics. Defining the change in relaxation rate per change in water content as,

$$S_{1,2} = \frac{\frac{1}{T_{1,2lesion}} - \frac{1}{T_{1,2normal}}}{P_{lesion} - P_{normal}} \qquad \text{Eqn 7.21}$$

and defining the average of S as,

$$\langle S_{1,2} \rangle = \sum_{\text{all fields}} S_{1,2} \qquad \text{Eqn 7.22}$$

gives the normalized relaxation rate relative to the lesion's water content as,

$$\frac{1}{T_{1,2}'} = \langle S_{1,2} \rangle (P_{normal} - P_{lesion}) + \frac{1}{T_{1,2}} \qquad \text{Eqn 7.23}$$

The implementation of the averages given in equation 7.22 was different of for brain than for muscle. The $\langle S \rangle$ value for the brain data has data from all the field included in the average while the value for the muscle

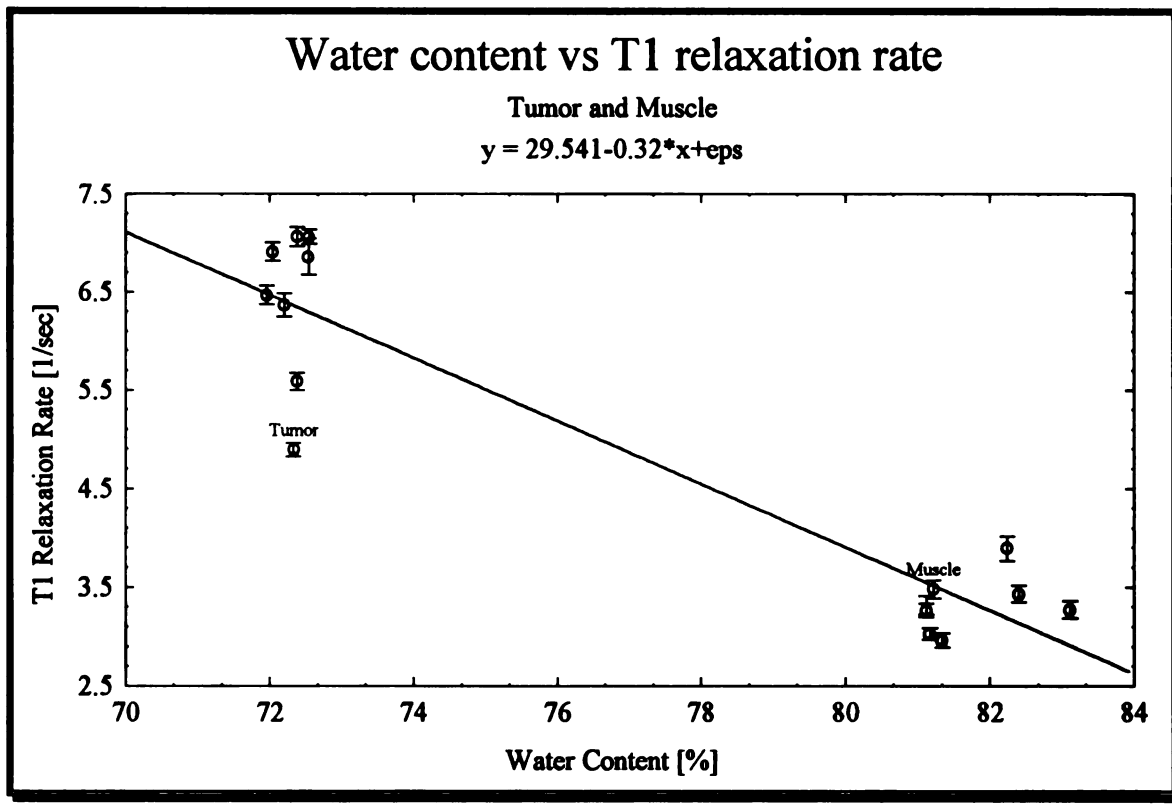

Figure 7.22

T_1 relaxation rate of tumor and muscle plotted against water content. Notice the much larger spread in T_1 relaxation rate for tumors while the spread for muscle is small.

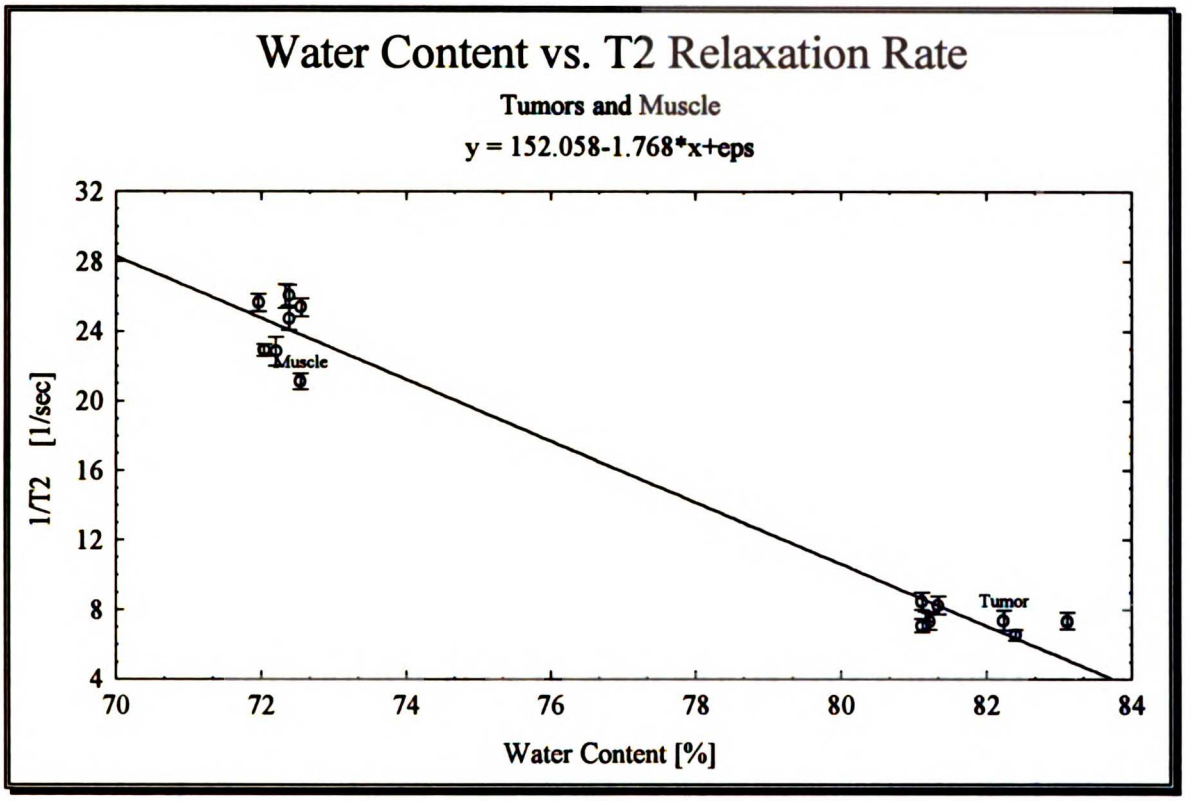

Figure 7.23

The spread for the tumors is considerably greater than that of muscles. The difference in the transverse relaxation rate is about a factor of 3 as compared to the longitudinal relaxation which differ by a factor of two for the same difference in water content.

Table 7.18

Linear fit of relaxation rates to water content.

Relaxation Rate	Slope	Intercept
$1/T_1$	-.32	29
$1/T_2$	-1.7	152

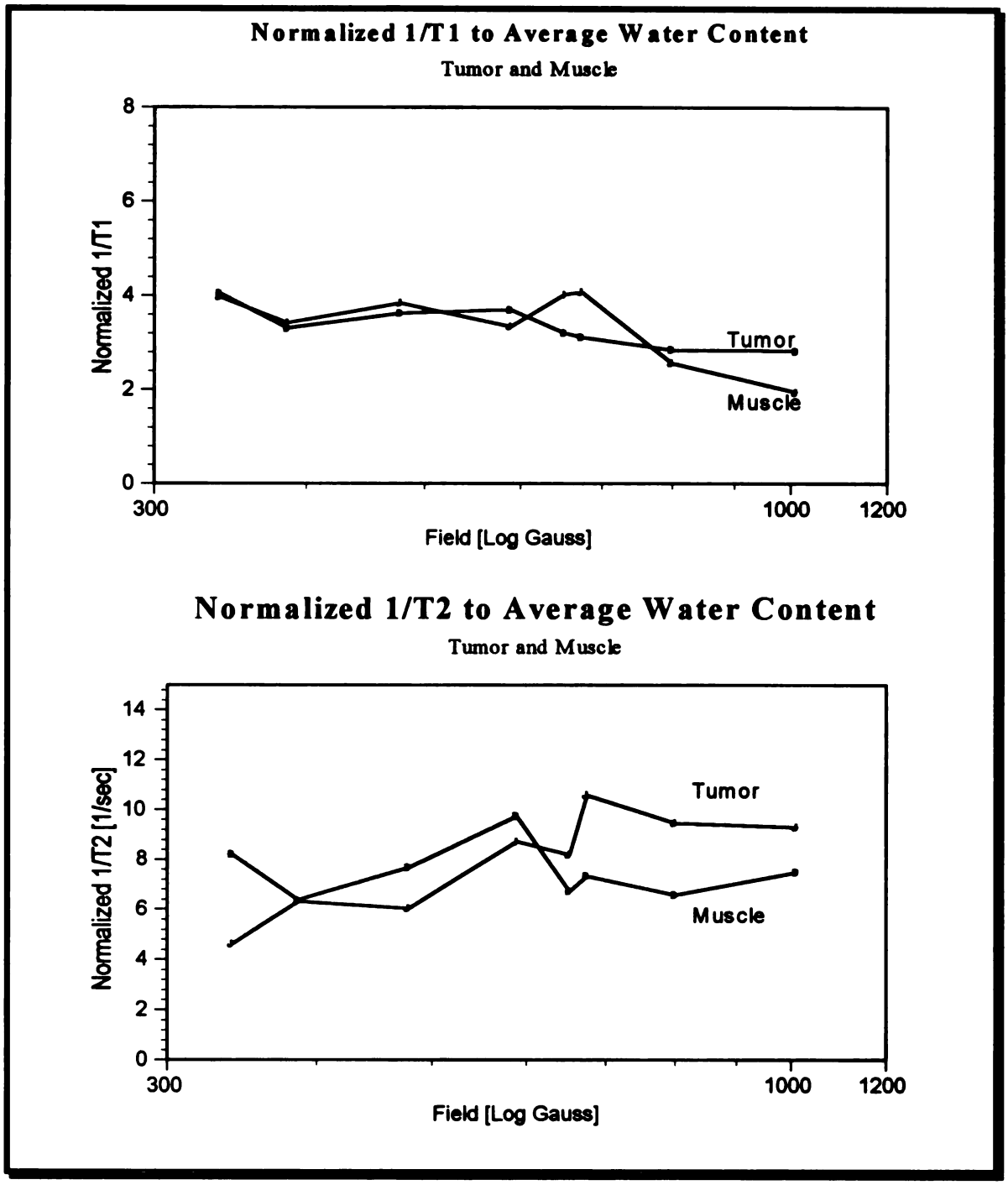

Figure 7.24

Graph of water content normalized T_1 and T_2 relaxation rate changes for tumors and muscle. The assumption is that all changes of relaxation rate are caused by the changes in water content. The 478, 63 and 675 Gauss points were not used in the averaging constant. The normalization constant is discussed in the text.

Figure 7.24 shows the relaxation data normalized using equation 7.23. Notice that the baseline for both the T_1 and T_2 show muscle and tumor have very similar characteristics. The T_2 data does have a larger scatter. Notice that the quadrupolar peaks are present only in the muscle data. What is of interest is the similar normalized dispersion properties for very different tissues.

Normal and Edematous Brain

As discussed previously in the muscle and tumor section, data with similar relaxation times will group together in a water content plot. Increased water content means lower relaxation rates, as shown in figures 7.25 and 7.26. The scatter for the edematous brain data was not very different from the normal brain data. Table 7.19 shows the corresponding linear fit parameters. Figure 7.27 has a different x-axis, where 1/water content is used rather than water content. This was done to compare data given by Kamann et. al [*44*]. The slope extracted from figure 7.27 produced a value of 19.5, considerably larger than given by Kamman. Kamman experiments were at 21.5 MHz.

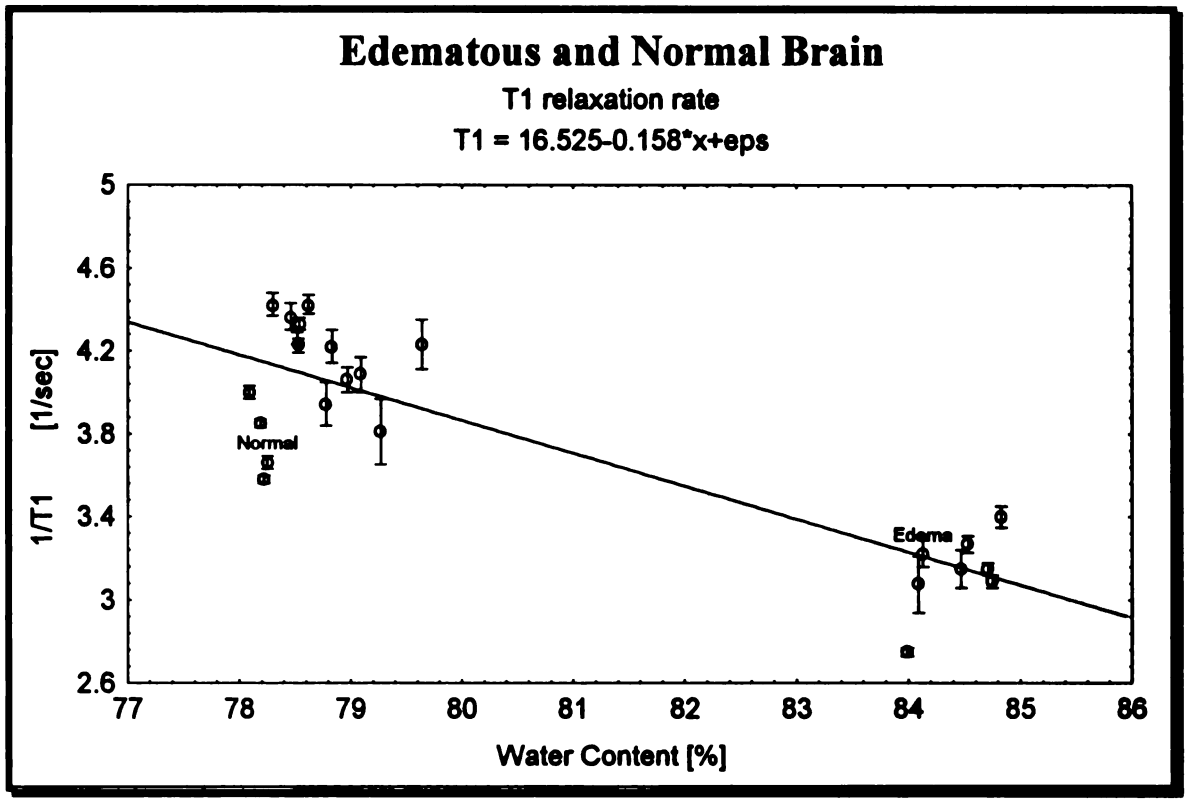

Figure 7.25

Plot of edematous and normal brain longitudinal relaxation versus water content. The normal brain data are split into a component in the opposite hemisphere to the infarct and another in the same hemisphere and below the infarct.

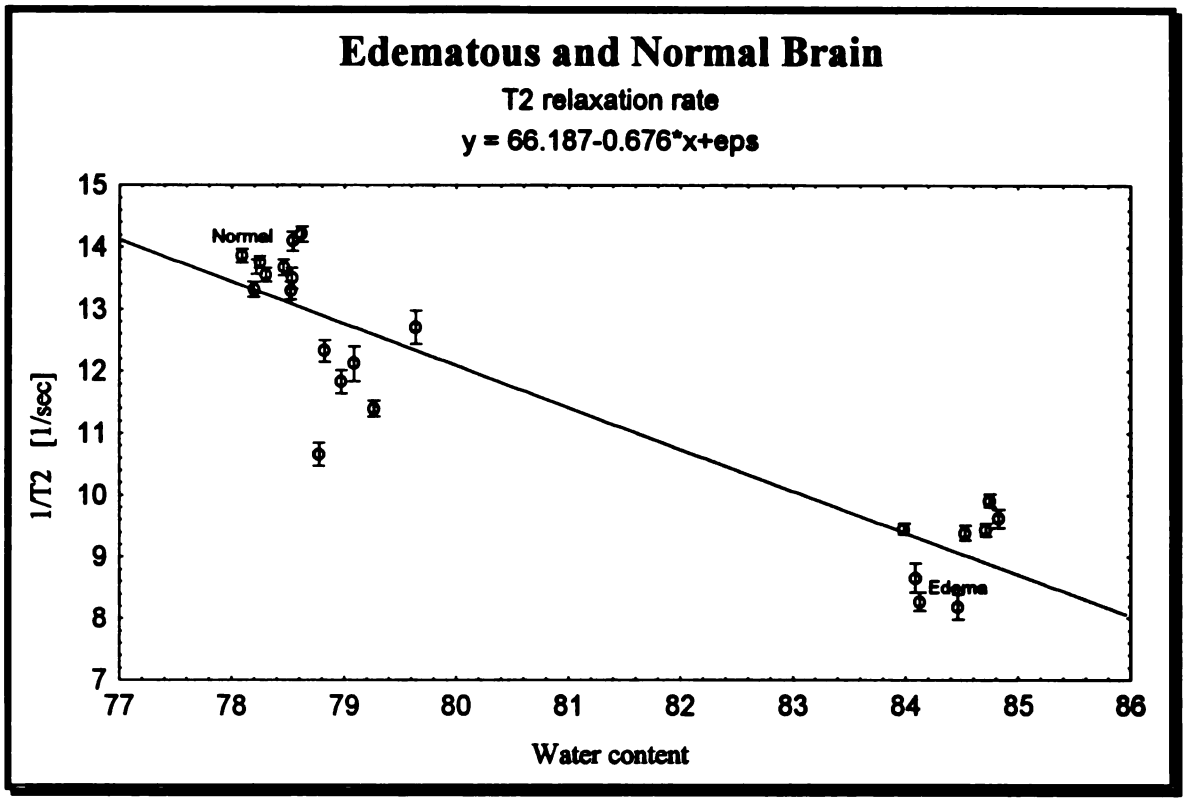

Figure 7.26

Plot edematous and normal brain transverse relaxation vs water content. The normal brain data are split into a component in the opposite hemisphere to the infarct and another in the same hemisphere and below the infarct.

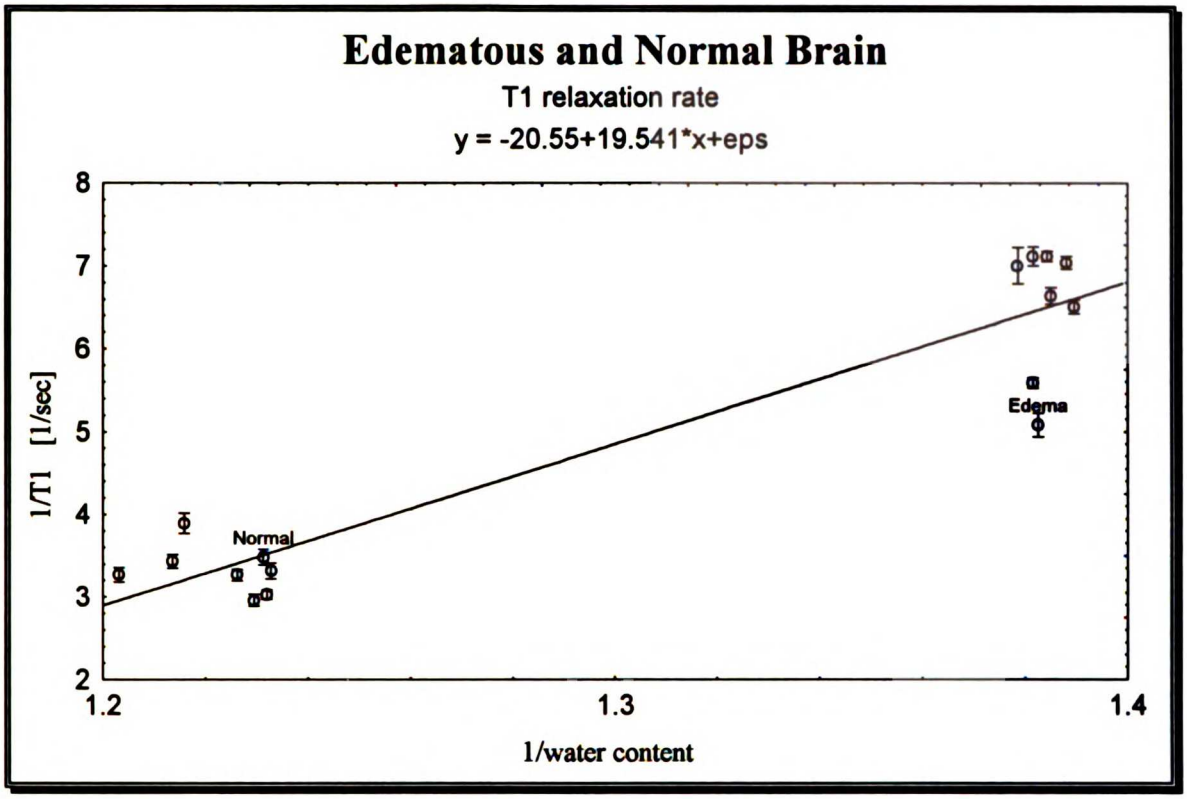

Figure 7.27

This plot has 1/water content as the x axis, which is different than previous plots. This was done to compare slope with data from earlier an publish experiment. The slope of line is 19.5, larger than what was determined by Kamman, et. al. for cat gray and white matter.

Table 7.19

Linear fit of transverse relaxation rates to water content.

	Slope	Intercept
$1/T_1$	-0.16	17
$1/T_2$	-0.68	66

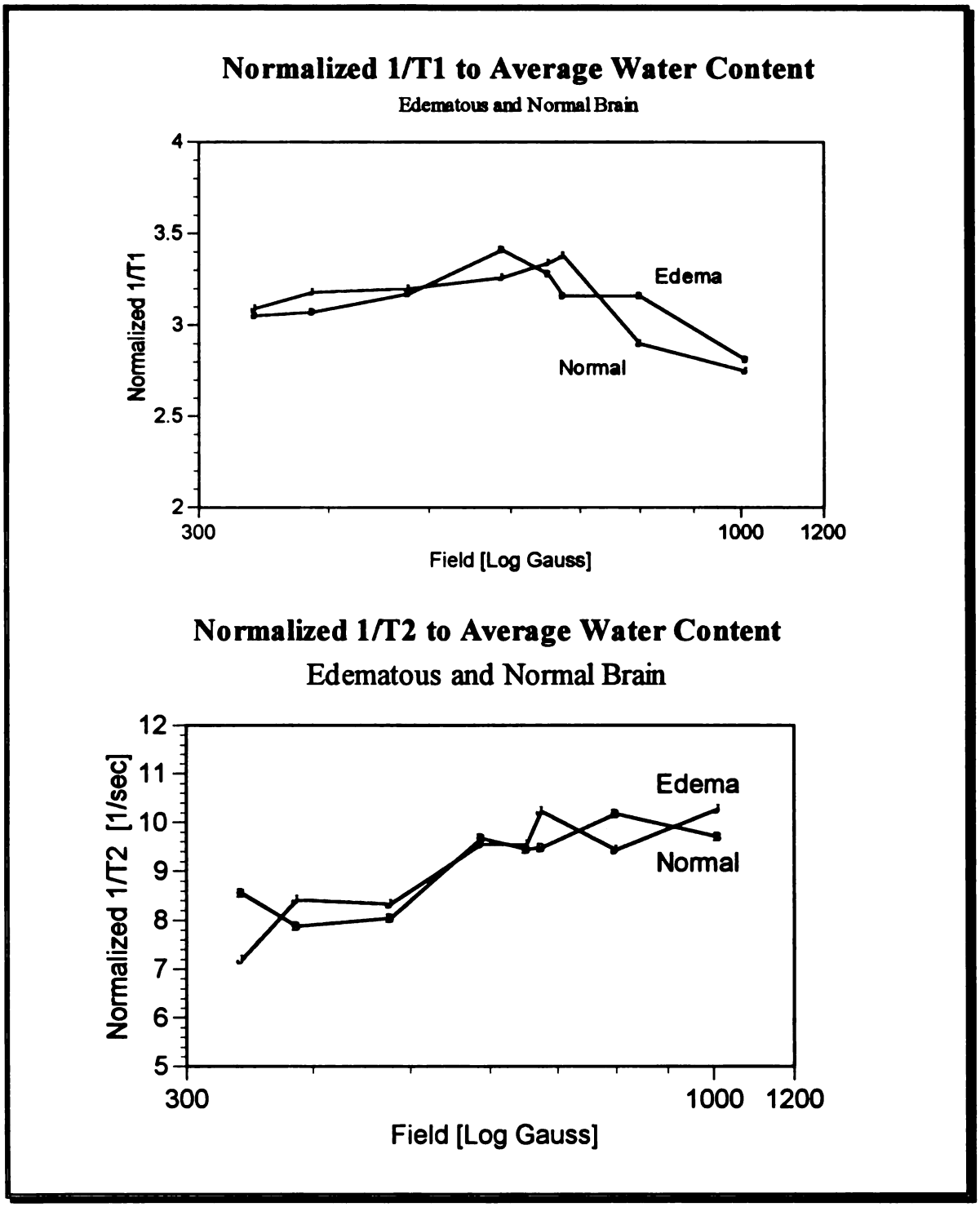

Figure 7.28

Graph of water content normalized T_1 and T_2 relaxation rate changes for normal and edematous brain. The assumption is that all changes of relaxation rate are caused by the changes in water content. The normalization constant is discussed in the text.

Figure 7.28 shows the normalized T_1 and T_2 rates for edematous and normal brain using the same equation used in normalizing the tumor data, equation 7.23. These graphs are not too surprising since the normalization plot given in figure 7.13 also shows the correlation. The single quadrupolar peak are present in the T_1 rates for both edematous and normal brain. The T_2 graph shows the normalized T_2 rate to average water content for edematous and normal brain. Again the results are similar to that given in figure 7.19.

Contrast

Figures 7.29 and 7.30 are contrast plots between lesion and normal tissue as described in the contrast section. The contrast is normalized relative to normal tissue to eliminate the different gain setting used in data acquisition.

Figure 7.29 shows the contrast between tumor and muscle. The contrast is defined as the difference in signal intensity. The three sequence timings used in the MR parameters calculations are plotted. These are the first and second echoes (TE=30,100), for the long TR (900ms) and the first echo for the short TR (150ms). The contrast is highest for the first echo of the long TR sequence. The lowest contrast occurs for short TRs.

Figure 7.30 show the contrast between edematous and normal brain. Notice the contrast for both the first and second echoes of the long TR sequence are about the same. Contrast dispersion is not apparent from the graph with a slight dip occurring at the nitrogen cross relaxation peak.

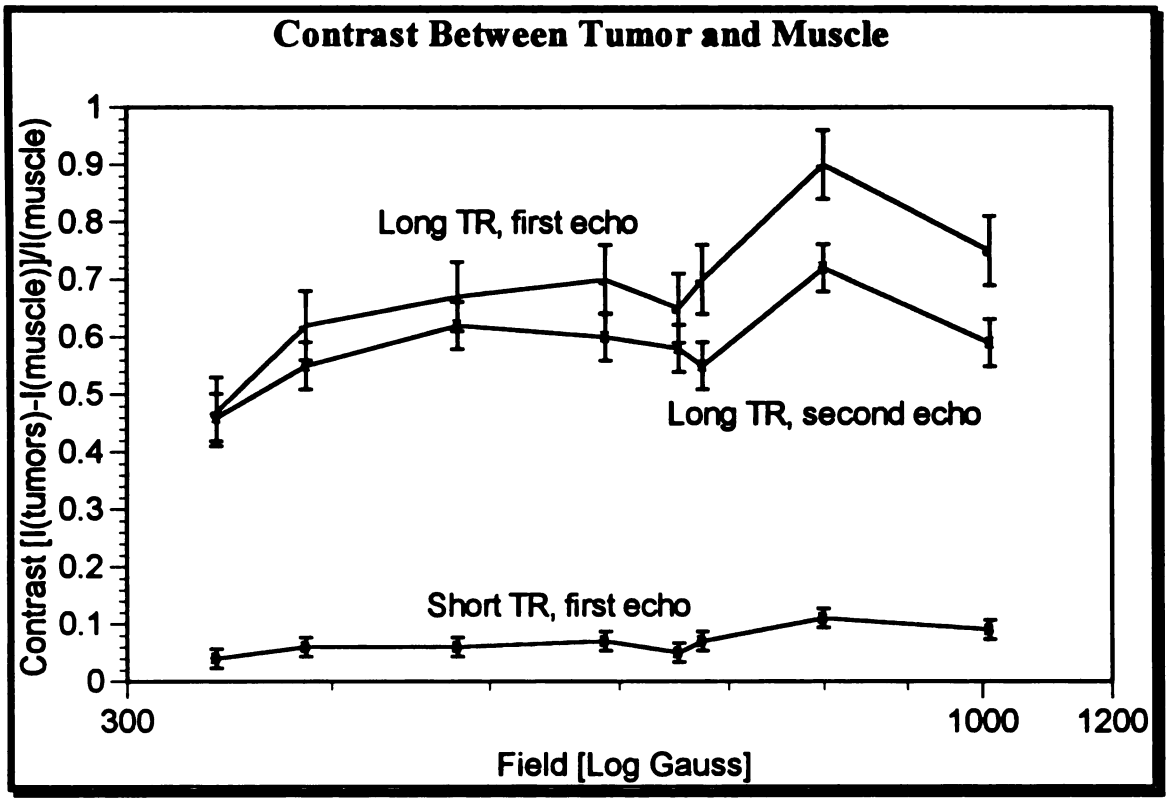

Figure 7.29
Graph of contrast between tumor and muscle.

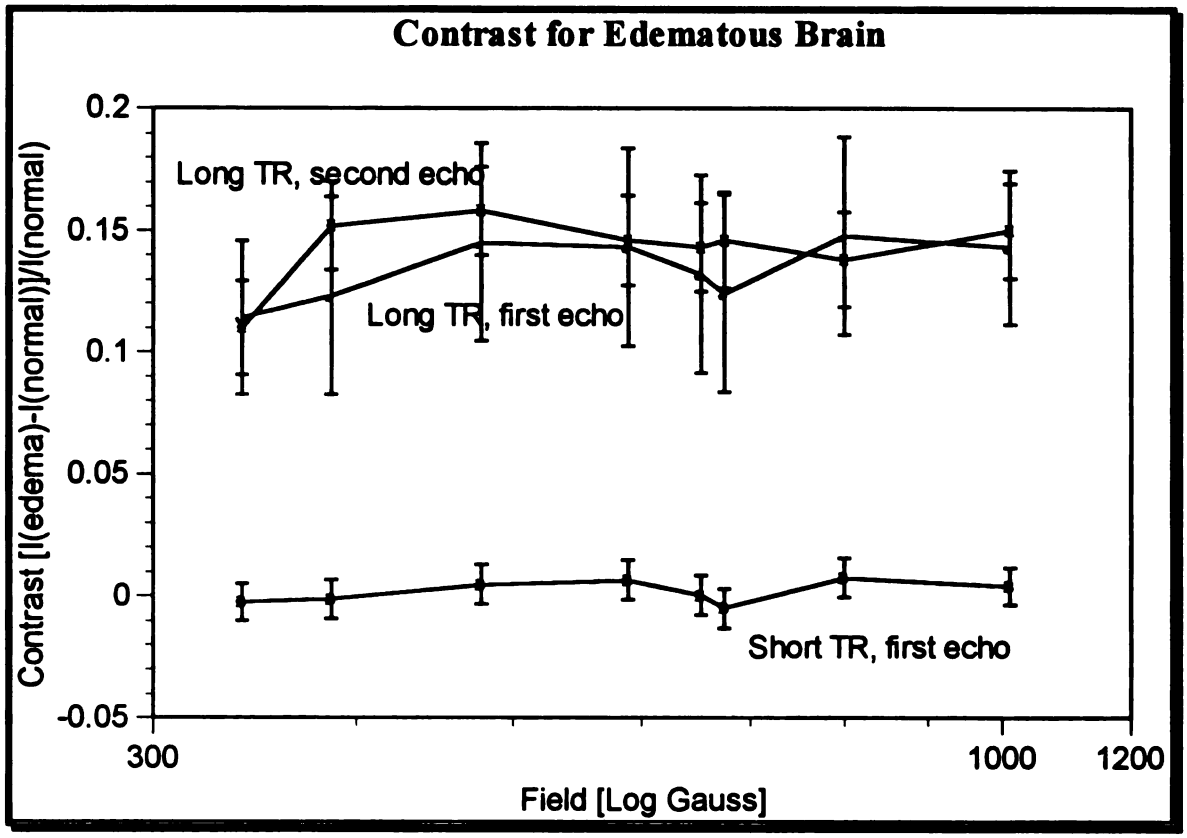

Figure 7.30
Graph of contrast between edematous and normal brain.

Discussion

Models for tissue relaxation are getting better at predicting relaxation times but still lack the unifying ideas or quantities that theories can be built on. The obvious reason is the complexity of tissue. Models for protein relaxation have some success but even in the case of a single protein solution do not reveal most of its secrets. Water content plays a major role in relaxation but water content alone does not account for the relaxation differences, as shown with data from the homogenized brain. Protein correlation time is another quantity that plays a major role in relaxation. NMRDs of protein solutions have shown to display an inflection that correlates with the size of the protein. Tissue's lack of this correlation is shown quite vividly by the change in the NMRD with the denaturing of the same protein. The "cross-linking" of native protein is shown to have "tissue" relaxation characteristics. Tissue "structure" plays a role in relaxation, but how and how much a role it plays are questions to be answered. Protein aggregation has as much to do with relaxation as water content as shown with the HeLa cells by measuring the relaxation times during the HeLa cell cycle[*48*]. The Longitudinal relaxation time was at maximum during mitosis, decreased rapidly upon exiting mitosis, and reaches a minimum during late G1 and early S phase. The water content differs very little during the cell cycle but the quantity and diversity of "free" proteins are very different in mitosis than in S phase. Comparing the water content between lesion and normal tissue shows a definite increase in water content for lesion tissue. This increase of less than 10% in water content does not account for the dramatic increase in relaxation time for the lesion tissue as compared to normal tissue which is greater by more than 100%.

Cross relaxation

Cross relaxation plays a major role in the relaxation rates. The appearance of quadrupolar peaks in muscle NMRD profiles shows that cross relaxation is present. Cross relaxation between protein protons and water protons have also been shown to occur. Applying the cross relaxation model many provide some insight into the relaxation mechanism. Equation 3.38 and equation 3.40 are repeated here for convenience in the case where the exchange is very fast, that is, $k_i >> R_i$,

$$m_i(t) = c_i^+ e^{-R_i^+ t} + c_i^- e^{-R_i^- t} \qquad \text{Eqn 3.38}$$

where

$$
\begin{aligned}
R_1^+ &= k_w + k_p \\
R_1^- &= p_w R_{1w} + p_p R_{1p} \\
c_w^+ &= \left[m_w(0) - m_p(0)\right] p_p \\
c_w^- &= 1 - \left[m_w(0) - m_p(0)\right] p_p
\end{aligned}
\qquad \text{Eqn 3.40}
$$

MRI sequences have very long RF tipping pulses so any protons with very short T2s will dephase well before the finish of the tipping pulse. The protein protons are in this category giving $m_p(0) \sim 0$ and $m_w(0) \sim 1$. This simplifies the constants c_w^+ and c_w^- to

$$
c_w^+ = p_p \quad \text{and} \quad c_w^- \sim 0 \qquad \text{Eqn 7.24}
$$

and what is left is the classic solution,

$$
m(t) \sim p_p m_w(0) e^{-(k_w + k_p)} \qquad \text{Eqn 7.25}
$$

which, as discussed previously, shows the dependencies of the longitudinal relaxation rate on the water content. The inverse linear correlation between relaxation rate and water content fails at low water content. This failure is apparent when the protein term becomes comparable to the free water term. The relationship between the exchange rate is given by,

$$
p_w k_w = p_p k_p \qquad \text{Eqn 7.26}
$$

which gives the relaxation rate as,

$$
\begin{aligned}
R_1^+ &= k_p \left(1 + \frac{p_p}{p_w}\right) \\
&= k_p \left(1 + \frac{1 - p_w}{p_w}\right) = \frac{k_p}{p_w}
\end{aligned}
\qquad \text{Eqn 7.27}
$$

which predicts R_1^+ will be large when water content is low. The other implication that equation 7.27 gives is that for low water contents, R_1^+ may be the dominant relaxation time seen in MR images depending on the value of k_p. It may very well be that k_p is the discriminating factor between relaxation times among different types of tissues. The occurrence of cross relaxation means that relaxation measurement must provide the pulse parameters used for the measurement.

The default assumption, at least in MRI, would be that the pulse will typically be long relative to the short relaxation component. If we assume equation 7.27 is correct, we can get a rough estimate for the ratio p_p/p_w from the brain data. At 340 G, the ratio is

$$\frac{R_{1,edema}}{R_{1,normal}} = \frac{P_{w,normal}}{P_{w,edema}} = \frac{3.07}{3.94} = 0.78 \qquad \text{Eqn 7.28}$$

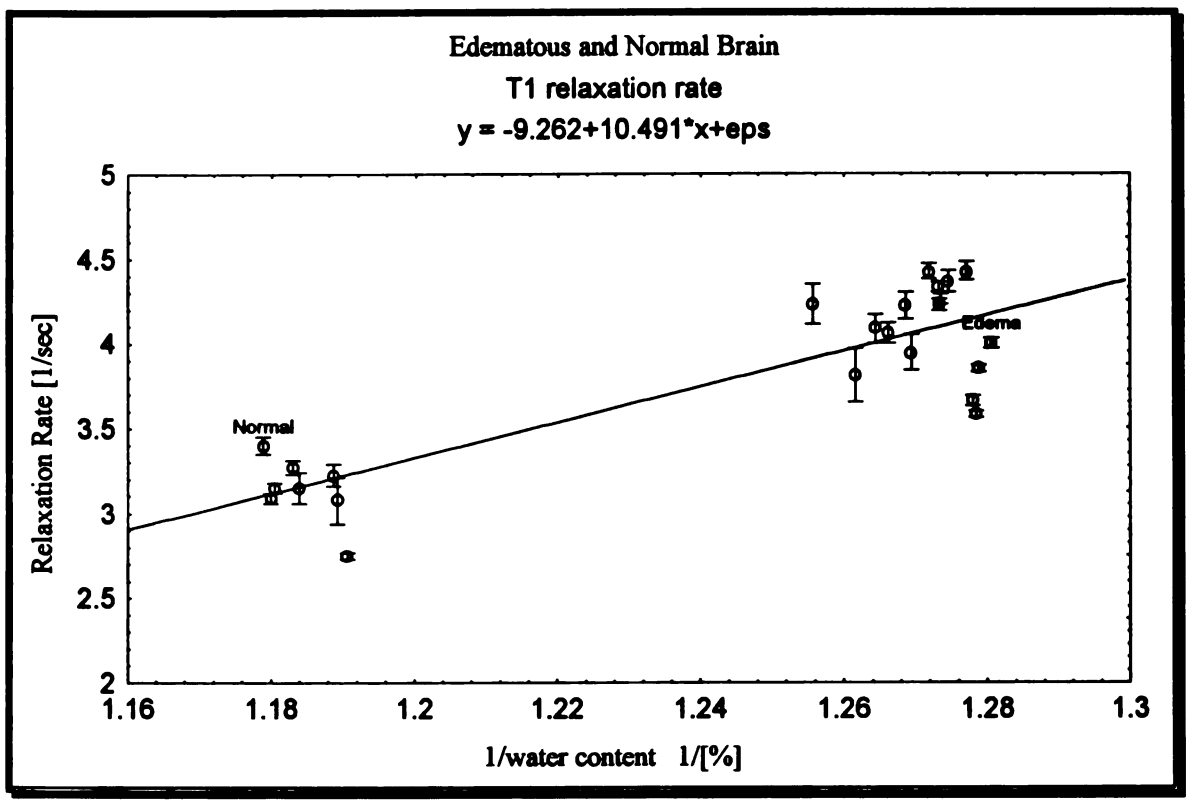

Figure 7.31
Transverse relaxation rate vs. inverse of water content.

Figure 7.31 is the same plot of T1 relaxation rate for edematous and normal tissue given earlier except that 1/(water content) is used for the x-axis. This graph can produce some information from Fullerton's ideas. With the aid of equation 3.23, the sum of the intercept and the slope gives free water relaxation rate,

$$\begin{aligned} R_w &= C_1 + C_2 \\ &= 10.49 - 9.26 \\ &= 1.23 \quad [1/\text{sec}] \end{aligned} \qquad \text{Eqn 7.29}$$

and from this, the protein relaxation rate can be calculated from,

$$R_p = \frac{C_1}{k} + R_w \qquad \text{Eqn 7.30}$$

taking k~.1, we get,

$$R_p = \frac{10.49}{.1} + 1.23 = 105.7 \quad [1/\text{sec}] \qquad \text{Eqn 7.31}$$

which translates to 9.5 ms. Though the numbers may be of the correct magnitude, the problem is the value of k used in Fullerton's model. It was here that Koenig's data show the contradiction as described earlier where the concept of a hydration layer with a percentage "k" was untenable.

Quadrupolar Cross Relaxation

That the quadrupolar peaks are present in muscle and brain tissue shows that cross relaxation is occurring. Of the four types of tissue imaged, only the tumor did not show peaks. Not showing any quadrupolar peaks implies that the one or more of the requirements quoted in the quadrupolar sections were not meet. Not meeting the condition of the spin lattice relaxation of the quadrupolar nuclei being fast as compared to the proton's relaxation time means that the quadrupolar coupling constant $\left(e^2Qq/\hbar\right)$ is very small. In other words, the electric field gradient inducing the quadrupolar relaxation is small. This occurs in very symmetric molecular environment such as in NH_4^+ or other tetrahedral symmetries. What environmental factor produces molecular symmetry in tumors is not clear. The mosaic nature of tumors may be the cause.

The other requirement for the absence of peaks is $\omega_i \tau_c < 1$. This implies the motion is less restrictive in muscle and brain than in tumors or possibly the molecular motions relevant in proton relaxation are considerably smaller. Tumors are undifferentiated and show chaotic patterns in contrast to normal tissue which are well differentiated and well structured so the restrictive motion is not the cause. The increased number of smaller molecules is the reason for the decreased correlation time. Tumors are constantly cycling through the complete cell cycle while most differentiated tissues will get arrested in a certain part of the cell cycle. Normal tissues have the

synthesis of proteins well regulated and the proteins synthesized are of a particular type. Tumors do not have this regulation. At any given time, the tumor will have a percentage of cells in a particular cycle equal to the percentage of time spent in that cycle. Having substantially more cells in the synthesis stage, the tumor will have a substantially larger amount of smaller proteins than a differentiated cell.

The cross relaxation quadrupolar peaks for normal and edematous brain are at a slightly different field strengths but are otherwise very similar. The shift in frequency implies that the quadrupolar coupling constant $\left(e^2Qq/\hbar\right)$ may be slightly different between the normal and lesion tissue. The details are difficult to extrapolate. The coupling constant is dependent on the molecular symmetry, so how increasing the water content of brain tissue changes the symmetry is not clear. It would be more likely that normally excluded proteins that crossed the blood brain barrier are contributing to the cross relaxation.

Dispersion

Dispersion behavior seems to be consistent among cell types irrespective of the water content. This is shown with both, the longitudinal and transverse, relaxation dispersion profiles for normal and edematous brain. Only a scaling factor is the difference between the normal and edematous brain. The scaling factors were 1.29±.04 for the longitudinal component and 1.41±.03 for the transverse component. These changes were caused by ~8% in increased water content. The dispersion behavior is not affected by the introduction of a variety of proteins not normally present in the brain. The corollary to this is that vasogenic edema does not affect the mechanism of dispersion which is intrinsic to the brain. The increase in absolute relaxation time (scaling) can be explained readily by cross relaxation as discussed above. The hydration layer is given the property of dispersion in many models. Introducing extravasted proteins will introduce additional hydration layers to contribute to the dispersion but the data does not show any changes. This additional contribution will have different correlation times because the different sizes of neo-proteins. If Koenig is correct, then the "effective" correlation time should change thus changing the dispersion profile as predicted by his Cole-Cole fit. The brain data do not show this change so either the dominant dispersive hydration layer is somewhere else, intrinsic to brain tissue, or the hydration layer plays only a role if the protein is bound to a relaxation center.

The transverse dispersion profile has a gradual increasing rate as the static field increases. The cause may be from micro susceptibility effects near the protons. The residence time for the proton in the neighborhood of the gradient is fairly long because of the "linear" behavior. Dephasing due to diffusion in the presence of a gradient has a quadratic form,

$$\frac{1}{T_2} = \frac{1}{T_{2,0}} + k\left(\frac{B_0 \Delta\chi}{\Delta x}\right)^2 \qquad \text{Eqn 7.32}$$

where

$T_{2,0}$ = Transverse relaxation in the absence of diffusion

$\Delta\chi$ = Change in suceptibility

Δx = Length of transistion region

k = diffusion constant

The transverse relaxation data for tumor, muscle, and brain do not show such a quadratic field dependency. This may be because of the limited field range span by this experiment but the field dependencies have a more steady increase and are slower than a quadratic function would imply.

References

[1] Koenig, S. H., Brown, R. D., Spiller, M., and Lundbom, N., "Relaxometry of Brain: Why White Matter Appears Bright in MRI", Magnetic Resonance in Medicine 14, 482-495 (1990)

[2] Bloch, F., Nuclear Induction, Physical Review, Vol 70, No 7 and 8, pp 460-485(1946)

[3] Kumar, A. M. Welti, D., and Ernst, R. R., NMR Fourier Zeugmatography, J. Mag. Reson., Vol 18, pp 69-83 (1973)

[4] Edelstein, W. A., Hutchison, J. M. S., Johnson, G., and Redpath, T, Phys. Med. Biol. Vol 25, pp 751, (1980)

[5] Avram, H. E., Hale, J. D., Li, A. J., and Kaufman, L., Evaluation of Truncated Readout-Echo MR Images Obtained at 0.35 T, Radiology, Vol 186, pp 891-901, (1993).

[6] Mitchell, Mark R., Tarr, Robert W., Conturo, Thomas E., "Understanding Basic MR Pulse Sequences", Mag. Res. Imag., Vol II, pp 1269-1310, W. H. Saunders Co, Philadelphia, (1988)

[7] Hoult, D. I. and Richards, R. E., Signal-to-noise of nuclear magnetic resonance experiment, J. Mag. Reson, Vol 24, pp 71-85, (1976)

[8] Chen, J. H, Ph.D. thesis, UC Berkeley, "In-vivo Measurements of MRI Tissue Parameters at Various Magnetic Field Strengths, (1991)

[9] Wong, S. T. S. and Roos, M.S., Effects of Slice Selection and diffusion on T_2 Measurements, Magn. Res. Med., Vol 5, pp 358-365, 1987

[10] Bloembergen, M., Purcell, E. M., and Pound, R. V., "Relaxation Effects in Nuclear Resonance Absorption," Phys. Rev. 73, 679-712 (1948)

[11] Solomon, I., "Relaxation Processes in a System of Two Spins", Phys Rev, Vol 99, No 2, pp559-565, (1955)

[12] Abragam, A., "Principles of Nuclear Magnetism", Clarendon Press, Oxford, (1961)

[13] Slicthter, C. P., "Principles of Magnetic Resonance", Springer-Verlag, New York, (1990)

[14] Cooper C. R., and McGillem, C. D., "Probabilistic Methods of Signal and System Analysis", Holt, Rinehart and Winston, Inc, New York, (1971)

[15] Frohlich, H., "Theory of Dielectrics", 2ed., Oxford Unversity Press, Oxford, (1958)

[16] Winter, F., and Kimmich, R. ,"Spin Lattice relaxation of dipole nuclei (I=1/2) coupled to quadrupole nuclei (S=1)", Mol. Phys., Vol. 45, No. 1, pp 33-49 (1982).

[17] Carrington, A., and McLachlan, A. D., "Introduction to Magnetic Resonance", Harper & Row, New York, (1967)

[18] Bottomley, Paul A., "Frequency Dependence of Tissue Relaxation Times", Mag. Res Imag., Vol II, Partain Et. al. (editors), Saunders, Philadelphia, (1988).

[19] Koenig, S. H., and Brown, R. D., "Relaxometry of Tissue", Ch 11, NMR Spectroscopy of Cells and Organisms, Vol II, Ray K gupta, ed., CRC Press, Boc Raton, Fl (1987)

[20] Cole, K. S., and Cole, R. H., "Dispersion and Absorption in Dielectrics", J. Chem. Phys.Vol. 9, pp 341-351 (1941)

[21] Koenig, S. H., and Brown, R. D., "The importance of the Motion of Water for Magnetic Resonance Imaging", Invest. Radiol., Vol 20, pp 297, (1985)

[22] Koenig, S. H., and Brown, R. D., "Field-Cycling Relaxometry of Protein Solution and Tissue: Implication for MRI", Prog. NMR Specr. Vol 22, PP487-567 (1991)
[23] Koenig, D. B., Brown, R. D., Ugolini, R., "A Unified View of Relaxation in Protein Solutions and Tissue, including Hydration and Magnetization Transfer.", Soc. Mag. Res., Vol 29, No. 1,pp 77-83 (1993)
[24] Bottomley, P. A., Foster, T. H., Argersinger, R .E., Pfeifer, L. M., A review of normal tissue hydrogen NMR relaxation times and relaxation mechanisms from 1-100 MHz: Dependence on tissue type, NMR Frequency, temperature, species, excision, and age, Med. Phys., Vol. 11, No. 4, pp 425-448 (1984)
[25] Bottomley, P. A., Magnetic Resonance Imaging, Vol II, 2nd Ed., Chap. 66, W. B. Sauders Co., Philadelphia, (1988)
[26] Fung, B. M., "Correlation of relaxation time with water content in muscle and brain tissue", Biochim Biophys. Acta, Vol 497, pp 317-322, (1977)
[27] Escanye, J. M., Canet, D., Robert, J., "Nuclear Magnetic Relaxation Studies of Water in Frozen Biological Tissues. Cross-Relaxation Effects between Protein and Bound Water Protons", J. Mag. Res., Vol 58, pp 118-131 (1985)
[28] Fullerton, Gary D., Plotter, Janet L., Dornbluth, N. Carol, NMR Relaxation of Protons in Tissues and Other Macromolecular Water Solutions, Magnetic Resonance Imaging, Vol 1, pp. 209-229, (1982)
[29] Hallenga, K, and Keonig, S. H., "Protein Rotational Relaxation as Studied by Solvent ^{1}H and ^{2}H Magnetic Relaxation", Biochemistry, Vol. 15, No. 19, pp 4255-4263 (1976)
[30] Keonig, S. H., Hallenga, K., Shporer, M. "Protein-Water Interaction Studied by solvent ^{1}H, ^{2}H, and ^{17}O Magnetic Relaxation", Proc. Natl. Acad. Sci. USA Vol 72, pp 2667, (1975)
[31] Edzes, H. T., Samulski, E. T., "The Measurement of Cross-Relaxation Effects in the Proton NMR Spin-Lattice Relaxation of Water in Biological Systems: Hydrated Collagen and Muscle, J. Mag. Res., Vol 31, pp 207-229, (1978)
[32] Edzes, H. T., Samulski, E. T., Cross relaxation and Spin Diffusion in the Proton NMR of Hydrated Collagen, Nature, Vol. 265, pp 531-523, (1977)
[33] Peto, Stéphane, Gillis, Pierre, Fiber-to-Field Angle Dependence of Proton Nuclear Magnetic Relaxation in Collogen, Mag. Res. Imag., Vol 8, No. 6, pp 705-712, (1990)
[34] Edzes, H. T., Samulski, E. T., The Measurement of Cross-Relaxation Effects in the Proton NMR Spin-Lattice Relaxation of Water in Biological System: Hydrated Collagen and Muscle, J. of Mag. Res., Vol. 31, pp 207-229, (1978)
[35] Winter, F and Kimmich, R, NMR Field-Cycling Relaxation Spectroscopy of Bovine Serum Albumin, Muscle Tissue, Micrococcus Luteus, and Yeast, BBA, Vol 719, pp 292-298, (1982)
[36] Keonig, S. H., Bryant, R. G., Hallenga, Klaas, and Jacob, G. S., Magnetic Cross-Relaxation among Protons in Protein Solutions, Biochemistry, Vol 17, No. 20, pp 3448-4358 (1978)
[37] Junqueira, L. C., Carneiro, J., Kelly, R. O., Basic Histology, Appleton & Lange, California, (1989)
[38] Ruddon, R. W., Cancer Biology, Oxford Press, New York, (1987)
[39] Alberts, B., et. al., Molecular Biology of the Cell, 2nd Ed., Garland Publishing, Inc, New York, (1989)
[40] Chan, P. H., and Fishman, Robert A., Brain Edema, Handbook of Neurochemistry, Vol 10, Edited by Abel Lajtha, Plenum Publishing, (1985)
[41] Chan, P. H., Longar, S, Fishman, R. A., Phospholipid Degradation and Edema Development in Cold-Injred Rat Brain, Brain Research, Vol 277, pp 329-337, (1983)
[42] Koenig, H., Goldstone, A. D., and Lu, C. Y., "Blood-Brain Barrier Breakdown in Cold-Injured Brain Is Linked to a Biphasic Stimulation of Ornithine Decarboxylase Activity and Polyamine Synthesis: Both Are Coordinately Inhibited by Verapamil, Dexamethasone, and Asprin.", J. of Neurochemistry, Vol. 52, No. 1, pp 101-109, (1989)
[43] Olson, J.J., Beck, D. W., Warner, D. S., Coester, H., "The Role of New Vessels and Macrophages in the Development and Resolution of Edema Following a Cortical Freeze Lesion in the Mouse", J. Neuropathology and Experimental Neurology, Vol. 46, No. 6, pp 682-694, (1987)

[44] Kamman, R. L., Go, K. G., Brouwer, W., Berendsen,H. J. C., Nuclear Magnetic Resonance Relaxation in Experimental Brain Edema: Effects of Water Concentration, Protein Concentration, and Temperature, Mag. Res. in Med., Vol 6, pp 265-274, (1988)
[45] Gennis, R. B, Biomembranes, Springer-Verlag, New York, New York (1989)
[46] Chan, S. I, Seiter, C. H., and Feigenson, G. W., "Anisotropic and Restricted Molecular Motion in Lecithin Bilayers", Biochem. Biophys. Res. Comm, Vol 46, No. 4, pp 1488-1492 (1972)
[47] Finer, E. G., Flook, A. G., and Hauser, H., "The Nature and Origin of the NMR Spectrum of Unsonicated and Sonicated Aqueous Egg Yolk Lecithin Dispersions", Biochim. Biophy. Acta, Vol 260, pp 59-69, (1972)
[48] Beall, P. T., and Hazlewood, C. F, Nuclear Magnetic Resonance Patterns of Intracellular Water as a Function of HeLa Cell Cycle, Science, Vol 192, pp 904-907, (1976)